

Quantitative Photoluminescence

Studies in

a-Si:H/c-Si Solar Cells

Von der Fakultät für
Mathematik und Naturwissenschaften der
Carl von Ossietzky Universität Oldenburg
zur Erlangung des Grades und Titels einer
Doktorin der Naturwissenschaften (Dr. rer. nat)
angenommene Dissertation

von

Saioa Tardon

geboren am 02.06.1975
in Bilbao (Spanien)

Oldenburg, 2005

Gutachterin/Gutachter: Prof. Dr. G. H. Bauer

Zweitgutachter:

Dr. habil. Rudolf Brüggemann

Prof. Dr. Jürgen Parisi

Tag der Disputation: 11.05.06

Contents

1	Introduction	5
2	a-Si:H/c-Si solar cells	8
3	Photon emission from matter	12
3.1	Injection of photons	12
3.2	Interaction between photons and electrons	13
3.3	Propagation of photons	15
3.4	Extraction of photons	18
3.5	Continuity equation at steady state conditions	19
4	Non-radiative recombination	21
5	Experimental setup	23
6	Quantitative measurements of photoluminescence of absorbers with passivation layers	25
6.1	Determination of quasi-Fermi level splitting	25
6.1.1	Results	26
6.2	Calculation of effective lifetime	29
6.2.1	Definition: bulk lifetime and effective lifetime	29
6.2.2	Effective lifetime from photoluminescence	30
6.2.3	Results	32
6.3	Dependence on intensity	34
6.3.1	Dependence of bulk lifetime on intensity	35
6.3.2	Intensity dependance of the surface recombination velocity	38
6.4	Discussion of results	44
6.5	Comparison of lifetimes from photoluminescence and photoconductive measurements	47
7	Temperature dependence of photoluminescence	49
7.1	Indirect transitions in crystalline silicon	49
7.2	Detailed analysis of PL-spectra at T=17K	50
7.3	Calculation of the absorption coefficient at different temperatures	52
7.4	Effective lifetime at different temperatures	55

8	a-Si:H/c-Si solar cell processing: step by step via PL	64
8.1	Sample description	64
8.2	Experimental results and simulation	65
8.3	Interpretation and discussion	76
9	Photoluminescence at different operating modes of an illuminated heterodiode	83
9.1	Photoluminescence of solar cells at open circuit and short circuit . .	83
9.1.1	Simulation of $Y_{pl,V_{oc}}/Y_{pl,I_{sc}}$ and estimation of interface defect densities	87
9.2	I-V-characteristics from photoluminescence	89
9.3	Error estimation between voltages derived from PL and electrically measured voltages	99
9.4	Conclusions	102
10	Summary / Zusammenfassung	104
A	Error calculation in the splitting of quasi-Fermi levels	109
B	Defects in a-Si:H	112
C	Recombination through interface defects	114
D	Calibration of photoluminescence setup	117

Chapter 1

Introduction

Homojunction crystalline silicon solar cells are nowadays broadly extended in the market, but still the price is not competitive with other energy resources. In order to reduce costs new structures and technologies are investigated, being the hydrogenated amorphous silicon / crystalline silicon (a-Si:H / c-Si) solar cells one of these alternatives. The first studies about a-Si:H/c-Si heterojunctions were developed in the early 1980s [1]. The main reason to substitute the crystalline silicon homo-junction is diminution of costs and easier production. While the deposition temperature of the a-Si:H layer is only around 250 ° C, the diffusion of dopants in c-Si to form the pn-junction achieves values up to 800 ° C [2]. Moreover, there are other advantages associated to heterojunction structures, as it can be window enhanced due to the greater band gap of a-Si:H. With this structure, efficiencies up to 21 % have been achieved [3, 4]. Unfortunately, the interface between the a-Si:H layer and the c-Si substrate contains a large density of defects, which are likely to act as recombination centers and reduce the splitting of quasi-Fermi levels in the bulk. In this work the investigations are centered on luminescence from a-Si:H/c-Si solar cells in order to understand the behavior and problems of these kind of solar cells.

Photoluminescence (PL) measurements are a powerful tool for the characterization of wafers and solar cells. The purpose of this thesis is to show the different possibilities of PL experiments in this field. Comparison between different passivation layers on the same substrates, determination of the evolution of the potential open circuit voltage from wafers or calculation of effective lifetimes are some of the applications of the PL technique.

The emitted photon flux can be described by Generalized Planck's Law, which accounts for non-thermal radiation by assigning a chemical potential to the emitted photons [5]. In semiconductors with local homogeneous distribution of the carrier densities, this chemical potential is equivalent to the splitting of quasi-Fermi levels, the latter representing the maximal voltage that can be obtained at open circuit conditions. Radiative recombination rate in the device is reduced if non-radiative

processes are increased by, for example, introduction of defects into the bulk or at the surface. This variation of recombination rates is reflected in the splitting of quasi-Fermi levels in the bulk and thereby in the emitted PL intensity [6, 7]. Known the splitting of quasi-Fermi levels defect densities can be estimated or the detection of recombination channels by PL. Furthermore, by the quantitative description of the photoluminescence, the absorption coefficient and absorbance can be calculated [8, 9].

One great advantage of PL measurements is that they can be performed in a contact less way. This allows the determination of the splitting of quasi-Fermi levels on substrates or samples that are not yet processed into a complete solar cell [10, 11]. Moreover, variation of photoluminescence can be measured after each step of the processing of solar cells, so that defects introduced by a specific process can be detected before the solar cell is finished, which can be used to improve the processing steps.

After a description of the a-Si:H/c-Si solar cells in chapter 2, the theory related to the physical description of photoluminescence or radiative recombination and its derived analytical expression is developed in the third chapter of this thesis. In the next chapter a short description of the non-radiative processes is presented. Chapter 5 includes all the details concerning the calibration of the setup in order to obtain quantitative PL measurements.

The results obtained during the investigations of this thesis are explained on chapters 6, 7, 8 and 9. The determination of the splitting of quasi-Fermi levels from quantitative measured curves is extensively described in chapter 6, together with the calculation of the effective lifetimes from wafers with different passivation layers. Furthermore, the problem of the separation of bulk and surface recombination is analyzed via their intensity dependance.

Chapter 7 exposes the variation of the photoluminescence spectra with the temperature. The different phonon transitions are identified and compared with previous experimental results. Moreover, the evolution of the effective lifetime for different temperatures is also studied.

During the processing of a-Si:H/c-Si solar cells, different layers are deposited in order to get passivation, pn-junction, back surface field, contacts, etc [12]. The electronic structure and band bending, specially in the space charge region, can be affected by any of these steps and improve the whole structure or, on the contrary, increase the recombination and possible losses. In chapter 8, the processing of an a-Si:H/c-Si solar cell is analyzed via photoluminescence. Through the comparison of the splitting of quasi-Fermi levels and simulation of different interface defect distribution, different parameters of these defects have been estimated.

Finally, in the last chapter, photoluminescence has been measured and simulated at different operating points. Measuring photoluminescence it is possible to distinguish losses in the bulk from external losses in the contacts. With the help of simulation studies, the calculation of the voltage for operation points with a different current density extraction has been analyzed.

Chapter 2

a-Si:H/c-Si solar cells

In the following chapter, I will describe the main properties of the a-Si:H/c-Si solar cells in order to show the structure that has been analyzed and introduce the problems which need to be solved.

In semiconductor heterojunctions, the materials at both sides of the junction are different semiconductors. In the investigated heterostructure the absorber is monocrystalline silicon (c-Si). This material has a periodic and homogeneous crystal lattice structure with each of its atoms tetrahedrally bonded to other four neighboring ones. Due to this, it has almost no defects or impurities, being ideal to produce high efficiency solar cells. The band gap of silicon, around 1.12 eV at 300 K, is close to the optimum for absorbing the photon spectrum of the sun. As already mentioned the reduction of cost due to reduction of emitter deposition temperature and easier production [13] are some of the main reasons for the substitution of the homo-junction by the hetero-junction. Other reasons, as a good lattice match and a larger band gap around 1.7 eV (what is translated in absorption by shorter wavelengths than the absorption with a diffused emitter), do make a-Si:H ideal to form a heterostructure with c-Si. Unfortunately, due to its amorphous structure, a-Si:H has a large density of defects in the form of dangling bonds, which occur when a silicon atom does not bond to four neighboring atoms, and localized states known as band tails, which are energetically described by an exponential decay from the valence and conduction band into the band gap. Dangling bonds are situated in gaussian distribution around mid-gap and together with the band tails form a continuous defect distribution through the band gap, so that it is not possible to define a sharp energetic region in amorphous silicon without any states [14, 15]. A schematic representation of this material is depicted in Figure 2.1 (a). Figure 2.1 (b) shows a sketch of a typical energetic distribution of states versus energy in a-Si:H. The two peaks in the dangling bonds are due to the superposition of two Gauss distributions: one for neutral and positively charged defects and the other for negatively charged defects which differ in energy by a correlation energy. More details about defects in a-Si:H are described in Appendix B. Hydrogenated intrinsic amorphous silicon has a characteristic decay constant in the conduction

band tail around 30 meV and in the valence band tail ca. 50 meV [14]. Larger values of around 200 meV [16] have been found e.g. for n-doped a-Si:H layers. Hydrogenated amorphous silicon is a material with a high density of midgap defects, around 10^{16}cm^{-3} for intrinsic a-Si:H and 10^{19}cm^{-3} for doped a-Si:H [17, 14]. The concentration and localization of the described states determines the transport properties and recombination kinetics in a-Si:H.

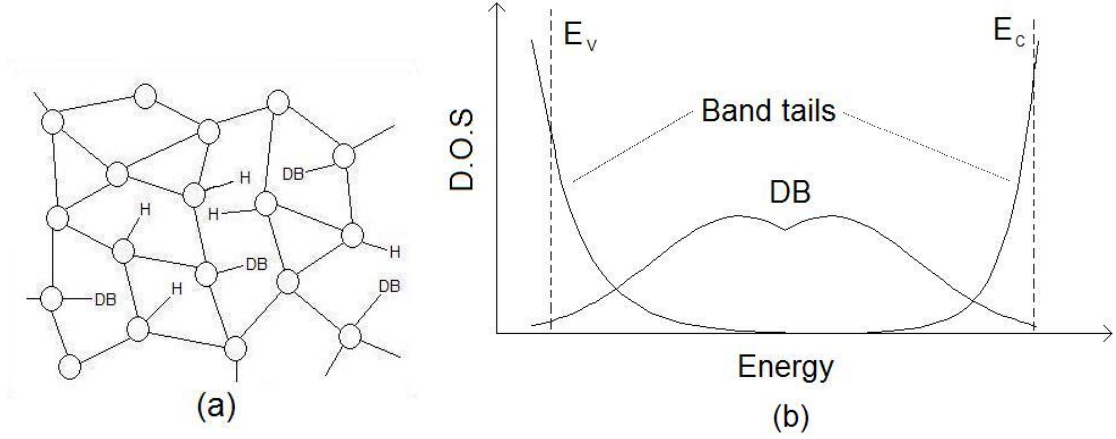


Figure 2.1: (a) Schematic representation of hydrogenated amorphous silicon. Dangling bond defects (DB) arise from unsatisfied silicon bonds in the amorphous network and they can be reduced via introduction of hydrogen (H) (b) Sketch of the density of states (D.O.S.) versus energy in amorphous silicon.

Figure 2.2 (a) shows the band diagram of an (n)a-Si:H/(p)c-Si heterojunction. For the construction of this diagram it is necessary to know the electron affinities (energy needed to remove an electron from the bottom of the conduction band E_C to vacuum level), $\chi_{a-Si:H}$ and χ_{c-Si} , and the band gaps, $E_{a-Si:H}$ and E_{c-Si} , of the two semiconductors. In thermodynamic equilibrium the Fermi level must be constant through the whole device and the vacuum level should be continuous. As a result, it can be seen that discontinuities in the conduction band $\Delta E_C = \chi_{c-Si} - \chi_{a-Si:H}$ and in the valence band $\Delta E_V = E_{a-Si:H} - E_{c-Si} + \chi_{c-Si} - \chi_{a-Si:H}$ are formed just at the junction between both materials [19]. The appearance of discontinuities in the band diagram when both materials are joined together can affect transport and recombination of charge carriers and therefore the electronic behavior of the device [20].

The principal problem when dealing with a-Si:H/c-Si heterostructures is the recombination of carriers at the interface [21, 22]. Although a large number of carriers are generated in the volume in crystalline silicon, if there is a high recombination at the interface, for diffusion lengths values around and larger than the thickness of the wafer, the splitting of quasi-Fermi levels in the bulk will be strongly decreased. In order to reduce this recombination rate, defect passivation techniques

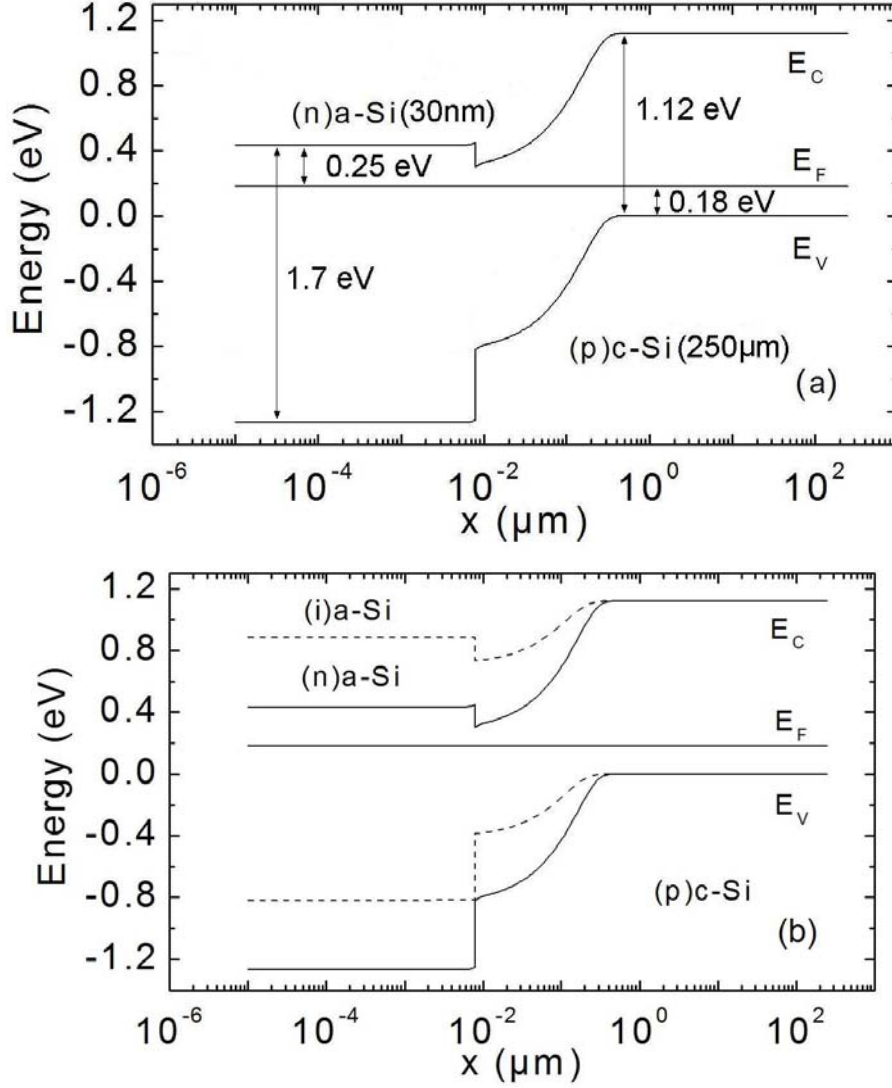


Figure 2.2: (a) Band diagram of a (n)a-Si:H/(p)c-Si heterostructure in thermodynamic equilibrium from numerical simulation. It should be noted that the abscissa axis is depicted in logarithmic scale in order to distinguish what occurs in the bulk and on the a-Si:H side. The Fermi level is constant along the whole device. The difference in electron affinities and band gap of both materials produces band bending and the appearance of discontinuities in the conduction E_C and valence band E_V (b) Band diagram of an a-Si:H/c-Si heterostructure for different doping densities of the amorphous silicon (dashed curve: intrinsic, continuous curve: n-doped). It can be easily seen how the band bending is changed due to the different Fermi levels in a-Si:H. [18]

are required [23]. A direct method to reduce the defect density at the surface of crystalline silicon is to remove them via chemical processes as it can be HF etching of the wafer. Indirectly, recombination can be avoided at the interface in two ways:

1. introducing positive (negative) charged carriers that repel the electrons (holes) moving towards the interface, 2. via band bending to form gradients which avoid potential wells that accumulate carriers. These two effects can be obtained via deposition of passivation layers on crystalline silicon substrates [24, 25].

In this work two different passivation layers have been investigated: silicon nitride (SiN) and hydrogenated amorphous silicon. It has already been shown [26] that on moderately p-type doped silicon wafers there is a fixed positive charge density within the SiN films which can create a n^+p junction with an associated space charge region. This inversion conditions at the surface assists in minimizing carrier recombination at the surface of the silicon wafer. Amorphous silicon has also been proven to be a very good passivation layer for p- and n-type silicon wafers due to hydrogen diffusion into the interface and consequently effective passivation of dangling bond states [27]. As it was mentioned in the previous paragraph, recombination at the interface can be avoided or reinforced depending on the gradient and appearance of potential wells. For a-Si:H, the positive (negative) charges are obtained from positive (negative) charged defects in dangling bonds. The density of positive (negative) dangling bonds changes considerably with the position of the quasi-Fermi energy and defect distribution. Furthermore, doping of a-Si:H shifts its Fermi level and therefore the gradient of electric potential in the region near to the interface changes. This fact can be observed in Figure (2.2 (b)). Talking about the passivation properties of a-Si, it seems to be a controversy, because its defects can also affect the a-Si:H/c-Si interface and increase recombination. This problem will be discussed in detail later.

In the samples analyzed, the thickness of the a-Si:H is very small (from 5 to 180 nm) in comparison with the thickness of the c-Si wafer ($250 \pm 15 \mu m$) so that generation of minority carriers within the a-Si:H film with illumination can be neglected. For this reason in this work the term surface recombination rather than interface recombination is used. In this sense, the interface recombination can be treated as a surface recombination of excess carriers generated in the c-Si bulk.

Chapter 3

Photon emission from matter

In accordance with the second law of thermodynamics, all materials that absorb radiation emit also radiation. If this did not happen, temperature of the absorber would increase above that of the source violating the mentioned law. This is the principle of photoluminescence: emission of photons is produced after absorption of photons. The state of the emitter is reflected in the spectrum of the emitted photons and therefore information of the material investigated can be obtained. This makes photoluminescence a very powerful tool for the analysis of materials in general, or in this particular case, solar cells.

In the following chapter I describe in detail the interaction of light with matter by quantification of the photons which are generated via photoluminescence till they are finally measured by a detector.

3.1 Injection of photons

When a material is illuminated by a source of photons, for example, a laser, a fraction of the incident photons are propagated following the law of refraction [28] due to the different refraction indexes between the air and the studied matter.

This fraction of photons reflected can be calculated using the Fresnel equations [28], obtained from the continuity conditions for a magnetic and electric field at a boundary between two media, and considering that the incident wave is normal to the surface is given by:

$$R = \left(\frac{n_i - n_t}{n_i + n_t} \right)^2 \quad (3.1)$$

with n_i and n_t being the refraction indices of the two media, from which photons come and to which photons are transmitted, respectively.

Thus, if ϕ_i is the photon flux incident on the silicon wafer, the number of photons which in fact is injected into the wafer, without being reflected is:

$$\phi_0 = (1 - R)\phi_i \quad (3.2)$$

where ϕ_0 is the photon flux at $x=0$ inside the wafer.

The Lambert-Beer-Bouguer law describes the profile of propagating photons in a material:

$$\phi(x) = \phi_0 \exp(-\alpha x) = (1 - R)\phi_i \exp(-\alpha x) \quad (3.3)$$

where $\phi(x)$ is the photon flux at a distance x inside the material, and α the absorption coefficient. Figure 3.1 shows the generation profile in a crystalline silicon wafer with a thickness of $250 \mu\text{m}$ excited with a wavelength of $\lambda = 782 \text{ nm}$, an absorption coefficient of 1010 cm^{-1} and an incident photon flux equivalent to $4 \times \text{AM1.5}$, as in the measurements used in this work.

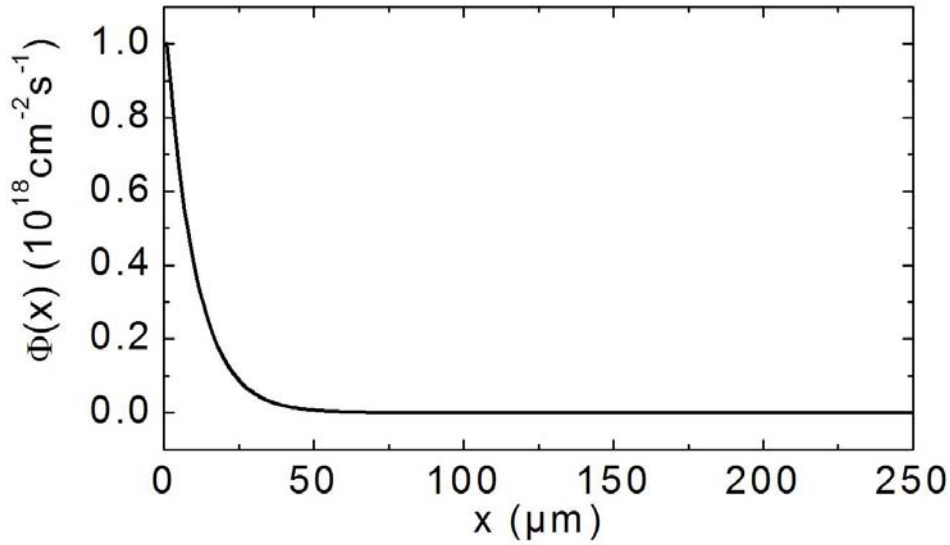


Figure 3.1: Photon flux profile in a silicon wafer with a thickness of $250 \mu\text{m}$ illuminated with a laser of a wavelength of $\lambda = 782 \text{ nm}$. An absorption coefficient of 1010 cm^{-1} and a reflection coefficient of 0.308 were considered between silicon and air.

3.2 Interaction between photons and electrons

Once photons are inside the material, they interact with the atoms or molecules that form the investigated matter. In our case, we are working with solids and

in concrete with semiconductors and therefore, photons interact with the electrons that form the valence band of the lattice and provide them sufficient energy to be free and fall into the conduction band. Electrons with a larger energy than the band gap ($E_n = E_C + 3/2kT$) thermalize by emission of multiple phonons till they reach the bottom of the conduction band. The return to the initial state occurs by again emission of multiple phonon or/and a photon.

As electrons are fermions their distribution function is described by Fermi-Dirac statistics. With illumination, as both electrons and holes are generated, it is necessary to use two Fermi distributions, one for the electrons and one for holes. The corresponding Fermi energies are known as the quasi-Fermi energies for electrons and holes respectively. The temperature of these Fermi distributions is the temperature of the lattice due to the frequent collisions between electrons and holes with the atoms. The densities for electrons and holes described by the Fermi energies under illumination are [29]

$$n = N_C \exp\left(-\frac{E_C - E_{F_n}}{kT}\right) \quad p = N_V \exp\left(-\frac{E_{F_p} - E_V}{kT}\right) \quad (3.4)$$

After the generation of electron-hole pairs via illumination, recombination of the excited carriers takes place. Figure 3.2 shows the different possible recombination

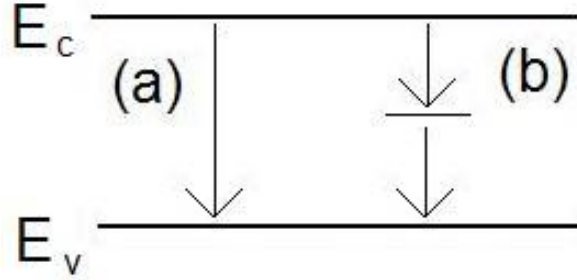


Figure 3.2: Possible recombination processes between the conduction band and the valence band in a semiconductor: (a) band-band recombination and (b) recombination via defects.

processes which can occur: (a) radiative recombination (usually band-band recombination, but it could also occur via defect levels in the gap) emitting photons which are detected as photoluminescence and (b) non-radiative recombination (via impurities or defects). For the case of indirect semiconductors, as silicon, the maximum of the valence band and the minimum of the conduction band are not in the same k -position, so that phonons are necessary in order to satisfy the momentum conservation in the existent reactions. This balance [5] between photons (γ), phonons (Γ), electrons in conduction band E_C (n) and holes in the valence band E_V (p) is described by

$$\gamma \Leftrightarrow n + p \pm \Gamma \quad (3.5)$$

Calculating the minimum of the Free Energy for the system in equilibrium conditions at constant entropy and volume

$$\mu_\gamma = \eta_n + \eta_p \pm \mu_\Gamma \quad (3.6)$$

where μ_γ , η_n , η_p and μ_Γ are the chemical potential of photons, the electrochemical potential of electrons and holes and the chemical potential of phonons, respectively.

For the case of indirect semiconductors [8] $\mu_\Gamma \approx 0$ as the generation and recombination rate of phonons in radiative transitions is much larger than the overall photon-generation and absorption rates. A phonon lifetime is around 10^9 times smaller than a carrier lifetime in silicon ($\sim 500 \mu s$) and in consequence, recombination processes do not influence the number of phonons.

$\eta_n + \eta_p = E_{F_n} - E_{F_p}$ from the sum of the electrochemical potential of the electrons and holes and therefore it can be found:

$$\mu_\gamma = E_{F_n} - E_{F_p} \quad (3.7)$$

if $E_{F_n} - E_{F_p}$ is spatially constant in the semiconductor wafer or solar cell.

3.3 Propagation of photons

Photon generation is given by the rate of spontaneous emission dr_{sp} . The definition of the absorption using the photon flux is: $-div(dN_\gamma(\hbar\omega)) = \alpha(\hbar\omega)dN_\gamma$. The net absorption rate is defined by the difference between the absorption rate and the stimulated emission rate: $dr_{abs}(\hbar\omega) - dr_{stim}(\hbar\omega) = \alpha(\hbar\omega)dN_\gamma$. Using the principle of the Detailed Balance [30]: $dr_{abs}(\hbar\omega) - dr_{stim}(\hbar\omega) = dr_{sp}(\hbar\omega)$ [31]. Therefore:

$$dr_{sp}(\hbar\omega) = \alpha(\hbar\omega) \frac{c_0}{n} D_\gamma(\hbar\omega) \frac{1}{\exp\left(\frac{(\hbar\omega) - \mu_\gamma}{kT}\right) - 1} d(\hbar\omega) d\Omega \quad (3.8)$$

where $D_\gamma(\hbar\omega) = n^3(\hbar\omega)^2 / (4\pi^3 \hbar^3 c_0^3)$. Considering the photon flux in x-direction, and introducing the equation 3.7 assuming that the splitting of quasi-Fermi levels is spatially dependent:

$$\begin{aligned} dr_{sp}(x, \hbar\omega) &= \frac{\alpha(\hbar\omega)(\hbar\omega)^2}{4\pi^3 c^2 \hbar^3} \left[\exp\left(\frac{\hbar\omega - \mu_\gamma(x)}{kT}\right) - 1 \right]^{-1} d(\hbar\omega) d\Omega \\ &= \frac{\alpha(\hbar\omega)(\hbar\omega)^2}{4\pi^3 c^2 \hbar^3} \left\{ \exp\left[\frac{\hbar\omega - (E_{F_n}(x) - E_{F_p}(x))}{kT}\right] - 1 \right\}^{-1} d(\hbar\omega) d\Omega \end{aligned} \quad (3.9)$$

where $c=c_0/n$ is the velocity of light in the semiconductor material and n is its refraction index. Total thermalization of the excited carrier has been taken into

account in order to use the quasi-Fermi energies to describe the states that participate in radiative transitions.

Silicon has a refraction index of $n \simeq 3.5$ at luminescence wavelengths ($\lambda \approx 850 \dots 1300$ nm) and due to this, photons coming from photoluminescence, which reach the surface between Si and air with an angle larger than $\theta = 16.6^\circ$ are totally reflected (around 96 %). Thus, angle dependance of the spontaneous emission rate is not taken into account as all the photons emitted by the semiconductor are nearly perpendicular to the surface and the rest is totally reflected.

Losses in the photon flux are given by reabsorption, which means that the initially generated photons are absorbed and therefore do not contribute to the emitted photon flux. This effect is accounted by a factor $r_{sp} \exp(-\alpha x)$ when the photons flow through the wafer. In this case, the photon flux balance can not be strictly divided in gain and loss, as the losses depend on the rate of the spontaneous emission. Equation 3.9 describes the spontaneous emission rate which contributes to the photon flux in a positive x-direction. The same contribution flows in the negative x-direction. Once the photons reach the surface of the semiconductor, part of them are reflected back continuing in the positive direction. When the photon flux reaches to the front side again, the same effects occur: part of the photons are transmitted and part are reflected back to the material, where they are partially absorbed on the way back. This happens continuously and is known as multi-reflection. Figure 3.3 shows schematically this effect.

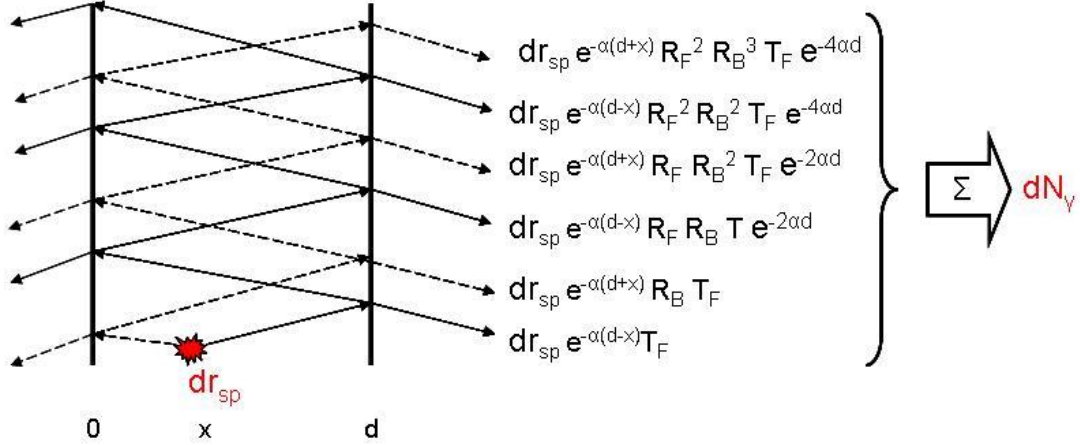


Figure 3.3: Sketch showing multi-reflection of photons at both sides of a wafer. Photoluminescence intensities were calculated each time when reflection and transmission took place.

In the case of a thick silicon slab, as is the case of our wafer, we have to consider that the photoluminescence centers emit waves (photons) with random phases, so that the total flux density can be determined by the sum of the individual flux

densities [28]. Doing this calculation we find:

$$\begin{aligned}
dN_\gamma(x, \hbar\omega, \Omega) &= dr_{sp}(x, \hbar\omega, \Omega)e^{-\alpha(d-x)}T_F(1 + e^{-2\alpha d}R_F R_B + e^{4\alpha d}R_F^2 R_B^2 + \dots) + \\
&\quad dr_{sp}(x, \hbar\omega, \Omega)e^{-\alpha(d+x)}T_F R_B(1 + e^{-2\alpha d}R_F R_B + \dots) \\
&= (dr_{sp}(x, \hbar\omega, \Omega)e^{-\alpha(d-x)}T_F + dr_{sp}(x, \hbar\omega, \Omega)e^{-\alpha(d+x)}T_F R_B) \\
&\quad \times ((1 + e^{-2\alpha d}R_F R_B + e^{-4\alpha d}R_F^2 R_B^2 + \dots))
\end{aligned} \tag{3.10}$$

Applying the conversion for a geometric progression sum: $a + ar + ar^2 + ar^3 = \frac{a}{1-r}$

$$dN_\gamma(x, \hbar\omega, \Omega) = dr_{sp}(x, \hbar\omega, \Omega) \frac{(1 - R_F)e^{-\alpha d}}{1 - e^{-2\alpha d}R_B R_F} (e^{\alpha x} + R_B e^{-\alpha x}) \tag{3.11}$$

being R_F and R_B the reflection coefficients at the front and back sides of the silicon wafer respectively and $T_F = 1 - R_F$ at the surface. These coefficients together with the absorption coefficients are wavelength dependent, but it was not been written in the previous equations in order to simplify the expression.

Another gain in photoluminescence is due to photon recycling, i.e, absorption of photons and subsequent re-emission, which in the case of silicon is negligible. Both processes are proportional to $\alpha(\hbar\omega)$ and as four particles are needed, the transition probability is very low for an indirect semiconductor.

The previous expression should be integrated over the thickness of the wafer to obtain photoluminescence from all emission centers:

$$\begin{aligned}
dN_\gamma(d, \hbar\omega) &= C(\hbar\omega) \times \int_0^d \frac{\exp[\alpha(\hbar\omega)x] + R_B(\hbar\omega) \exp[-\alpha(\hbar\omega)x]}{\exp\left[\frac{\hbar\omega - (E_{F_n}(x) - E_{F_p}(x))}{kT}\right] - 1} dx \\
&= \frac{\alpha(\hbar\omega)(\hbar\omega)^2}{4\pi^3 c^2 \hbar^3} \times \frac{[1 - R_F(\hbar\omega)] \exp[-\alpha(\hbar\omega)d]}{1 - \exp[-2\alpha(\hbar\omega)d] R_B(\hbar\omega) R_F(\hbar\omega)} d(\hbar\omega) d\Omega \\
&\quad \times \int_0^d \frac{\exp[\alpha(\hbar\omega)x] + R_B(\hbar\omega) \exp[-\alpha(\hbar\omega)x]}{\exp\left[\frac{\hbar\omega - (E_{F_n}(x) - E_{F_p}(x))}{kT}\right] - 1} dx
\end{aligned} \tag{3.12}$$

This emission formula is the generalization of Planck's law [32, 5], which extended the thermal radiation described by Planck to radiation of any kind by the introduction of the chemical potential of photons. It was developed considering a cavity filled with matter and calculating the balance between absorption and emission processes.

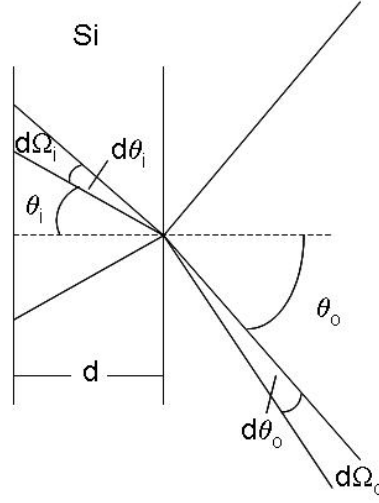


Figure 3.4: Sketch showing the incident and refracted angle and solid angles of photon fluxes inside and outside of the silicon wafer. The angles inside the wafer are oversized in order to show them clearer.

3.4 Extraction of photons

Till now we have considered the radiation inside the semiconductor but we measure from outside the radiation emitted across the surface. We have already calculated the photon flux arriving at the surface of the semiconductor from a solid angle $d\Omega$, which is given by formula (3.12). A sketch of the solid angles inside and outside of the wafer can be seen in Figure 3.4. Due to the different refraction indices inside and outside the silicon slab, the relation between the photon flux leaving ($dN_{\gamma,o}$) and reaching (dN_{γ}) the surface is given by:

$$dN_{\gamma,o}(\hbar\omega) = \frac{1}{n^2} dN_{\gamma}(d, \hbar\omega) \quad (3.13)$$

where n is the refraction index of the material. Using the Snell's law, the solid angle inside the wafer is related to the solid angle viewed by the detector [33] by

$$d\Omega = \frac{1}{n^2} \cos \theta_o d\Omega_o \quad (3.14)$$

being θ_o the angle that the photons inside the solid angle $d\Omega_o$ form with the normal to the surface. Besides, I have considered, as mentioned in the previous sections, that the angle inside the silicon is so small that it can be considered: $\theta_i \approx 0 \rightarrow \cos \theta_i \approx 1$.

Introducing (3.14) in (3.12), the photon flux in the solid angle interval $d\Omega$ and in the photon energy interval $d(\hbar\omega)$ measured by the detector is obtained as:

$$\begin{aligned}
dN_\gamma(d, \hbar\omega) &= \frac{\alpha(\hbar\omega)(\hbar\omega)^2}{4\pi^3 c_o^2 \hbar^3} \times \frac{[1 - R_F(\hbar\omega)] \exp[-\alpha(\hbar\omega)d]}{1 - \exp[-2\alpha(\hbar\omega)d] R_B(\hbar\omega) R_F(\hbar\omega)} d(\hbar\omega) \cos \theta_o d\Omega_o \\
&\times \int_0^d \frac{\exp[\alpha(\hbar\omega)x] + R_B(\hbar\omega) \exp[-\alpha(\hbar\omega)x]}{\exp\left[\frac{\hbar\omega - (E_{F_n}(x) - E_{F_p}(x))}{kT}\right] - 1} dx \\
&= dn_\gamma(\hbar\omega) \cos \theta_o d\Omega_o
\end{aligned} \tag{3.15}$$

being $n_\gamma(\hbar\omega)$ the photon flux per stereo radian in the energy interval $d(\hbar\omega)$.

3.5 Continuity equation at steady state conditions

As it was described in the previous sections photons falling into the semiconductor wafer generate electrons that propagate through the material till they recombine. In the following section I describe the spatial evolution of electrons in 1 dimension when the material is illuminated in steady state conditions. The differential equation that describes the charge carrier concentration is:

$$\frac{\partial}{\partial t} n(x) = -\frac{\partial}{\partial x} \frac{1}{q} j_n(x) + G_n(x) - S_n(x) = 0 \tag{3.16}$$

where n is the electron concentration, j_n is the electron current density, G_n is the electron generation term and S_n is the electron loss term.

Considering that each photon absorbed by the wafer generates an electron-hole pair, G_n is described by equation (3.3). In S_n recombination in the bulk is taken into account by τ_b as $S_n = \Delta n / \tau_b$, where Δn is the excess charge carrier injected under illumination. The electron current is, in this simple case, just diffusion current (without electric field which produces drift currents). This current is obtained as a result of a gradient in the carrier concentration due to the exponential generation profile: $j_n(x) = -D \frac{\partial}{\partial x} \Delta n(x)$, with D as the diffusion constant of electrons.

Introducing all the described terms the steady state continuity equation of electrons is given by:

$$-D \frac{\partial^2}{\partial x^2} \Delta n(x) + \alpha(1 - R) \phi_i \exp(-\alpha(d - x)) - \frac{\Delta n(x)}{\tau_b} = 0 \tag{3.17}$$

The illumination falls into the surface at $x = d$ and the PL detection is also done from the same side. For solving this differential equation two boundary conditions are needed, which state that the minority carriers that reach the surface recombine there. These conditions can be described by the surface recombination velocities at

each boundary (S_0 and S_d) because the carrier distribution is strongly influenced by the non-radiative recombination at the surfaces:

$$\begin{aligned} D \frac{\partial}{\partial x} \Delta n(0) &= S_0 \Delta n(0) \\ D \frac{\partial}{\partial x} \Delta n(d) &= -S_d \Delta n(d) \end{aligned} \quad (3.18)$$

The solution of the differential equation is [19, 34]:

$$\Delta n(x) = A \exp(x/L) + B \exp(-x/L) + C \exp(-\alpha(d-x)) \quad (3.19)$$

being $L = \sqrt{\tau_b D}$ the diffusion length and the constants A, B, C:

$$\begin{aligned} A &= C \frac{(\frac{S_d L}{D} + \alpha L)(1 + \frac{S_0 L}{D}) + (\frac{S_0 L}{D} - \alpha L)(1 - \frac{S_d L}{D}) \exp(d(-\alpha - 1/L))}{(1 - \frac{S_0 L}{D})(1 - \frac{S_d L}{D}) \exp(-d/L) - (1 + \frac{S_0 L}{D})(1 + \frac{S_d L}{D}) \exp(d/L)} \\ B &= C \frac{(\frac{S_d L}{D} + \alpha L)(1 - \frac{S_0 L}{D}) + (\frac{S_0 L}{D} - \alpha L)(1 + \frac{S_d L}{D}) \exp(d(-\alpha - 1/L))}{(1 - \frac{S_0 L}{D})(1 - \frac{S_d L}{D}) \exp(-d/L) - (1 + \frac{S_0 L}{D})(1 + \frac{S_d L}{D}) \exp(d/L)} \\ C &= \frac{\tau \alpha \Phi_i (1 - R)}{1 - \alpha^2 L^2} \end{aligned} \quad (3.20)$$

Chapter 4

Non-radiative recombination

The total recombination rate of the excess of minority charge carriers is strongly influenced by non-radiative processes (in c-Si at moderate temperatures). The latter are mainly due to Auger recombination, recombination via impurities and surface recombination. Auger recombination occurs when free energy obtained during recombination is transferred to an electron or a hole as kinetic energy which is subsequently dissipated by emission of multiple phonon till the charge carrier reach the band edge. These processes always imply three particles, i.e, two electrons and one hole or two holes and one electron [35]. The Auger recombination is defined as following:

$$\begin{aligned} R_{eeh} &= C_n n^2 p & R_{ehh} &= C_p n p^2 \\ R_A &= R_{eeh} + R_{ehh} \end{aligned} \quad (4.1)$$

where C_n and C_p are the Auger capture coefficients of electrons and holes, and they have values around $10^{-31} \text{ cm}^6 \text{ s}^{-1}$ [36]. Due to the quadratic dependance, Auger recombination is the determining recombination mechanism for high charge carrier concentrations, as under high excitation intensity. So far, Auger recombination is an unavoidable loss and thus an upper limit for the efficiency of solar cells.

Deep impurities are usually situated in the middle of the forbidden gap between valence and conduction band. Recombination via these defects is described by the Shockley-Read-Hall (SRH) theory [37, 19] and its rate is given by:

$$R_{SRH} = \frac{np - n_i^2}{\tau_{c,p} \left[n + n_i \exp \left(\frac{E_t - E_i}{kT} \right) \right] + \tau_{c,n} \left[p + n_i \exp \left(\frac{E_i - E_t}{kT} \right) \right]} \quad (4.2)$$

where

$$\tau_{c,p} = \frac{1}{\sigma_p v_{th} N_i} \quad \tau_{c,n} = \frac{1}{\sigma_n v_{th} N_i} \quad (4.3)$$

being σ_n and σ_p the capture cross-section of electrons and holes in the material (typical values around 10^{-15}cm^2 [19]), v_{th} is their thermal velocity ($\sim 10^7 \text{cm s}^{-1}$ in Si at 300K), N_i is the concentration of impurities and E_i their energy level. $\tau_{c,n}$ and $\tau_{c,p}$ are the capture time constants of electrons and holes. n_i is the density of impurities.

The existence of a high number of non-saturated Si-bonds, energetically distributed within the band gap is responsible for the recombination at the surface. These defects can also be described using the SRH theory, taking the total recombination rate as the sum of the contributions from each energy interval, which can be determined if the concentration of surface states and its capture cross-sections are known. This recombination is characterized by a surface recombination velocity, S :

$$R_{s,n} = \sigma_{s,n} v_{th} p_s n_s = S_n n_s \quad (4.4)$$

where $R_{s,n}$ is the recombination rate of electrons per area, n_s and p_s are the concentration of electrons and holes at the surface. The surface recombination velocity of electrons, S_n is characteristic of the surface quality, but it is not a material quality as it is dependent on the excitation conditions by the occupation of the surface states. For bulk impurities, surface states situated energetically at mid-gap are most effective for recombination.

Recombination via impurities or surface defects can be reduced or eliminated by material treatment. In the case of silicon, surfaces just exposed to air evolve an amorphous SiO_x layer that produces a high density of states in the band gap, and therefore a larger surface recombination velocity ($S \geq 10^3 \text{cm/s}$). Recombination at the silicon surface can be reduced using different passivation techniques as thermally grown SiO_2 , remote plasma silicon nitride or deposition of amorphous silicon. All these passivation methods reduce the surface recombination velocities at silicon surfaces to values of ca. 10cm/s or less [38, 39, 27]. Besides, wafer pretreatments before deposition of the passivation layer influence the density of surface defects and therefore play an important role in the recombination [40]. For example, it has been found that HF-dip decreases surface defect densities in comparison to a RCA wafer pretreatment [41]. In our case, dealing with a-Si:H/c-Si heterostructures, the interface defect density plays a very important role in the performance of the solar cells [11, 24, 42].

Chapter 5

Experimental setup

The experimental setup for photoluminescence measurements is shown in Fig. 5.1.

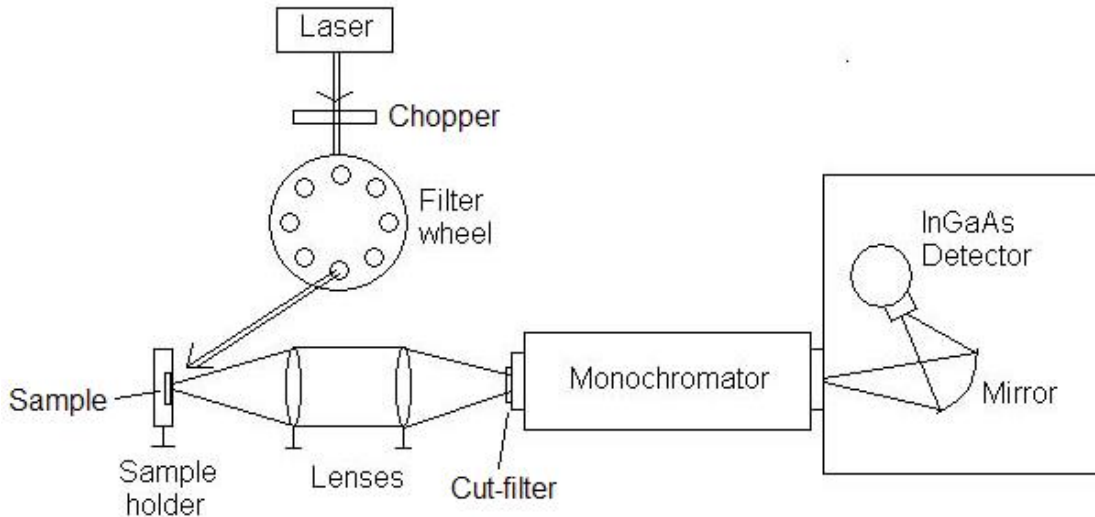


Figure 5.1: Sketch of photoluminescence setup. The filter wheel can be used to get different excitation intensities.

Samples were illuminated with a laser diode at a wavelength of 782 nm. A filter wheel is placed between the laser and the sample holder to get different excitation intensities. The laser beam is focused on a spot (radius around 1 mm) on the sample surface. Photoluminescence is collected by a system of lenses and focused to the entrance of a monochromator, which separates photons at different wavelengths. Photons coming through the monochromator are collected by a mirror and focused to the detection area of an InGaAs detector. This mirror and the detector are placed inside a metal box to avoid noisy photons. Photons coming from the laser are absorbed by a cut-filter at 830 nm just at the entrance of the monochromator. The signal produced by photons in the detector is measured by lock-in technique. The filter wheel rotation and the monochromator are automatized by a computer as well as the data reading.

Calibration of the setup in order to get absolute measurements was done using a tungsten lamp, which emits the already well known black body radiation at a determined temperature of $T = 2500 \pm 50K$. The lamp was situated in the same position as the samples and a 1 mm diameter pinhole was used at the entrance of the monochromator in order to have the same collected solid angle in both measurements, calibration and photoluminescence.

When working with solar cells, photoluminescence was measured at different operating points. In this case a voltage source was connected to the samples.

Chapter 6

Quantitative measurements of photoluminescence of absorbers with passivation layers

Luminescence measurements were calibrated as described in Appendix D in order to get quantitative photoluminescence. The calibration of a photoluminescence setup allows the access to quantities as the splitting of quasi-Fermi levels or effective lifetimes of the materials investigated.

Passivation of interface defects is a very determinant step in the improvement of the performance of a-Si:H/c-Si solar cells. In this chapter I analyze the influence of different passivation layers deposited on a standard (p)c-Si substrate via the $E_{F_n} - E_{F_p}$ obtained from quantitative PL. From these measurements, the effective lifetime has been derived. Furthermore the non-linearity of PL versus excitation intensities has been studied.

6.1 Determination of quasi-Fermi level splitting

Determination of the splitting of quasi-Fermi levels is only achieved when the photoluminescence measurements are absolutely calibrated, so that the spectrum obtained can be quantitatively described in equation (3.15) from chapter 3. In the samples examined, passivation at the front and back of the silicon wafer was the same so that optical reflection at both sides has been considered identical. Furthermore, as the passivation is done with SiN and a-Si:H, being both excellent for defect passivation at silicon surfaces, a nearly constant distribution of carriers at the bulk has been assumed. This implies that the spatial dependence of the splitting of quasi-Fermi levels can be neglected and the photoluminescence of the studied wafer is approximately described by the following formula

$$\begin{aligned}
dn_\gamma(\hbar\omega) &= \frac{\alpha(\hbar\omega)(\hbar\omega)^2}{4\pi^3 c_o^2 \hbar^3} \times \frac{[1 - R(\hbar\omega)] \exp[-\alpha(\hbar\omega)d]}{1 - \exp[-2\alpha(\hbar\omega)d] R(\hbar\omega)^2} d(\hbar\omega) \\
&\quad \times \int_0^d \frac{\exp[\alpha(\hbar\omega)x] + R(\hbar\omega) \exp[-\alpha(\hbar\omega)x]}{\exp\left[\frac{\hbar\omega - (E_{F_n} - E_{F_p})}{kT}\right] - 1} dx \\
&= \frac{(\hbar\omega)^2}{4\pi^3 c_o^2 \hbar^3} \times \frac{[1 - R(\hbar\omega)][1 - \exp(-\alpha(\hbar\omega)d)]}{1 - R(\hbar\omega) \exp(-\alpha(\hbar\omega)d)} \times \frac{d(\hbar\omega)}{\exp\left[\frac{\hbar\omega - (E_{F_n} - E_{F_p})}{kT}\right] - 1} \\
&= A(\hbar\omega) \times \frac{(\hbar\omega)^2}{4\pi^3 c_o^2 \hbar^3} \times \frac{d(\hbar\omega)}{\exp\left[\frac{\hbar\omega - (E_{F_n} - E_{F_p})}{kT}\right] - 1} \tag{6.1}
\end{aligned}$$

where $R_F(\hbar\omega) = R_B(\hbar\omega) = R(\hbar\omega)$ and $A(\hbar\omega)$ is the absorbance of the sample calculated considering multi-reflection at both surfaces of the sample as indicated in section 3 of chapter 3.

The splitting of quasi-Fermi levels is obtained by fitting an analytical curve obtained from the previous equation (6.1) to the measured and calibrated photoluminescence curve. The parameter d is already known, R is obtained as indicated in the formula (3.1) from chapter 3 for the a-Si:H passivation and from reflection measurements for the SiN layer. α for (p)c-Si is obtained from literature [8], so that the only adjustable variable is $E_{F_n} - E_{F_p}$.

The error in $E_{F_n} - E_{F_p}$ calculated from the calibration is ± 4 meV ($\approx 1\%$). More details about the error calculation can be found in Appendix A.

6.1.1 Results

The splitting of quasi-Fermi levels was calculated as described for 7 different passivation layers. The substrate was the same for all the samples: a (p)c-Si monocrystalline substrate with low resistivity ($\sim 1\Omega cm$) which is a typical standard material for the manufacturing of solar cells. One sample, with a thickness of $273\ \mu m$, was passivated with SiN deposited by the remote plasma technique at the Institut für Solarenergieforschung in Hameln (Germany). The other 6 samples were passivated with differently doped a-Si:H layers and have a thickness of $250\ \mu m$. Three of the samples with amorphous silicon layers had an HF-dip wafer pretreatment before deposition (at the Hahn Meitner Institut in Berlin). The other three wafers were passivated using a standard RCA pretreatment (at the Fern Universität Hagen).

In the calculation of the analytical curves of photoluminescence spectra, given

in equation (6.1), no wavelength dependence was considered in the reflection coefficient, i.e. in the refraction indices. Instead of that an average value centered at the maximum of the PL-yield was used. This assumption can evolve in variations of the calculations from the experimental spectra. In order to solve this problem, the influence of this averaged refraction index in the PL-spectra has been studied. In Figure 6.1 the calculated absorptivity for the SiN-passivation is depicted. The three curves were obtained as following. It was considered a measured reflexion of $R = 0.23$, which implies a refraction index of $n = 2.84$ of the silicon wafer. With a reasonable error of 5% in the determination of n , I calculated the values $n = 2.7$ ($R = 0.21$) and $n = 3$ ($R = 0.25$). Figure (6.1) shows the variation of the absorptivity $A(\hbar\omega)$ for the calculated values of n and R . These differences are translated in a variation at the maximum of the spectrum, when fitting the analytically calculated curve from equation (6.1) to the measured ones. These fittings can be detected in Figure 6.2. The best fit is obtained for a refraction index of $n = 3$ and $R = 0.25$, giving a splitting of quasi-Fermi levels of 723 meV.

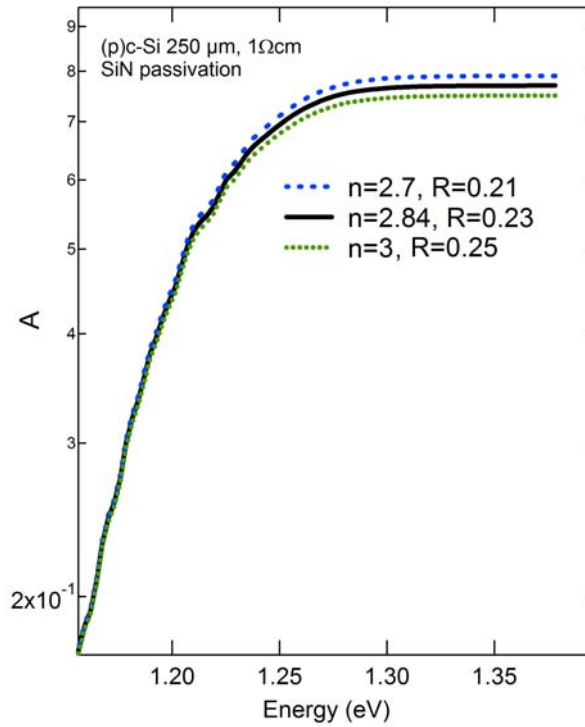


Figure 6.1: Absorptivity A calculated for a (p)c-Si wafer passivated with silicon nitride. The different curves were obtained considering refraction indexes $n = 2.7, 2.84, 3$.

Figure 6.3 shows the quantitative photoluminescence measurements. The spectra were obtained at room temperature and at an excitation intensity of about $4 \times AM1.5$ using a laser diode with a wavelength of 782 nm. The result from Figure 6.1 was used to match the experimental to the calculated curve for silicon

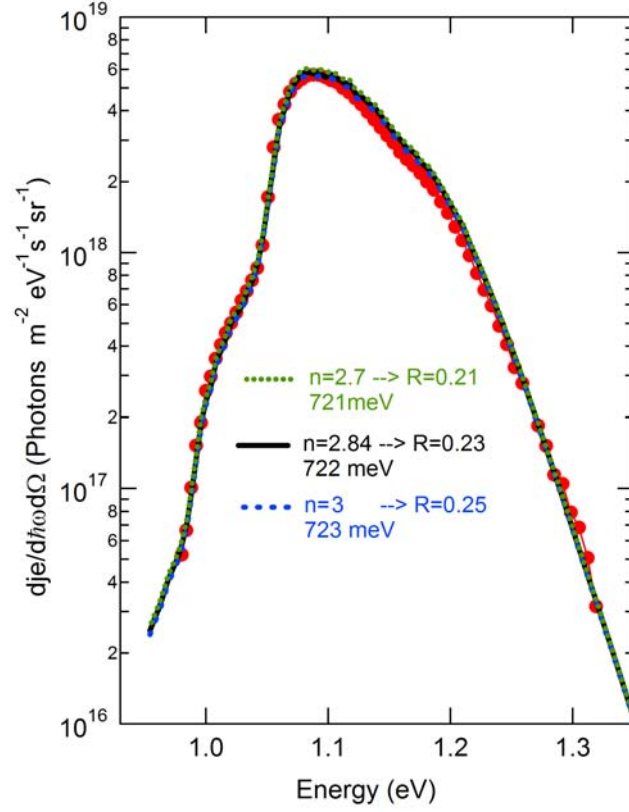


Figure 6.2: Measured photoluminescence (red dots) and analytical PL-yield calculated for a (p)c-Si wafer passivated with silicon nitride. The three different fitting curves were obtained with the absorbance from figure (6.1).

nitride passivation. There is a good match for the a-Si:H layers for an average refraction index of silicon $n = 3.5$ and $R = 0.309$. Therefore, this 3 layer system a-Si:H/ c-Si/a-Si:H can be approximately treated as a 1 layer system air/c-Si/air, neglecting the effect of the amorphous silicon films, in the calculation of the reflection.

The silicon nitride passivation shows the highest PL yield of the series with a value of 723 meV in the splitting of quasi-Fermi levels. It is followed by the intrinsic amorphous silicon layers with a difference of ca. 30 meV in the $E_{F_n} - E_{F_p}$, for both wafer pretreatments, with the SiN passivation. 695 and 653 meV are the splittings in the quasi-Fermi energies for the deposited (n)a-Si:H with HF-dip wafer pretreatment. The RCA process for the (p)a-Si:H and (n)a-Si:H passivation layers results in $E_{F_n} - E_{F_p}$ of 650 and 581 meV, respectively.

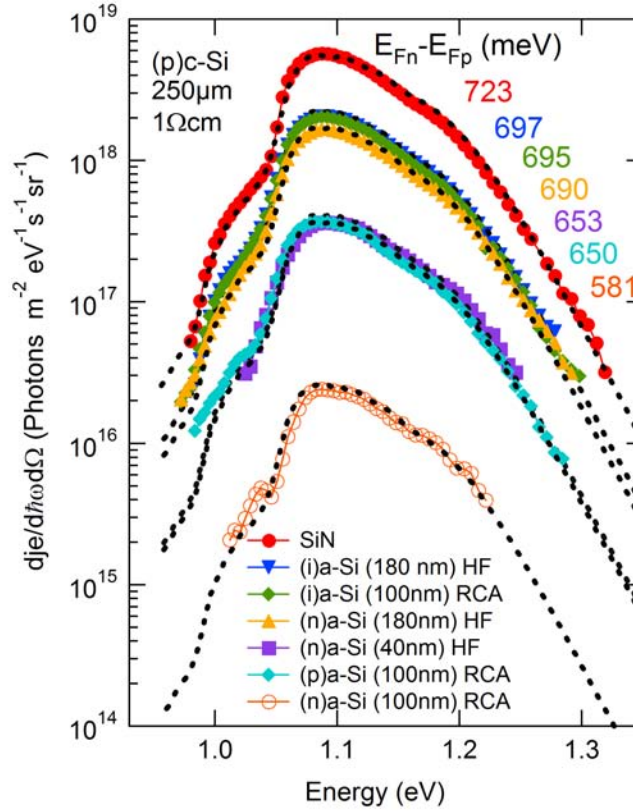


Figure 6.3: Quantitative photoluminescence spectra of a monocrystalline (p)c-Si wafer with different passivation layers. Splitting of quasi-Fermi levels has been derived from each of the curves. The best passivation was found for SiN_x, followed by (i)a-Si. HF-dip as a cleaning pretreatment shows in general better results than the RCA-process. The dotted curves show the modelled functions.

6.2 Calculation of effective lifetime

6.2.1 Definition: bulk lifetime and effective lifetime

All recombination mechanisms described in chapters 3 and 4 determine the lifetime of the excess carriers Δn generated in the semiconductor. Total recombination rate (R_b) in the bulk is calculated as the sum of rates from band-band (R_{bb}), defect and impurity transitions (R_{SRH}) and Auger processes (R_A):

$$R_b = R_{bb} + R_{SRH} + R_A \quad (6.2)$$

For each recombination process a lifetime can be defined. For a p-doped material under low injection conditions:

$$\tau_{bb} = \frac{\Delta n}{R_{bb}} \quad \tau_{SRH} = \frac{\Delta n}{R_{SRH}} \quad \tau_A = \frac{\Delta n}{R_A} \quad (6.3)$$

and the total recombination lifetime is given by

$$\frac{1}{\tau_b} = \frac{1}{\tau_{bb}} + \frac{1}{\tau_{SRH}} + \frac{1}{\tau_A} \quad (6.4)$$

If there is recombination at the surface it is necessary to define an effective lifetime which takes into account all the recombination processes R_{tot} in the volume and at the surface of the sample. It is defined as:

$$\tau_{eff} = \frac{\Delta n_{tot}}{R_{tot}} \quad (6.5)$$

where Δn_{tot} is the excess of minority carriers recombined in the bulk and at the surface of the wafer. If there is no surface recombination, $\tau_{eff} = \tau_b$.

6.2.2 Effective lifetime from photoluminescence

Taking into account equation (3.4) in chapter 3 and with the definition of the intrinsic carrier density $n_i = \sqrt{N_C N_V} \exp(-E_g/2kT)$, $E_g = E_C - E_V$, the splitting of quasi-Fermi levels for non-degenerated semiconductors, i.e., $E_{F_n} + 3kT < E_C$ and $E_{F_p} - 3kT > E_V$, which is verified in our case, can be expressed by:

$$E_{F_n} - E_{F_p} = kT \ln \left(\frac{np}{n_i^2} \right) \quad (6.6)$$

Assuming that in our samples of high quality crystalline silicon the density of bulk deep impurities (i.e. metal introduced in the crystallization process) is very low in comparison to the doping and valence band and conduction band density of states, N_i can be neglected in the 'balance charge neutrality' equation:

$$n + N_A^- = p \quad (6.7)$$

being N_A^- the density of ionized acceptor atoms. Substituting the following expressions in (6.7),

$$n = n_0 + \Delta n \quad p = p_0 + \Delta p \quad N_A^- = N_{A,0}^- - \Delta N_A \quad (6.8)$$

where n_0 , p_0 and $N_{A,0}^-$ are the electron, hole and ionized acceptor densities without illumination and Δn , Δp and ΔN_A , the variation in the latter quantities introduced by light; it can be obtained:

$$n_0 + \Delta n + N_{A,0}^- - \Delta N_A = p_0 + \Delta p \quad (6.9)$$

For a p-doped semiconductor and the conditions of the experiment here: $n_0 \ll \Delta n$, $N_{A,0}^-$, p_0 and thus n_0 can be neglected. ΔN_A can also be neglected for no high injection $N_A^- = N_{A,0}^-$. At room temperature, all the acceptors are ionized, thus $N_{A,0}^- = N_A$:

$$\Delta n + N_A = p_0 + \Delta p \quad (6.10)$$

Knowing the splitting of quasi-Fermi levels from photoluminescence measurements and expanding the product of n and p :

$$np = (n_0 + \Delta n)(p_0 + \Delta p) = n_0 p_0 + \Delta n p_0 + \Delta n \Delta p + n_0 \Delta p \quad (6.11)$$

with $n_i^2 = n_0 p_0$, $p_0 \approx N_A$ and $\Delta n \approx \Delta p$.

$$np \approx n_i^2 + \Delta n N_A + \Delta n^2 + n_0 \Delta n = n_i^2 + (N_A + n_0) \Delta n + \Delta n^2 \quad (6.12)$$

using the approximation: $n_0 \ll N_A \Rightarrow N_A + n_0 \approx N_A$:

$$np \approx n_i^2 + N_A \Delta n + \Delta n^2 = n_i^2 + \Delta n (N_A + \Delta n) \quad (6.13)$$

Introducing (6.13) in (6.6):

$$E_{F_n} - E_{F_p} = kT \ln \left[1 + \frac{\Delta n}{n_i^2} (\Delta n + N_A) \right] \quad (6.14)$$

Transforming the previous expression (6.14) in a quadratic equation, Δn can be solved:

$$\begin{aligned} \Delta n^2 + \Delta n N_A - n_i^2 \left[\exp \left(\frac{E_{F_n} - E_{F_p}}{kT} \right) - 1 \right] &= 0 \\ \Rightarrow \Delta n &= \frac{-N_A \pm \sqrt{N_A^2 + 4n_i^2 \left[\exp \left(\frac{E_{F_n} - E_{F_p}}{kT} \right) - 1 \right]}}{2} \end{aligned} \quad (6.15)$$

where only the positive result should be considered.

An effective lifetime from PL can be defined as:

$$\tau_{eff,PL} = \frac{\Delta n}{\bar{R}} \quad (6.16)$$

with Δn accounted for the previous expression (6.15) and \bar{R} is the total recombination rate, averaged over the whole structure taking into account the recombination in the bulk and at the surface as we are calculating an effective lifetime.

And in steady state, generation equals recombination: $\bar{R} = \bar{G}$:

$$\tau_{eff,PL} = \frac{\Delta n}{\bar{G}} \quad (6.17)$$

The value of the generation rate is:

$$\overline{G} = \frac{\int_0^d -\frac{\partial \Phi(x)}{\partial x} dx}{\int_0^d dx} = \frac{\Phi_i(1-R)[1 - \exp(-\alpha d)]}{d} \quad (6.18)$$

being $\phi(x)$ given by (3.3) in chapter 3.

Introducing the positive value of (6.15) and (6.18) in (6.17):

$$\tau_{eff,PL} = \frac{d \left(-N_A + \sqrt{N_A^2 + 4n_i^2 \left[\exp\left(\frac{E_{Fn}-E_{Fp}}{kT}\right) - 1 \right]} \right)}{2\Phi_i(1-R)[1 - \exp(\alpha d)]} \quad (6.19)$$

I have found an expression of the effective lifetime τ_{eff} as a function of the splitting of quasi-Fermi levels which can be calculated from PL.

6.2.3 Results

With the splitting of quasi-Fermi levels obtained in section 1.1.1, the effective lifetime $\tau_{eff,PL}$ has been calculated using the formula (6.19). The results are collected in Table 6.1.

	$E_{Fn} - E_{Fp}$ (eV)	$\Delta n (cm^{-3})$	$\tau_{eff,PL} (\mu s)$
SiN	0.723 ± 4	$(9.1 \pm 1) \times 10^{15}$	227 ± 23
(i)a-Si (180nm) HF	0.697 ± 0.004	$(4.3 \pm 0.5) \times 10^{15}$	108 ± 12
(i)a-Si (100nm) RCA	0.695 ± 0.004	$(4 \pm 0.5) \times 10^{15}$	100 ± 12
(n)a-Si (180nm) HF	0.69 ± 0.004	$(3.4 \pm 0.4) \times 10^{15}$	86 ± 10
(n)a-Si (40nm) HF	0.653 ± 0.004	$(1 \pm 0.1) \times 10^{15}$	25 ± 4
(p)a-Si (100nm) RCA	0.65 ± 0.004	$(9 \pm 1) \times 10^{14}$	22 ± 3
(n)a-Si (100nm) RCA	0.581 ± 0.004	$(6.5 \pm 1) \times 10^{13}$	2

Table 6.1: Splitting of quasi-Fermi levels, electron excess density and effective lifetime for the various passivated samples.

For the calculation of Δn with the equation (6.15) the values of the intrinsic carrier concentration (n_i) and doping concentration (N_A) are also needed. $n_i = 1.213 \times 10^{10} cm^{-3}$ was determined using $kT = 0.0259$ eV and the values $N_C = 2.86 \times 10^{19} cm^{-3}$, $N_V = 3.1 \times 10^{19} cm^{-3}$, $E_g = 1.12$ eV from reference [43]. $N_A = 1.25 \times 10^{16} cm^{-3}$ was estimated assuming a specific resistivity of $\rho = 1 \Omega cm$ and a hole mobility of $\mu_p = 500 cm^2 V^{-1} s^{-1}$. The generation rate $\overline{G} \approx 4 \times 10^{19} cm^{-3} s^{-1}$ was derived from the photon flux used in the measurements, i.e., $\Phi_i = 1.6 \times 10^{18} cm^{-2} s^{-1}$, and a value of $1010 cm^{-1}$ for the absorption coefficient was taken for the excitation wavelength $\lambda = 782 nm$. Reflection of 23% was taken into account for the SiN passivation. For the samples with the different amorphous silicon layers, a reflection

coefficient $R=0.306$ was used. In Table 6.1 there is an error for the excess electron density and effective lifetime. An error bar of ± 4 meV for the determination of the splitting of quasi-Fermi levels has been derived. The calculation of the error is described in Appendix A. This error derives from the inaccuracy in the determination of $E_{F_n} - E_{F_p}$ (see Appendix A) and involves an uncertainty of around 10% in the effective lifetime determined from the PL-yield.

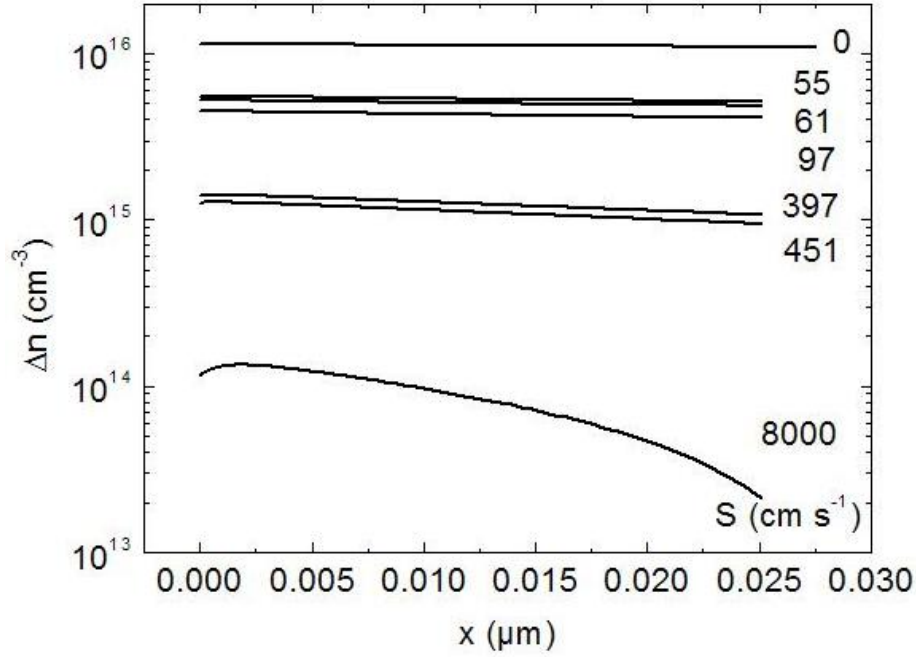


Figure 6.4: Excess carrier densities from the simulation of continuity equation (equation 3.17) for a silicon wafer with an effective lifetime of $250 \mu s$ and different surface recombination velocities (same values S for front and rear side). The higher the surface recombination, the more spatially inhomogeneous is $\Delta n(x)$. The same excitation intensity as in the experiments has been taken.

Figure 6.4 shows the electron excess density over the thickness of the wafer. Δn has been calculated solving the continuity equation according to section 5 of chapter 3. I have considered a diffusion length of $L = 930 \mu m$, which corresponds to a lifetime of $250 \mu s$. L is larger than the thickness of the wafer, so that carriers that diffuse can reach the surface and suffer recombination. This is the largest diffusion length obtained in our calculation and therefore, a very illustrative case for the evaluation of the influence of the surface recombination in the homogeneity of the spatial distribution of the carrier densities and thus the splitting of quasi-Fermi levels. Introducing the bulk lifetime in the continuity equation, different surface recombination velocities, from 0 to 8000 cm s^{-1} have been applied, obtaining the spatial dependence of the excess electron density.

When the carrier densities are not spatially constant, $\tau_{eff,PL}$ is averaged. From the previous simulation, the local variation of carrier densities shows a local effective lifetime. In Table 6.2, the maximum and minimum values of Δn and the difference in percentage to the averaged value are shown. For values up to 451 cm s^{-1} , this percentage difference reaches the value of 15%. For $S = 8000 \text{ cm s}^{-1}$, which is a non-realistic value for well passivated wafers, local variations around 60 % can be reached. Furthermore, in this case, local deviations for well passivated wafers ($S < 100 \text{ cm s}^{-1}$) have local differences up to 5% and the calculation of the splitting of quasi-Fermi levels implies an inaccuracy 10%.

$S(\text{cm s}^{-1})$	$\Delta n_{max}(\text{cm}^{-3})$	$\Delta n_{min}(\text{cm}^{-3})$	$\Delta n_{eff,PL}(\text{cm}^{-3})$
0	$1.144 \times 10^{16} (4\%)$	$1.099 \times 10^{16} (1\%)$	1.11×10^{16}
55	$5.52 \times 10^{15} (4\%)$	$5.15 \times 10^{15} (3\%)$	5.32×10^{15}
61	$5.23 \times 10^{15} (4\%)$	$4.86 \times 10^{15} (3\%)$	5.03×10^{15}
97	$4.49 \times 10^{15} (5\%)$	$4.12 \times 10^{15} (4\%)$	4.29×10^{15}
397	$1.41 \times 10^{15} (13\%)$	$1.078 \times 10^{15} (14\%)$	1.25×10^{15}
451	$1.276 \times 10^{15} (14\%)$	$9.47 \times 10^{14} (15\%)$	1.11×10^{15}
8000	$1.34 \times 10^{14} (61\%)$	$2.11 \times 10^{13} (25\%)$	8.33×10^{13}

Table 6.2: Local maximum, minimum and average (integrated) excess of electron density calculated for a wafer with a bulk lifetime of $250 \mu\text{s}$ for different surface recombination velocities.

6.3 Dependence on intensity

As the spectral distribution of PL does not change with the excitation intensity, the photoluminescence dependence on intensity has been evaluated just at the wavelength for the maximum emission ($\lambda \approx 1130 \text{ nm}$). Figure 6.5 shows the measured photoluminescence at different generation rates over one order of magnitude ($\bar{G} = 7 \times 10^{19} \dots 7 \times 10^{20} \text{ cm}^{-3} \text{ s}^{-1}$) for the sample passivated with silicon nitride and for one of the samples passivated with (i)a-Si:H. The measured values have been calibrated as explained in chapter 3. The slope of the curves are 1.26 and 1.38, showing a non-linear behaviour of the emission of photons versus the excitation intensity. As it has been explained, PL is proportional to the effective lifetime, therefore, this non-linearity is also detected in $\tau_{eff,PL}$. At first view, this effect can be explained via three different ways:

1. The surface recombination velocity is constant and the bulk lifetime increases with Φ ,
2. Bulk lifetime is constant over the considered \bar{G} range, but surface recombination velocity decreases for higher generation rates.

3. the non-linearity is due to variation in the bulk lifetime together with changes in the surface recombination velocities for different excitation intensities.

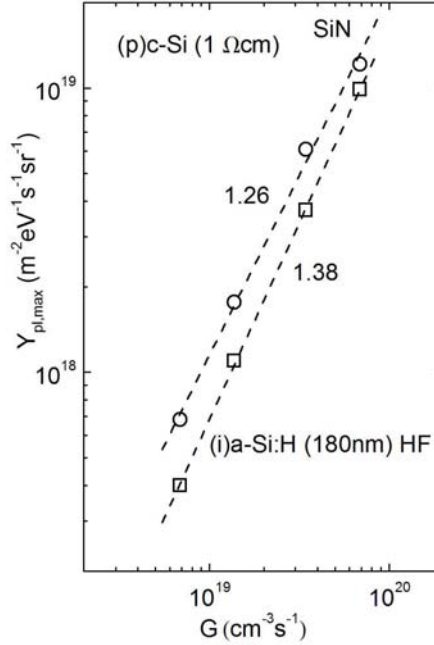


Figure 6.5: Intensity dependence of photoluminescence measured at maximum emission wavelength for the (p)c-Si wafer with silicon nitride passivation and for one of the samples passivated with intrinsic amorphous silicon.

6.3.1 Dependence of bulk lifetime on intensity

In order to study the intensity dependence of the bulk lifetime I will simulate the recombination of a four energy level system [44]. The energy levels are the conduction band, the valence band and two defect levels (one deep impurity level and one doping level) in between as shown in Figure 6.6.

The Shockley-Read-Hall model [37, 45] was applied, characterized by having two recombination centers with capture coefficients $\beta_{ij} = \sigma_{ij}v_{th}$ (σ_{ij} is the capture cross section of level j for the free carriers from level i and $v_{th} \approx 10^7 \text{ cm s}^{-1}$ is the average thermal velocity of the free carrier) and with thermal excitation between the levels and both the conduction and the valence bands. In this case it is possible to write 4 rate equations:

$$\frac{dn}{dt} = G - R_{Ci} - R_{CA} - R_{CV} + G_{iC} + G_{AC} + G_{VC} \quad (6.20)$$

$$\frac{dn_i}{dt} = R_{Ci} - R_{iA} - R_{iV} - G_{iC} + G_{Ai} + G_{Vi} \quad (6.21)$$

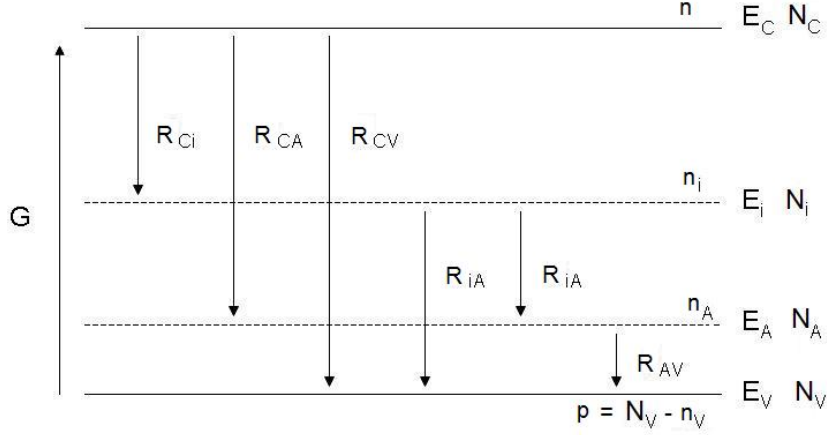


Figure 6.6: Sketch of the recombination model considered in the simulation of the bulk lifetime. A four energy level system has been chosen: the valence and conduction band, an energy level in the middle of the gap to represent deep impurities in silicon and the doping acceptor level E_A , which in this case has been drawn too far away from the valence band in order to facilitate the view of the recombination rates. All possible recombination channels between the four levels are shown in the figure. Thermal generation rates, which are not shown, would be the same ones but changing the direction of the arrows.

$$\frac{dn_A}{dt} = R_{CA} + R_{iA} - R_{AV} - G_{AC} - G_{Ai} + G_{VA} \quad (6.22)$$

$$\frac{dp}{dt} = G + G_{VC} + G_{Vi} + G_{VA} - R_{CV} - R_{iV} - R_{AV} \quad (6.23)$$

where n , n_i , n_A are the electron densities at the conduction band, at the defect level and at the doping (acceptor in this case) level and p is the hole density at the valence band. G is the applied generation rate and the terms R_{jk} are the recombination rates between level j and k and G_{kj} are the thermal generation rates in the opposite direction. The indices C, V, i and A correspond to the conduction band, valence band, intrinsic impurity and acceptor level, respectively. The next step is the calculation of the recombination and thermal excitation rates. Kinetic arguments are considered for the determination of the recombination rate. When an electron (hole) moving through the lattice reaches the capture cross section σ of an atom with a hole (electron), it will recombine there. In this model, we consider that no electron capture takes place if the atom is already occupied by an electron because the energy of this second electron may be very high and in the range of the conduction band (Pauli Principle). The possible rates for our 4-level system are the following:

$$\begin{aligned} R_{Ci} &= \beta_{Ci} n (N_i - n_i) \\ R_{CA} &= \beta_{CA} n (N_A - n_A) \end{aligned}$$

$$\begin{aligned}
R_{CV} &= \beta_{CV}np \\
R_{iA} &= 0 \\
R_{iV} &= \beta_{iV}n_i p \\
R_{AV} &= \beta_{AV}n_A p
\end{aligned} \tag{6.24}$$

Thermal generation rates can be calculated using the Principle of Detailed Balance in the dark and considering that, due to the rapid thermalization, electrons and holes have the same energy and velocity distribution under illumination and in the dark. Therefore, equaling recombination and emission rates in a steady state ($G=0$) for each recombination channel and knowing the density of electrons in the dark described by the Fermi distribution, the emission coefficient can be found and therefore generation rates are given by:

$$\begin{aligned}
G_{iC} &= \beta_{Ci} \exp((E_i - E_C)/kT) n_i (N_C - n) \\
G_{AC} &= \beta_{CA} \exp((E_A - E_C)/kT) n_A (N_C - n) \\
G_{VC} &= \beta_{CV} \exp(-E_C/kT) (N_V - p) (N_C - n) \\
G_{Ai} &= 0 \\
G_{Vi} &= \beta_{iV} \exp(-E_i/kT) (N_V - p) (N_i - n_i) \\
G_{VA} &= \beta_{AV} \exp(-E_A/kT) (N_V - p) (N_A - n_A)
\end{aligned} \tag{6.25}$$

where it has been assumed that there is neither recombination nor thermal generation between the defect level and the doping level. In our case it has been considered the valence band $E_V = 0$ eV, thus, for crystalline silicon, conduction band is at $E_C = 1.12$ eV. The doping level is located at $E_A = 0.045$ eV (boron doped) and the intrinsic defect level is placed in the middle of the gap, i.e., $E_i = 0.55$ eV. The density of states are: $N_C = 2.9 \times 10^{19} \text{ cm}^{-3}$, $N_V = 3.1 \times 10^{19} \text{ cm}^{-3}$ [43], $N_A = 1.2 \times 10^{16} \text{ cm}^{-3}$ ($\rho \approx 1 \Omega \text{ cm}$) and $N_i = 6.5 \times 10^{10} \text{ cm}^{-3}$.

In order to simulate the non-linearities from the PL measurements, two criteria were followed: 1) the 4 capture coefficients: β_{Ci} , β_{CA} , β_{iV} and β_{AV} were varied over a reasonable range of values and 2) the electron density n in the conduction band should have values within the densities obtained for the SiN passivation from the quantitative photoluminescence ($\Delta n \in (8 \times 10^{15}, 10^{16} \text{ cm}^{-3})$) (see Table 6.1). The recombination coefficient between the conduction and the valence band for the sample was measured from quantitative photoluminescence elsewhere [46] and has the value $\beta_{CV} = 5 \times 10^{-15} \text{ cm}^3 \text{ s}^{-1}$. Figures 6.7 and 6.8 show the band band recombination rate and the carrier densities versus generation rate when varying the recombination coefficient between the intrinsic defect level and the valence band β_{iV} within the range ($5 \times 10^{-10} \dots 10^{-8} \text{ cm}^3 \text{ s}^{-1}$). The other coefficients have the following values: $\beta_{Ci} = 10^{-7} \text{ cm}^3 \text{ s}^{-1}$, $\beta_{CA} = 10^{-10} \text{ cm}^3 \text{ s}^{-1}$, and $\beta_{AV} = 10^{-9} \text{ cm}^3 \text{ s}^{-1}$ in order to maintain Δn within the mentioned limits. In Figure 6.7 the curves show non-linearities in the same excitation range ($G \in (\sim 7 \times 10^{18} \dots \sim 7 \times 10^{19}) \text{ cm}^{-3} \text{ s}^{-1}$)

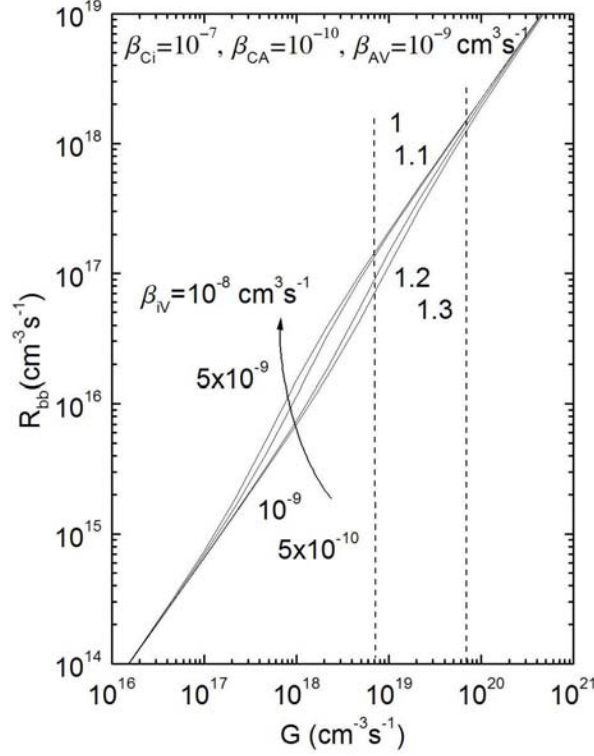


Figure 6.7: Band-band recombination ($R_{bb} = R_{CV}$) versus the generation rate resulted from the simulation of the 4-level model and SRH- recombination in the log-log scale. The different curves have been obtained varying the recombination coefficient between the intrinsic defect level and the valence band. Non-linearities appear in the curves in the same excitation range as in the PL measurements.

as in the PL measurements. Two dashed lines mark this range in both figures. The slopes vary from 1 to 1.3 when the coefficient β_{iV} is increased. The evolution of the carrier densities within G of the measurements show in Figure 6.8 that nearly all the doping atoms are ionized ($\approx 99.7\%$). The maximum of $n \approx \Delta n$ is one order of magnitude smaller than p_o and therefore low injection conditions ($\Delta n \ll p_o$) can not be assumed. Δn is just around half an order of magnitude larger than p_o , thus not following either high injection conditions ($n, p \gg n_o, p_o$). The measurements are done in a range in between. The non-linearities in the PL in the range of G studied are not only determined by the excess of the electron density but also by the hole density p because it is not any more constant. Finally, there are more neutral defects than positively charged ones.

6.3.2 Intensity dependance of the surface recombination velocity

Assumed the lifetime in the bulk to be constant.

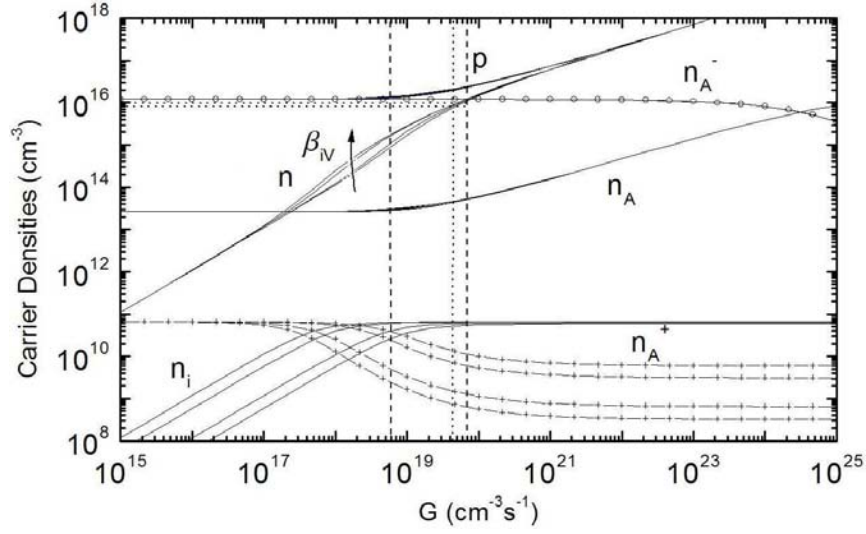


Figure 6.8: Carrier densities versus the generation rate as result of the simulation of the 4-level model and SRH-recombination. The different curves have been obtained varying the recombination coefficient between the intrinsic defect level and the valence band: $\beta_{iV} = 10^{-8} \dots 5 \times 10^{-10} \text{ cm}^3 \text{ s}^{-1}$.

Radiative recombination, i.e. the photoluminescence yield, is proportional to the product of electron and hole densities $Y_{pl} \propto np$. Under the definition of effective lifetime as $\Delta n/G$, for a p-doped semiconductor and under low injection conditions ($\Delta n, \Delta p \ll p_o$):

$$Y_{pl} \propto \Delta n \implies Y_{pl} \propto \tau_{eff,PL}(G) \cdot G \quad (6.26)$$

In the measurements, PL shows non-linearities versus excitation intensity. It has been assumed that they are proportional to G^m in the excitation range taken:

$$Y_{pl} \propto G^m \implies \tau_{eff,PL}(G) \propto G^{m-1} \quad (6.27)$$

so that $\tau_{eff,PL}(G)$ is also a monotone function if the PL increases monotonously. Effective lifetime is constant just only when the slope of Y_{pl} equals unity.

For the well passivated wafers, at $G \in (\sim 7 \times 10^{18}, \sim 7 \times 10^{19} \text{ cm}^{-3} \text{ s}^{-1})$, low injection conditions are not satisfied ($\Delta n, \Delta p$ are not $\ll p_o$). In this case:

$$\begin{aligned} Y_{pl} \propto n \cdot p &\approx \Delta n \cdot (p_o + \Delta p) = \Delta n \cdot (N_A + \Delta n) = (\Delta n)^2 + N_A \cdot \Delta n \\ &= (\tau_{eff,PL}(G) \cdot G)^2 + N_A \cdot G \cdot \tau_{eff,PL}(G) \end{aligned} \quad (6.28)$$

where we have used again $p_o + \Delta p = N_A + \Delta n$ from the neutrality equation as in section 6.2.2. Taking into account as above that $Y_{pl} \propto G^m$, the effective lifetime can be obtained solving the following quadratic equation:

$$(G \cdot \tau_{eff,PL}(G))^2 + N_A \cdot G \cdot \tau_{eff,PL}(G) - C \cdot G^m = 0$$

$$\Rightarrow \tau_{eff,PL}(G) = \frac{-N_A}{2G} + \frac{\sqrt{N_A^2 + 4C \cdot G^m}}{2G} \quad (6.29)$$

being C a constant. In this case the effective lifetime has a more complicated dependence on the excitation intensity than for low injection conditions.

Considering that photoluminescence does not change its spectral distribution when the excitation intensity is changed, the calibrated measurements of PL from Figure 6.5 can be used to obtain the splitting of quasi-Fermi levels for the different generation rates measured. First of all, the measured points in Figure 6.5 are fitted linearly in a double logarithmic scale and the fitted curve is used as extrapolated data. Afterwards, the maxima of the spectra from Figure 6.3 are compared with the PL maxima measured and the extrapolated data and differences are translated into differences of quasi-Fermi levels using

$$\Delta(E_{F_n} - E_{F_p}) = kT \ln \left(\frac{Y_{pl,max}}{Y_{max,s}} \right) \quad (6.30)$$

where $Y_{pl,max}$ is the photoluminescence yield at wavelength of maximum emission from the measurement at different G and $Y_{max,s}$ is the value of quantitative PL ($dn_\gamma/d(\hbar\omega)d\Omega$) at the same wavelength from the whole spectra measurements done for the determination of $(E_{F_n} - E_{F_p})_s$ of this sample (see Figure 6.3). Once this value is obtained, the splitting of quasi-Fermi levels at each G is determined as $(E_{F_n} - E_{F_p})_G = (E_{F_n} - E_{F_p})_s + \Delta(E_{F_n} - E_{F_p})$, the excess of electron density and thus, the effective lifetime are calculated just following the same steps as in section 6.2.2.

The results obtained from the explained calculations are depicted in Figure 6.9. The measured data are shown with open circles for the SiN passivation and with open squares for the (i)a-Si:H passivation. The extrapolated data is drawn with a dashed curve. The dotted curves mark the error obtained from the calculation of the splitting of quasi-Fermi levels (± 4 meV). Adding this error to the $E_{F_n} - E_{F_p}$ of the extrapolated data, an inaccuracy of Δn and $\tau_{eff,PL}$ using equations 6.15 and 6.17, respectively, was derived. The solid line was obtained using the formula (6.29) with the parameters of the sample: $N_A = 1.2 \times 10^{16} \text{ cm}^{-3}$ and $m = 1.26$ for the sample with the SiN layer and $m = 1.38$ for the (i)a-Si:H passivation. The constant C was varied till the curve fit the dashed curves.

At this point it should be noted that in the previous measurements and in the calculations of this section, lateral variations of the effective lifetimes and surface recombination velocity have not been taken into account. In the last section of this chapter a short evaluation of these variations is described.

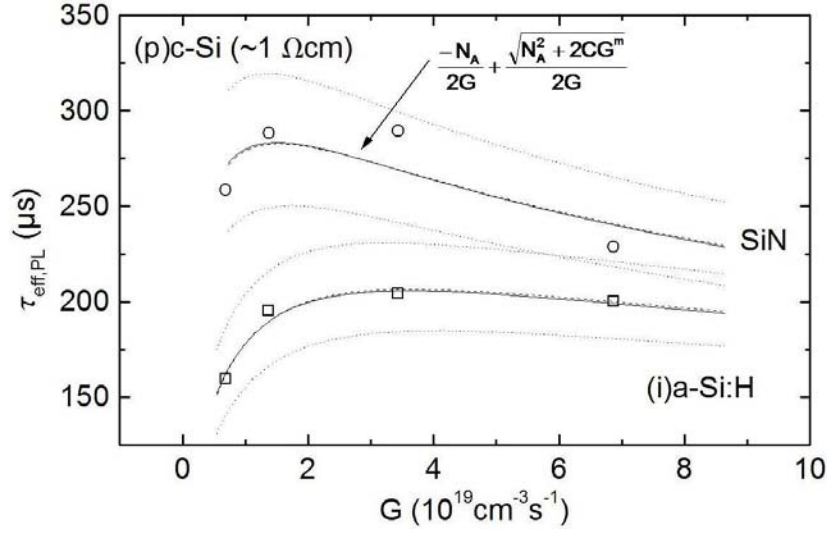


Figure 6.9: Effective lifetime versus generation intensity for the SiN ($m = 1.26$) and one of the (i)a-Si:H ($m = 1.38$) passivated samples obtained from PL measurements at wavelength of maximum emission (open circles and open squares, respectively). The dashed line shows the $\tau_{eff,PL}$ obtained for the extrapolated data from the measured points in Figure 6.5. Dotted curves show the uncertainty derived from the calculation in the splitting of quasi-Fermi levels. The solid lines show the calculations of the effective lifetimes using formula 6.29.

Determination of surface recombination velocity

Assuming that the bulk lifetime is constant versus G , the solution $\Delta n(x)$ of the continuity equation at steady-state conditions (equations (3.18) and (3.19)) has been used for the determination of the surface recombination velocity. As the passivation at both sides of the samples is the same, wafers are symmetrical, and surface recombination velocities at back and front are identical $S_0 = S_d = S$. The absorption coefficient is $\alpha = 1010 \text{ cm}^{-1}$ for the incident wavelength.

From the measurements of PL yield, I derived the total Δn (see equation 6.15) generated via illumination. If the bulk lifetime is known and the surface recombination velocity is varied, the profile of the electron excess carrier densities changes and thus the integral $\int_0^d \Delta n(x) dx$ too. By comparison of experimental and simulated Δn , the value of $S_0 = S_d$ was obtained.

I calculated Δn and $\tau_{eff,PL}$ from experimental luminescence in the previous section. The bulk lifetime of a wafer can only be determined with certain deviations. In our case, the lower limit is given by the very good silicon nitride passivation, where I will consider that the surface recombination velocity is $S_{min} = 0 \text{ cm s}^{-1}$ for the highest $\tau_{eff,PL}$ calculated. In this case the effective lifetime measured equals the bulk lifetime: $\tau_{eff,PL} = \tau_{b,min}$. The calculated maximal effective lifetime (Fig-

ure 6.9) is $320 \mu\text{s}$ at $G = 1.3 \times 10^{19} \text{ cm}^{-3} \text{ s}^{-1}$. Figure 6.10 shows the result of these calculations. The open circles and open squares correspond to the surface recombination velocity obtained from the measurements and the closed circles and squares were obtained from the extrapolated data. The dashed lines show the error corresponding to the inaccuracy in the determination of the splitting of quasi-Fermi levels. For the SiN passivation, the measured point gives values for $S \in (4, 15) \text{ cm s}^{-1}$ and the calculated velocities oscillate between 0 and 20 cm s^{-1} . For the (i)a-Si:H passivation, measured values vary in the range $(21 - 39) \text{ cm s}^{-1}$ and the calculated ones, in the range $(15 - 51) \text{ cm s}^{-1}$.

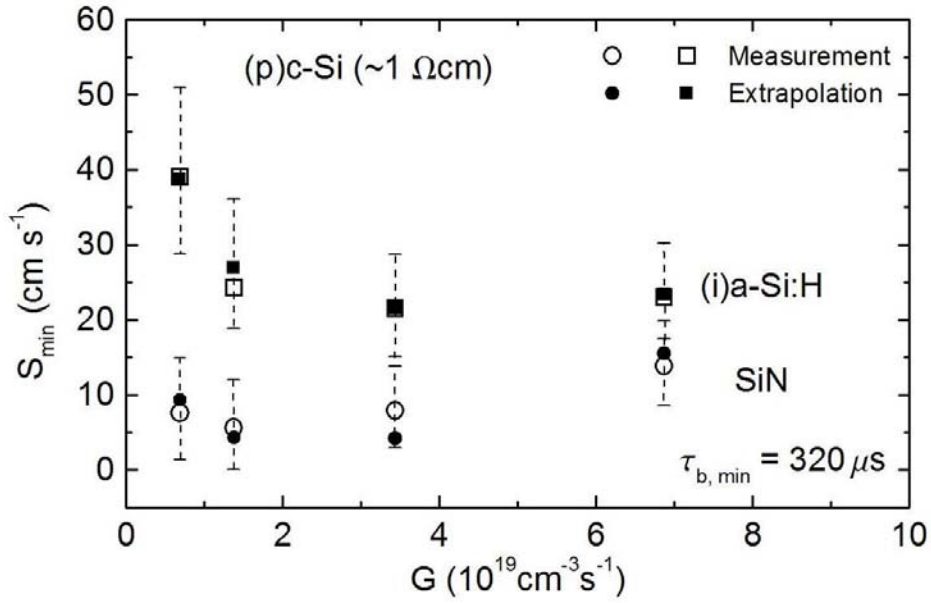


Figure 6.10: Surface recombination velocity versus generation intensity for the SiN (open circles) and a-Si:H passivated (open squares) samples obtained from PL measurements at wavelength of maximum emission and for the extrapolated data (closed symbols). The error bars show the uncertainty derived from the calculation in the splitting of quasi-Fermi levels. For the calculation of S_{\min} , the bulk lifetime assumed is $\tau_{b,\min} = 320 \mu\text{s}$.

As the upper limit, I took the intrinsic bulk lifetime of crystalline silicon, determined by enhanced Auger recombination and radiative recombination [47]: $\tau_{b,\max} = \tau_{b,i}$, where $\tau_{b,i}$ is given by:

$$\frac{1}{\tau_{b,i}} = \frac{1}{\tau_A} + \frac{1}{\tau_{bb}} \quad (6.31)$$

For the determination of the upper limit using (6.31), I used the parametrization developed by Altermatt [48] based in the results from [35] for the enhanced Auger recombination lifetime, so that for the doping concentration of the samples, $N_A = 1.2 \times 10^{16} \text{ cm}^{-3}$, a $\tau_{Ae} \approx 1100 \mu\text{s}$ has been assumed also for a generation

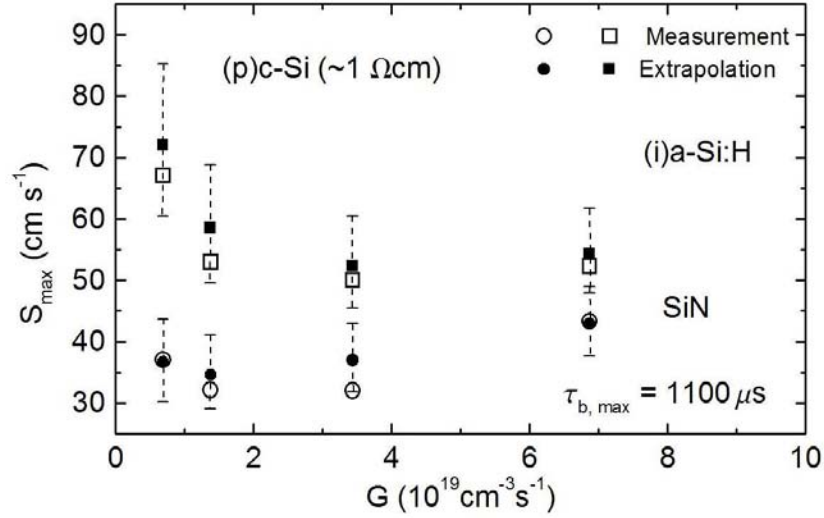


Figure 6.11: Surface recombination velocity versus generation intensity for the SiN (open circles) and one of the (i)a-Si:H (open squares) passivated samples obtained from PL measurements at wavelength of maximum emission for the extrapolated data (closed symbols). Dashed curves show the uncertainty derived from the calculation in the splitting of quasi-Fermi levels. For the calculation of S_{max} it has been considered a bulk lifetime of $\tau_{b,\text{max}} = 1100 \mu\text{s}$ calculated from Auger enhanced recombination.

rate of $G = 1.3 \times 10^{19} \text{ cm}^{-3} \text{ s}^{-1}$. The radiative recombination lifetime is given by $\tau_{bb} = (Bnp)^{-1}$, where $B = 5 \times 10^{-15} \text{ cm}^3 \text{ s}^{-1}$ has been determined experimentally [46]. An intrinsic bulk lifetime of $\tau_{b,i} = \tau_{b,\text{max}} = 1100 \mu\text{s}$ is obtained. Figure 6.11 shows the same calculations as in Figure 6.10 but using the bulk lifetime obtained from enhanced Auger recombination. The surface recombination velocity increases for the same effective lifetimes. For the sample passivated with SiN, S_{max} varies from 32 to 43 cm s^{-1} for the measured points and from 29 to 49 cm s^{-1} for the calculated curves. For the (i)a-Si:H passivation, surface recombination velocity is between 50 and 67 cm s^{-1} for the measured values and between 45 and 85 for the extrapolated data with the inaccuracy included.

In Figure 6.12 the continuity equation at a steady state has been solved for a bulk lifetime of $227 \mu\text{s}$ and different surface recombination velocities from 0 to 200 cm s^{-1} . Considering a minimum value of $S = 5 \dots 10 \text{ cm s}^{-1}$ for the SiN passivation [47], we find that a difference of 30 % (as in the PL) in the excess carrier density is found for S values around 20-30 cm s^{-1} . This confirms the values obtained in the previous calculations, so that it can be that a variation in the surface recombination velocity as described (from around 5 to 20 cm s^{-1}) for the lifetime taken, do produce the measured variation in PL.

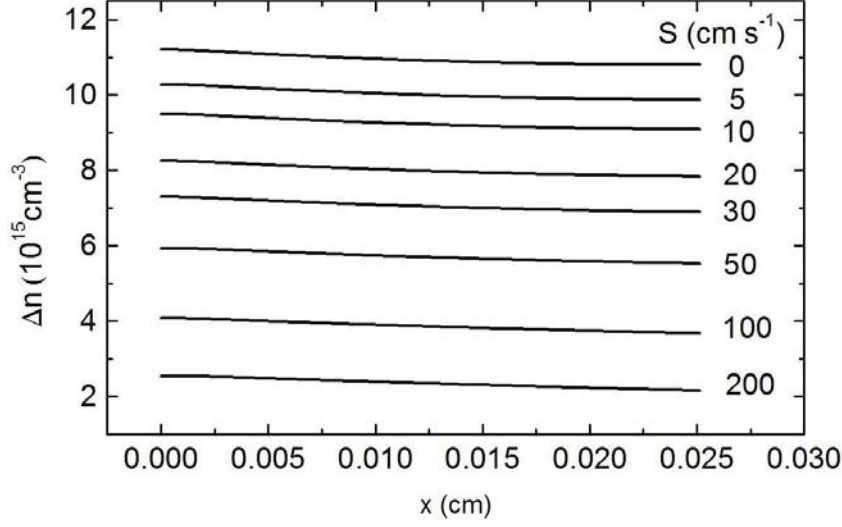


Figure 6.12: Profile of the excess electron density obtained from solving the continuity equation for a fixed volume lifetime ($\tau_b = 227 \mu s$) and various surface recombination velocities S .

6.4 Discussion of results

In this chapter, splitting of quasi-Fermi levels is derived from quantitative photoluminescence. In the calculations it has been considered that the reflection coefficient is constant for all emission wavelengths. This can evolve in differences around the maximum emission wavelength between generated photoluminescence from Planck's Generalized Law curve and the measured spectra. The best fitted curve was obtained for a reflection of 25 % ($n = 3$) for the silicon nitride passivation and 31 % ($n = 3.5$) for the wafers passivated with amorphous silicon.

$E_{F_n} - E_{F_p}$ was calculated for c-Si with different passivation layers. The best quality was obtained with silicon nitride passivation deposited by remote plasma technique, verifying the already investigated good passivation properties of this material [36, 39, 49, 50, 51, 52, 53, 54, 55, 56]. Silicon nitride films may contain a high density of fixed positive charges which induce an inversion layer at the silicon surface producing a field-effect passivation and reducing the surface recombination velocity S . Amorphous silicon can also form very good passivation layers with the advantage of having no parasitic shunting and lower deposition temperatures. In the developed work, (i)a-Si:H passivated wafers show photoluminescence yields very similar to the SiN layers and doped a-Si:H have less splitting of quasi-Fermi levels. Similar results have also been previously reported [57, 26, 55].

Passivation using doped a-Si:H films is noticeable improved when an intrinsic amorphous layer is introduced between them and the silicon substrate [24, 57, 11]. In the samples analyzed, it can also be observed that for the same type of a-Si:H pas-

sivation layer, the HF-dip wafer pretreatment improves the splitting of quasi-Fermi levels in comparison to the RCA process. This result has been extensively proved too [57, 40, 41]. Defects at the interface N_{if} , which increase the surface recombination velocity, can be enormously reduced by means of hydrogen passivation of silicon dangling bonds. Interface defect densities up to $7 \times 10^{11} \text{cm}^{-2} \text{eV}^{-1}$ have been found for wafers precleaned with HF [41].

Once the splitting of quasi-Fermi levels has been determined, the excess electron density and the effective lifetime can be easily calculated for a doped semiconductor under non high injection conditions if the doping density is known. For the SiN passivated sample a value of $\tau_{eff,PL} = 227 \pm 23 \mu\text{s}$ is obtained, the a-Si:H passivated effective lifetimes have values between $(108 \pm 12) \mu\text{s}$ and $2 \mu\text{s}$.

For all the previous calculations a constant distribution of carriers over the wafer under illumination has been assumed. In order to confirm the validity of this simplification, profiles of excess electron density have been simulated using the continuity equation of carriers and splitting of quasi-Fermi levels have been derived from them. For a bulk lifetime of $250 \mu\text{s}$, the variation of Δn from the constant value obtained from the PL measurements can be translated in local variations (in the thickness) of effective lifetime. Variances of up to 5% and 15% have been found for $S < 100 \text{cm s}^{-1}$ and $S \approx 500 \text{cm s}^{-1}$ respectively, which are not very high. Only for $S \approx 8000 \text{cm s}^{-1}$, the variation can get values of 60%.

In order to analyze the effective lifetime when the generation rate is varied, an expression (6.29) relating the effective lifetime and the slope m of the PL was obtained. Under low injection $\tau_{eff,PL}$ follows the behavior of the PL with a slope $m-1$. Between low and high injection conditions, the relation is more complicated, being the solution of a quadratic equation. The excitation intensity considered in this work falls in the latter case and therefore the calculated effective lifetime does not follow the monotone tendency obtained in the PL measurements, but increasing up to $G \approx 3 \times 10^{19} \text{cm}^{-3} \text{s}^{-1}$ and then decreasing progressively (see Figure 6.9).

From the PL measurements non-linearities versus G are clearly observed. Two possible explanations have been investigated in order to explain these non-linearities: intensity dependance of bulk lifetime and of surface recombination velocity.

Bulk lifetime, simulated by a 4-level system, shows variation up to 30 % in the slope of log-log plot of the band-band recombination rate versus G . The critical point in this simulation is the choice of the recombination coefficients. For the capture of holes, increasing β_{iV} , or what is the same, the capture cross section $\sigma_{iV} = \beta_{iV}/v_{th}$, lower slopes are obtained for R_{bb} . Values around 10^{-15}cm^2 are typical values for neutral defects [29, 58, 59]. In the simulation, some of the intrinsic defects are positively charged; therefore, even lower values, accounting for Coulomb repulsive forces, may also be reasonable. In that case, slopes around 1.2-1.3 are ob-

tained (see Figure 6.7). A recombination coefficient of $\beta_{CA} = 10^{-10} \text{cm}^3 \text{s}^{-1}$, which accounts for a capture cross section for electrons of $\sigma_{CA} = 10^{-17} \text{cm}^2$ at the acceptor level was taken. Such a small value is only possible for negative charged atoms in the case of capture of electrons due to repulsive coulomb forces [29]. As nearly all acceptor atoms are ionized, this value is quite reasonable for the studied case. For the same reasons, capture coefficient of holes by the acceptor level should be larger due to attractive coulomb forces. In the simulation a value of $\beta_{AV} = 10^{-9} \text{cm}^3 \text{s}^{-1}$, i.e. $\sigma_{AV} = 10^{-16} \text{cm}^2$ has been assumed. If this value is large enough for that kind of attractive forces or corresponds to neutral recombination centers remains as an open question. Also, a value of $\beta_{Ci} = 10^{-7} \text{cm}^3 \text{s}^{-1}$, which means a $\sigma_{Ci} = 10^{-14} \text{cm}^2$ may be too high for the capture of electrons by neutral defects. Therefore more detailed studies are needed in order to confirm the validity of the capture cross sections taken for the simulation and furthermore, an intensity dependance of the bulk lifetime. That the intensity dependance of PL derives only from bulk lifetime is questioned by the fact that different slopes in the log-log plot of $Y_{pl,max}(G)$ are obtained for different passivated samples (see Figure 6.5), even when the substrate is the same. This suggests that surface recombination is also changed when the sample is illuminated with different excitation intensities.

The calculation of the surface recombination velocity and its intensity dependance have been done by solving the continuity equation for known constant τ_b and comparing the total electron excess densities obtained from PL and from the simulation. The limitation of the possible values for τ_b is done considering a minimum value of $320 \mu\text{s}$ for $S = 0 \text{ cm s}^{-1}$ obtained for the silicon nitride passivation via the effective lifetime calculations and a maximum value of $1100 \mu\text{s}$ given by the intrinsic bulk lifetime. These two quantities seem to be reasonable values for a crystalline silicon wafer with a resistivity of $1 \Omega \text{ cm}$ [19].

S decreases till a minimum around $G = 3 \times 10^{19} \text{cm}^{-3} \text{s}^{-1}$ for the silicon nitride passivation and at $\sim 10^{19} \text{cm}^{-3} \text{s}^{-1}$ for the wafer passivated with (i)a-Si:H when the generation rate is increased, and increases again slowly for both samples. Similar results have been found in previous investigations [50, 51, 55, 27]. These results are in favor of the hypothesis that considers non-linearities in PL due to variations in the recombination rates at the surface when the generation rate is changed. However, the changes in the surface recombination velocities for the SiN passivation in the range of G considered are not confirmed by photoconductive decay (PCD) measurements of similar deposited films [27, 55], which show much smaller variations in S (from 2 to 8 cm s^{-1}).

As none of the two proposed explanations for the non-linearities in the PL describe completely this behavior, the third possible proposal is a combination of both, i.e. that not only the bulk lifetime but also the surface recombination velocities are not constant and vary when changing the excitation intensity. In this case, the calculation τ_b and S is much more complicated.

Finally, it should be mentioned that the definition of the effective lifetime τ_{eff} as $\Delta n/G$ has been derived from its general description from exponential decay of excess carrier densities when the generation is turned off. In that case the recombination rate is assumed to be proportional to Δn : $R = G = \Delta n/\tau$ and not injection dependent. The PL measurements of our samples show an intensity dependance in the form $Y_{PL} \propto G^m$ and then it is questionable if the previous definition is a good approximation. The justification for this extrapolation is the comparison of lifetimes from PL with lifetimes obtained with other measurement techniques which are also defined by the previous equation.

6.5 Comparison of lifetimes from photoluminescence and photoconductive measurements

	$\tau_{eff,PL}(\mu s)$	$\tau_{eff,PCD}(\mu s)$
SiN	227 ± 23	448
(i)a-Si (180nm) HF	108 ± 12	227
(i)a-Si (100nm) RCA	100 ± 12	297
(n)a-Si (180nm) HF	86 ± 10	245
(n)a-Si (40nm) HF	25 ± 4	160
(p)a-Si (100nm) RCA	22 ± 3	13
(n)a-Si (100nm) RCA	2	4

Table 6.3: Excess of electron density and effective lifetime for the different passivated samples. The error given for the PL measurements comes from the inaccuracy in the determination of quasi-Fermi levels.

The effective lifetimes of the SiN and a-Si:H passivated samples were also measured at ISFH via the photoconductive decay technique (PCD) [60]. Results are condensed in Table 6.3 together with the calculated $\tau_{eff,PL}$. The values measured from PL tend to be lower than the measured from PCD. However, the excitation intensity employed is ca. 8 times lower than the one used in the PL experiments, and this can evolve in variances in the effective lifetime. Values of $\tau_{eff,PL}$ calculated from the PL intensity dependence measurements are between 250 and 320 μs for a generation rate $G = 1.5 \times 10^{19} cm^{-3}s^{-1}$ (AM1.5), which is closer to the PCD lifetime value, but still smaller.

Another explanation for the difference between both measurements could be inhomogeneities found in the samples. In Figure 6.13 an effective lifetime scan of the silicon nitride passivated wafer is shown. An illumination around 0.3-0.5 AM1.5 equivalent photon fluxes at a wavelength of 904 nm was used. At the first view

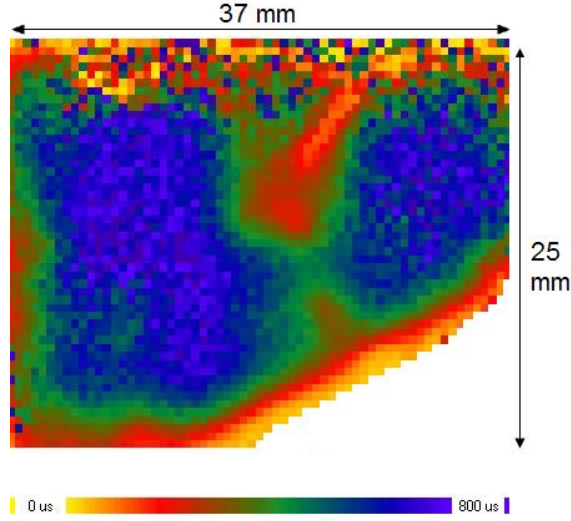


Figure 6.13: Scan of effective lifetime measured by the PCD technique for the SiN passivated sample. Large inhomogeneities can be detected in the wafer [60]. The scala of colors is linear.

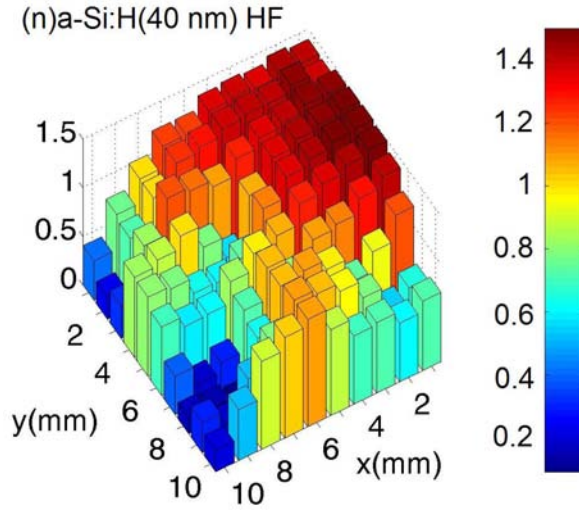


Figure 6.14: PL scan measured from one of the samples passivated with amorphous silicon. Inhomogeneities can be easily detected in the wafer.

it can be observed that in the examined sample large inhomogeneities are detected. Due to this, lateral variations up to 70 % in the lifetime are obtained: $\tau_{eff,PCD} = 448 \pm 211 \mu s$. PL scans at wavelength of maximum emission were also done for the samples passivated with amorphous silicon. One of the scans is shown in Figure 6.14. As for SiN inhomogeneities are easily observable.

Chapter 7

Temperature dependence of photoluminescence

In the following chapter I will discuss the photoluminescence spectra at different temperatures. At low temperatures it is possible to distinguish the indirect transitions in crystalline silicon from transition peaks in PL measurements. Splitting of quasi-Fermi levels and the effective lifetime for a series of temperatures (from 77 K to 393 K) have been derived.

7.1 Indirect transitions in crystalline silicon

In silicon, as the maximum of the valence band and the minimum of the conduction band are not situated at the same k -value, direct transitions between the valence and the conduction band are not allowed for photon energies lower than 3.5 eV due to momentum-conservation. Indirect transitions can only take place if a phonon, with a wave vector which accounts for the difference in momentum between the initial and final states, is absorbed or emitted. The energy and momentum conservation for indirect transitions (with photon absorption) are the following [29]:

Absorption of a phonon:

$$\hbar\omega + \hbar\Omega = E_f - E_i; \quad p = \hbar k_f - \hbar k_i \quad (7.1)$$

Emission of a phonon:

$$\hbar\omega - \hbar\Omega = E_f - E_i; \quad -p = \hbar k_f - \hbar k_i \quad (7.2)$$

where the indices i and f mean the initial and final states of the electron implied in the transition, $\hbar\Omega$ and p are the energy and momentum of a phonon, respectively. The momentum of photons involved is much smaller than p and therefore it can be neglected.

The transition probability P_{ac} for an indirect transition between a state a in the valence band to a state c in the conduction band over an intermediate state b equals the product of two probabilities: 1) direct transition between the state a to the state b , P_{ab}^d , with the absorption of a photon, and 2) emission or absorption of a phonon, P_{bc}^i . For different possible intermediate states, the transition probability is proportional to the sum over all intermediate states [61]:

$$P_{ac} = \sum_b P_{ab}^d P_{bc}^i \quad (7.3)$$

These simple transitions involving a single momentum-conserving phonon described by equations (7.1) and (7.2) could be, in principle, extended to more complex ones where more phonons are included but these kind of multiphonon processes are much less probable.

For each allowed phonon (or set of phonons) and for each emission and absorption of those phonons, a contribution to the absorption constant with identical shape is expected [61]. The identification of each of the corresponding phonon branches can be done via its characteristic transition matrix element (P_{ac}) and its threshold energy, which indicates at which initial energy the transition with the implied phonon is possible. So far, it would be expected to find an absorption spectrum with well defined edges indicating the contribution of particular phonon branches. Experimental results [62] showed these clearly distinguished absorption contributions for low temperatures (~ 5 K). At higher temperatures these structures are smoothed by thermic influences, what is known as relaxation broadening. This smoothing was suggested to be due to exciton scattering by phonon absorption which produces a phonon lifetime broadening or due to deviations from parabolicity [63].

7.2 Detailed analysis of PL-spectra at T=17K

Silicon has a diamond crystal structure, which can be considered as two penetrating face-centered cubic lattices. For the acoustic modes these two sublattices move in the same direction, whereas for the optical mode they move in opposite directions. For a three-dimensional lattice with two atoms per unit cubic cell, as Si, three acoustic modes and three optical modes exist. Longitudinally polarized modes are modes with the displacement vectors of each atom along the direction of the wave vector; thus there is one longitudinal acoustic mode (LA) and one longitudinal optical mode (LO). Modes with atoms moving in the planes normal to the wave vector are called transversely polarized modes. There are two transverse acoustic (TA) and two transverse optical (TO) modes [19].

In this section I am going to analyze the PL spectra at 17 K of one of the samples of the previous Chapter in order to identify the radiative processes involved in the (p)c-Si substrate. At this temperature, the broadening effect is not very strong and

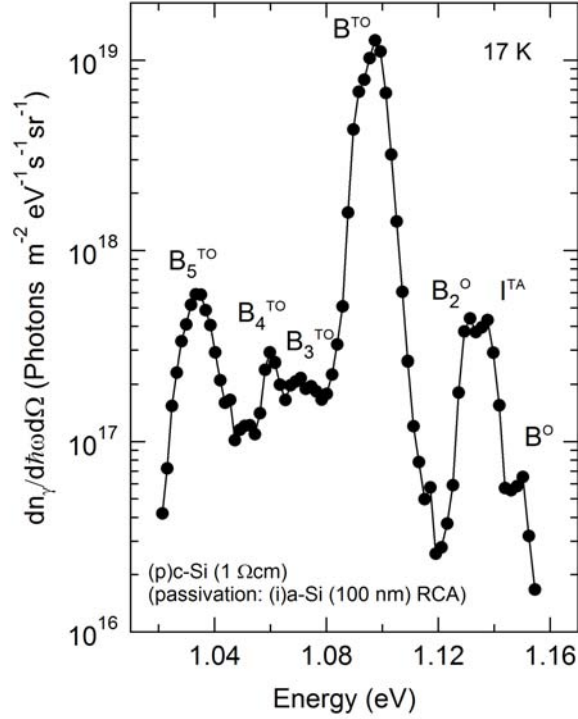


Figure 7.1: Quantitative photoluminescence spectra measured at 17 K from one of the (p)c-Si samples passivated with intrinsic amorphous silicon. Identification of peaks according to [64]

the different transitions can be easily detected. The sample was passivated with amorphous silicon (100 nm) and had an RCA cleaning pretreatment. The sample was placed in a cryostat (Cryo Vac) cooled with liquid helium. Quantitative photoluminescence was measured by comparing the calibrated PL spectra at room temperature with and without cryostat and obtaining a transfer function between both cases.

Figure 7.1 shows the measured photoluminescence and the transition components identified following the notation used by Dean et al. [64]. It can be seen that the spectrum is dominated by the B^{TO} component, which corresponds to transverse optical momentum conserving (MC) phonons. The B^O transition is related to no-phonon assisted decay of excitons bound (BE) to neutral acceptor centers. The second highest components are B_2^O and B_5^{TO} which are phonon replicas of bound exciton transitions, both situated at lower energies than the BE no-phonon line and the TO(MC) phonon replica respectively. According to Dean, the energy differences are related to transverse acoustical momentum conserving (TA(MC)) phonon and multiphonon transitions involving the zone-center optical phonon together with the TO(MC). A process in which a bound electron and hole recombine releasing part of the energy to raise a second hole to an excited bound state is accounted by

the component B_4^{TO} . B_3^{TO} involves recombination of free electrons with one hole in an H^- -like acceptor complex; part of the energy is used to raise a second hole to an excited bound state. Finally, the intrinsic component I^{TA} accounts for the spectral component associated with the recombination of free excitons assisted by transverse phonons.

Table 7.1 compares the lines associated with each of the mentioned transitions in the study developed by Dean and this work. It can be seen that there is a very good accordance between both results.

component	E_P (eV) [64]	E_P (eV) at 17 K
B^0	1.1503	1.151
I^{TA}	1.1365	1.137
B_2^0	1.1319	1.131
B^{TO}	1.0924	1.098
B_3^{TO}	1.067	1.069
B_4^{TO}	1.058	1.059
$I^{TO+0\Gamma}$	1.0315	1.033

Table 7.1: Comparison of the different components of the 17 K PL spectra obtained from own measurements and the ones derived from Dean et al. [64]

7.3 Calculation of the absorption coefficient at different temperatures

Photoluminescence from the sample described in the previous section was further measured at different temperatures: $T = 77, 112, 195, 296, 333, 363$ and 393 K. The same procedure as for the 17 K measurement was used to calibrate the PL-yield.

Figures 7.2 and 7.3 show the obtained curves for temperatures lower than room temperature and higher than room temperature, respectively. It can be observed that for lower temperatures there is a finer structure from the transitions. The higher the temperature is, this fine structure is smoothed, due to the effect of relaxation broadening of excitons mentioned in section 7.1. Another effect that can be noted is that the maximum of the photoluminescence spectrum shifts to lower energies for higher temperatures. The reasons for this effect are changes in bond lengths and electron-phonon interactions which dominate for high temperatures, with the consequence of a reduction of the band gap [65, 66].

In order to obtain the absorption coefficient, the following steps have been applied. Once the experimental curves are calibrated, an analytical photoluminescence spectrum given by the formula:

$$dn_\gamma = A(\hbar\omega) \times \frac{(\hbar\omega)^2}{4\pi^3 c_o^2 \hbar^3} \times \frac{\exp\left(\frac{E_{F_n} - E_{F_p}}{kT}\right) d(\hbar\omega)}{\exp\left(\frac{(\hbar\omega)}{kT}\right)} \quad (7.4)$$

$$A(\hbar\omega) = \frac{[1 - R(\hbar\omega)][1 - \exp(-\alpha(\hbar\omega)d)]}{1 - R(\hbar\omega) \exp(-\alpha(\hbar\omega)d)} \quad (7.5)$$

was calculated in order to estimate the splitting of quasi-Fermi levels. The 1 in the denominator of formula (6.1) was eliminated to simplify the calculations. However, this produces deviations from the real spectrum for energies lower than $\hbar\omega < 1.09\text{eV}$ and $\hbar\omega < 1.05\text{eV}$ at $T = 77\text{ K}$ and 112 K respectively and the fitting was restricted to higher energies than the described for these temperatures. For the calculation of the absorbance, the formula (7.5) was applied. The data for the absorption coefficient $\alpha(\hbar\omega)$ was obtained from literature: [62] and [31] for temperatures $T = 77, 195\text{ K}$ and $T = 112, 296\text{ K}$ respectively, and the reflection coefficient at the interface was $R_i = 0.31$. The excitation intensity has been assumed to be the same for all the temperatures.

T(k)	$E_{F_n} - E_{F_p}$ (eV)
77	1.067
112	1.015
195	0.887
296	0.703
333	0.632
363	0.572
393	0.512

Table 7.2: Splitting of quasi-Fermi levels calculated from the PL curves shown in Figures 7.2 and 7.3.

As no literature data was found for the absorption coefficient at higher temperatures, another method was used to find $E_{F_n} - E_{F_p}$ for the samples in Figure 7.3. For $E > 1.25\text{ eV}$, the absorptivity of silicon is determined only by the reflection coefficient: $A(\hbar\omega) = (1 - R(\hbar\omega))$. Therefore, we only used the high energetic range of the PL spectra to find the splitting of quasi-Fermi levels. In Figures 7.4 and 7.5 one example of each of the used methods is shown. The dashed lines show the analytic curves used for the estimation of $E_{F_n} - E_{F_p}$. The resulting calculated values are shown in Table 7.2. The splitting of quasi-Fermi levels decrease with

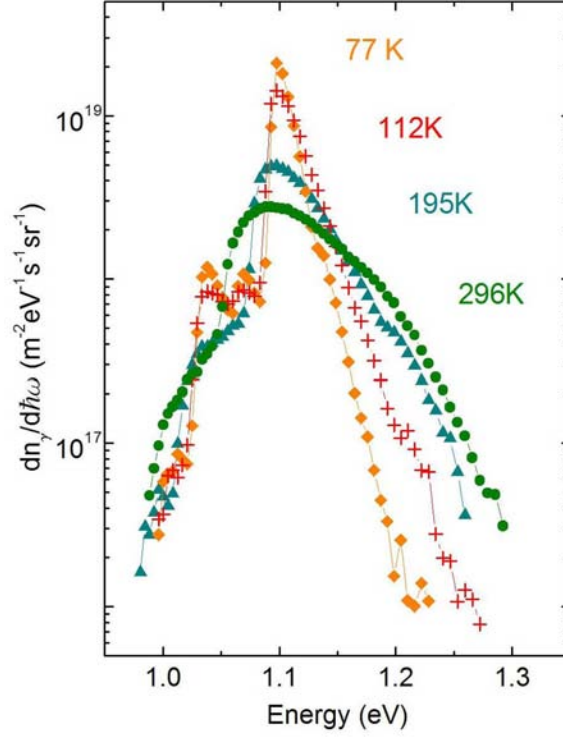


Figure 7.2: Calibrated photoluminescence of p-type crystalline silicon measured at different temperatures ($T \leq 296K$) .

increasing temperature.

Both methods for the calculation of the splitting of quasi-Fermi levels are depicted in Figure 7.6: 1. known the absorptivity and using the analytical expression of photoluminescence (dashed line) and 2. when the $A(\hbar\omega)$ is not known, the absorptivity can be assumed to be $(1 - R(\hbar\omega))$ for $\hbar\omega \geq 1.25eV$, and the fitting is done for high energies. It can be seen how both methods converge at $\hbar\omega \geq 1.25eV$.

The next step is the calculation of the absorbance. With the values of $E_{F_n} - E_{F_p}$ known, $A(\hbar\omega)$ can be easily derived from the measured PL-yield using the following expression derived from Planck's Generalized Law:

$$A(\hbar\omega) = dn_\gamma(\hbar\omega) \frac{4\pi^3 \hbar^3 c_0^2}{(\hbar\omega)^2} \left[\exp \left(\frac{\hbar\omega - (E_{F_n} - E_{F_p})}{kT} \right) - 1 \right] \quad (7.6)$$

The resulting absorbance curves are pictured in Figure 7.7. For getting the values of the absorption coefficient, $\alpha(\hbar\omega)$ was calculated from the absorbance formula used in (6.1):

$$\alpha(\hbar\omega) = \frac{1}{d} \ln \left(\frac{A(\hbar\omega)R_i(\hbar\omega) - 1 + R_i(\hbar\omega)}{A(\hbar\omega) - 1 + R_i(\hbar\omega)} \right) \quad (7.7)$$

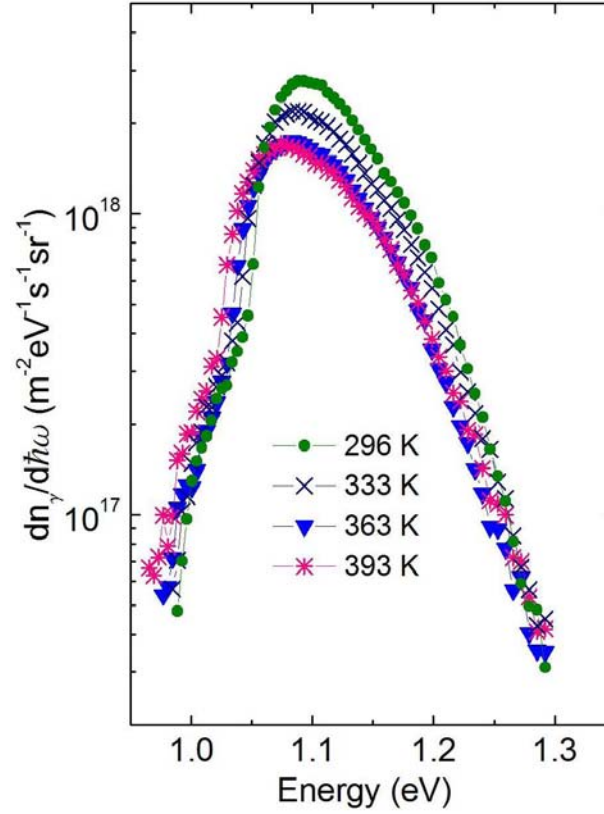


Figure 7.3: Calibrated photoluminescence of p-type crystalline silicon measured at different temperatures ($T \geq 296\text{K}$).

being d the thickness of the wafer and R_i the reflection at the interface. In Figure 7.8 the calculated absorption coefficient and literature data ([62, 31, 67]) are shown for the temperatures $T = 77, 112, 195$ and 296 K . The literature values of α at room temperature is a tabulation from Green and Keevers based in previously measured data. The other data were direct measurements. It can be seen that the obtained values match very well with the literature data for higher energies. For low energies, there is a deviation with the data obtained from MacFarlane et al.. This is probably due to inaccuracy in the digitalization of linear graphical data which was done from the literature data. For the other two temperatures $T = 112\text{ K}$ and $T = 296\text{ K}$, the accordance is found in the whole energy spectrum.

7.4 Effective lifetime at different temperatures

From the measured quantitative photoluminescence for different temperatures, it is possible to obtain the effective lifetime following the same procedure as described in Chapter 6. However, like some material parameters, as the intrinsic carrier density

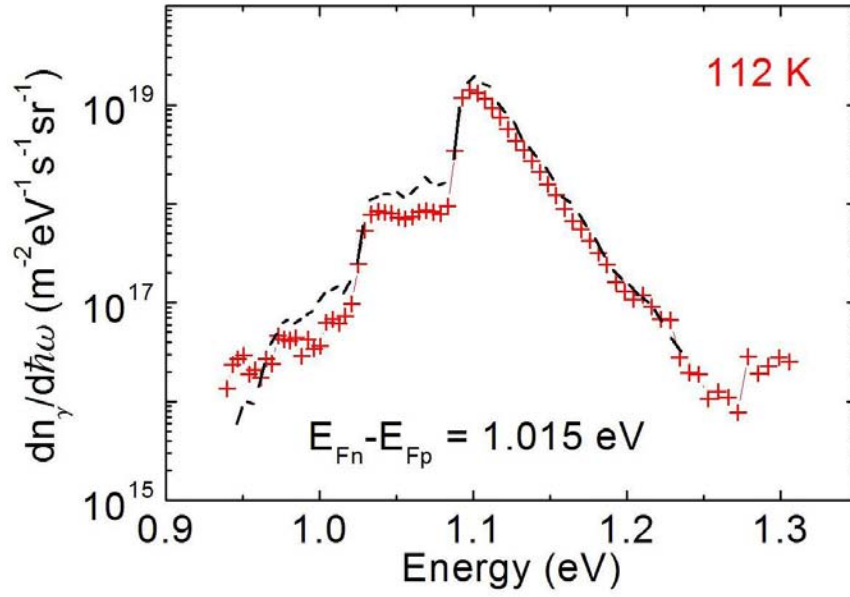


Figure 7.4: Photoluminescence spectra from the (p)c-Si wafer measured at 112 K and analytically calculated PL-yield (dashed line)

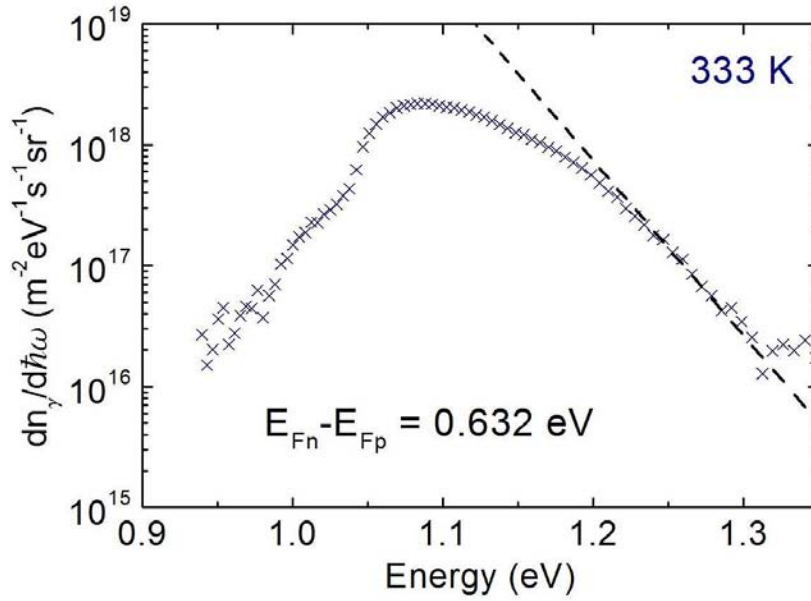


Figure 7.5: Photoluminescence spectra from the (p)c-Si wafer measured at 333 K and analytically calculated PL-yield (dashed line).

and the absorption are temperature dependent, this should be taken into account in the calculations.

For the calculation of the lifetime $\tau_{eff,PL}$ using the formula (6.19) obtained in

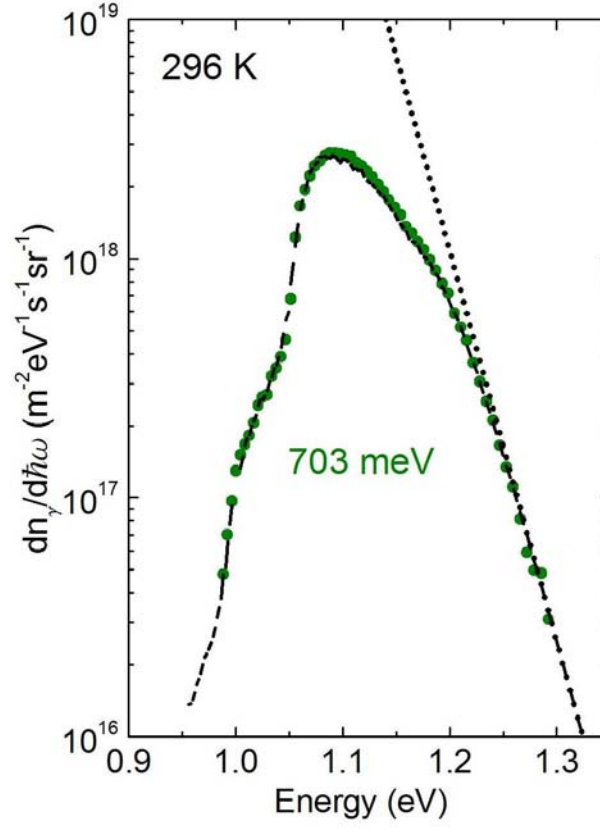


Figure 7.6: Photoluminescence spectra from the (p)c-Si wafer measured at 296 K. Both methods to determine the splitting of quasi-Fermi levels are shown in the graph: 1. known the absorptivity (dashed line) and 2. $A(\hbar\omega) \approx (1 - R(\hbar\omega))$ for $\hbar\omega \geq 1.25\text{eV}$. Both methods converge at $\hbar\omega \geq 1.25\text{eV}$.

Chapter 6,

$$\tau_{eff,PL} = \frac{d \left(-N_A + \sqrt{N_A^2 + 4n_i^2 \left[\exp\left(\frac{E_{Fn} - E_{Fp}}{kT}\right) - 1 \right]} \right)}{2\Phi_i(1 - R)[1 - \exp(\alpha d)]} \quad (7.8)$$

it is necessary to know the density of the doping level N_A and the intrinsic carrier density n_i in addition to the splitting of quasi-Fermi levels, which are temperature dependent.

I have considered $N_{A,0}^- \approx p_0$ and I have solved the particle conservation in the dark in order to know the value of the Fermi level E_F , p_0 and thus N_A :

$$n_0 + N_{A,0}^- = p_0 \quad (7.9)$$

$$N_C \exp\left(-\frac{E_C - E_F}{kT}\right) + N_A \frac{1}{1 + \exp\left(\frac{E_A - E_F}{kT}\right)} = N_V \exp\left(\frac{E_V - E_F}{kT}\right) \quad (7.10)$$

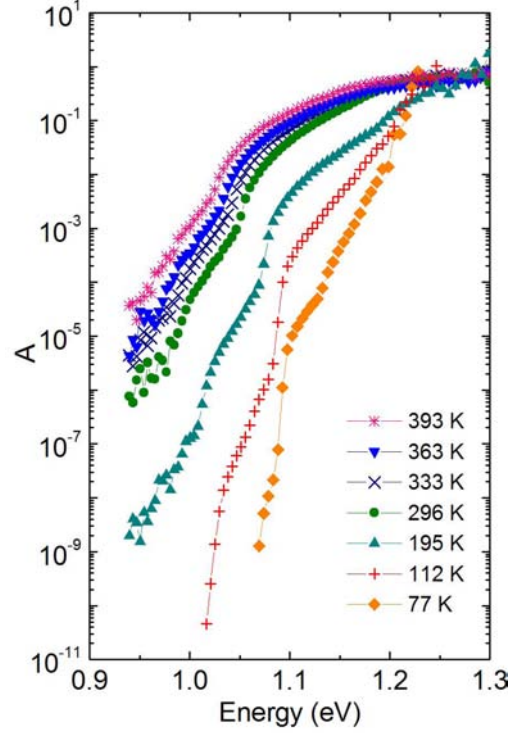


Figure 7.7: Absorbance curves at different temperatures derived from quantitative measurements for a (p)c-Si wafer.

where I have also assumed that the occupation of the doping center N_A is given by Fermi statistics $N_{A,0}^- = 1/(1 + \exp((E_A - E_F)/kT))$, as it is very close to the valence band ($E_A - E_V \approx 0.045\text{eV}$). The variation of the effective density of states N_C and N_V , in the conduction and valence band respectively, the band gap energy E_G and the intrinsic carrier density which are also temperature dependence have been extrapolated from [43].

Using the formula (7.8) the effective lifetime $\tau_{eff,pl}$ was calculated and the results are showed in Figure 7.9. The effective lifetime and thus Δn increase with the temperature. Similar results of lifetime enhancement with increasing temperature have also been reported in the literature [68, 69]. On the contrary, the splitting of quasi-Fermi levels goes up with decreasing T and the measured photoluminescence signal too (see Figure 7.10).

In order to verify the assumptions previously taken, the simulation of the four level recombination system using the Shockley-Read-Hall model as in Chapter 6 has been applied. It has been assumed $N_A = 1.2 \times 10^{16}\text{cm}^{-3}$ and the same values for N_V , N_C and E_G as above to solve 7.10. The result of the variation of the carrier densities with temperature for the generation rate of the experiments ($G = 4 \times 10^{15}\text{cm}^{-3}$) is shown in Figure 7.11. The hypotheses $p_0 = N_A^-$ and $n \approx \Delta n = \Delta p$ are verified

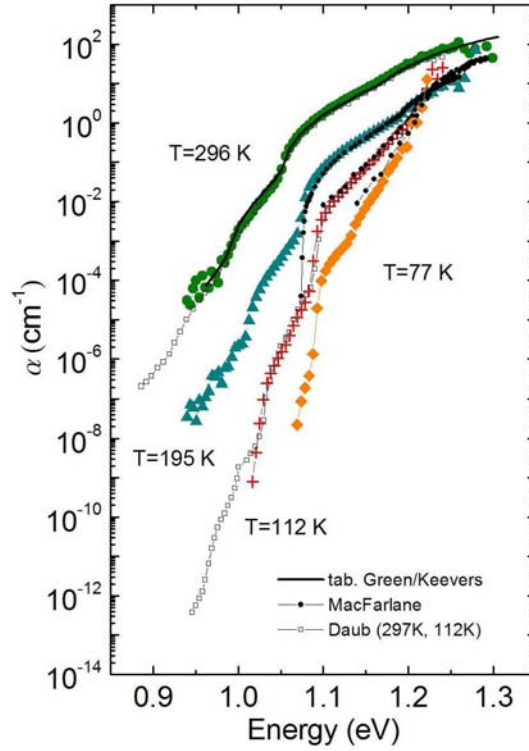


Figure 7.8: Absorption coefficient at different temperatures derived from quantitative PL measurements for a (p)c-Si wafer. Values from literature are also included for comparison: thick solid line from [67], small open squares from [31] and small solid circles from [62].

in the whole range of temperatures considered.

With $\tau_{eff,pl} = \Delta n / G$ and low injection conditions $n \approx \Delta n$, the enhancement of the effective lifetime with the temperature is derived from the increase of excess electron density. The latter is described analytically by $n = \int_{E_C}^{\infty} D_n(E) f_n(E) dE = N_C \exp(-(E_C - E_{F_n})/kT)$. If we assume that the term $E_C - E_{F_n}$ does not change, an increase in the temperature will produce a higher carrier density. That is due to the occupation probability of the electrons $f_n(E) = 1/(1 + \exp((E - E_{F_n})/kT))$, which increase with temperature as electrons have a higher thermal energy and therefore a larger probability to reach the conduction band. Furthermore the density of states $D(E) = 4\pi(2m_n^*/h^2)^{3/2}(E - E_C)^{1/2}$ [29] is incremented also at higher temperatures due to the reduction of the energy gap. These modifications in E_G are due to a change in the shape of the energy-momentum curves with temperature as the lattice expands [43]. As the splitting of quasi-Fermi levels gets smaller with increasing temperature, it would be expected that E_{F_n} moves away from the conduction band and the density of electrons should decrease. As the band gap also decreases and the thermal energy of the electron increases n is enhanced.

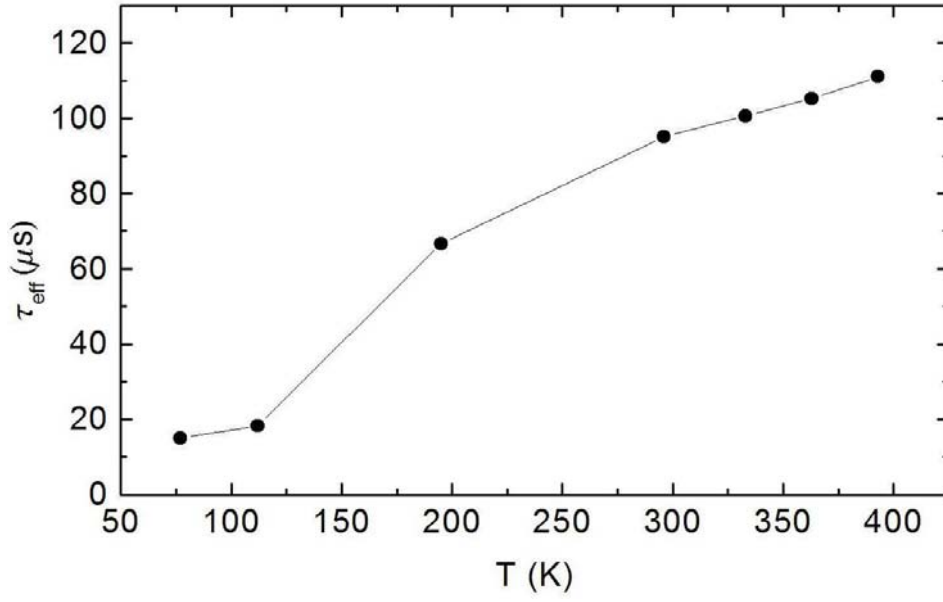


Figure 7.9: Effective lifetimes $\tau_{eff,pl}$ calculated from photoluminescence measurements for different temperatures from 77 K to 393 K. $\tau_{eff,pl}$ clearly increases with temperature.

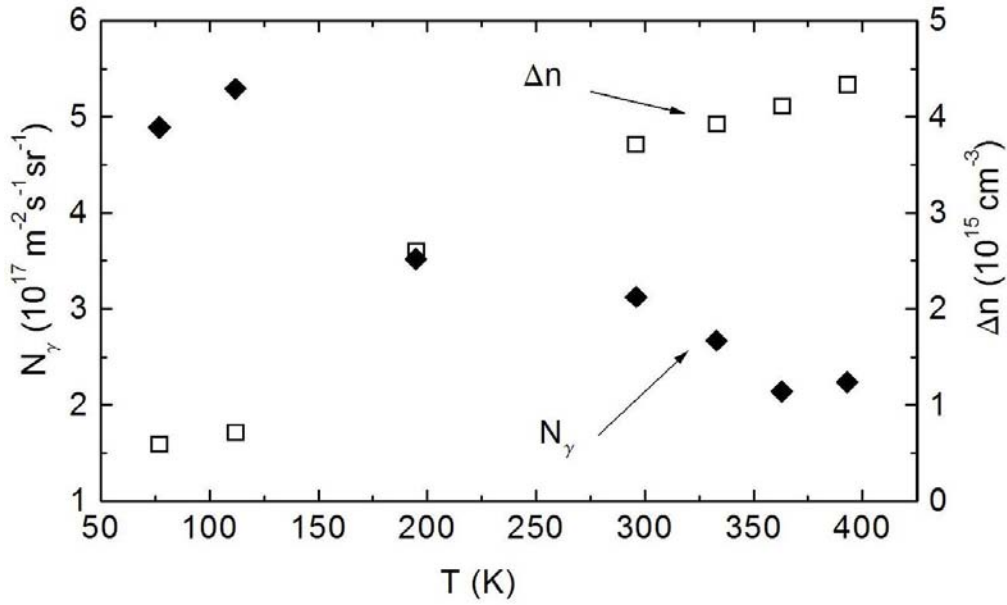


Figure 7.10: Integrated photoluminescence yield and calculated excess carrier densities Δn for different temperatures from 77 K to 393 K. While the photoluminescence decreases Δn increases for higher temperatures.

The emitted photon flux N_γ from an illuminated semiconductor is determined from one side by its absorption and from the other side by the splitting of quasi-Fermi levels. Departing by the formula 6.1 from chapter 6, the 1 in the denominator can

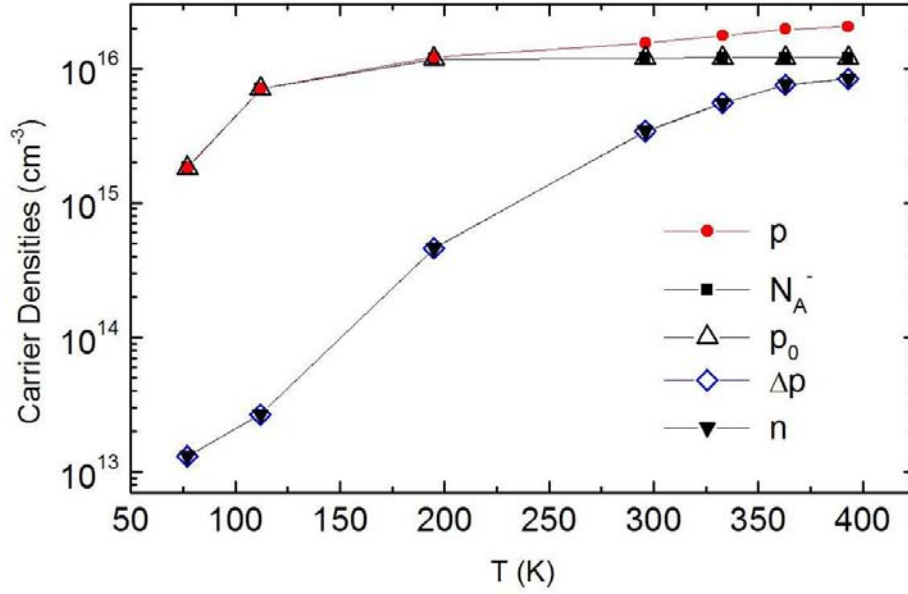


Figure 7.11: Carrier densities obtained from the simulation of a Shockley-Read-Hall recombination model in a 4 level system for different temperatures from 77 K to 393 K and a generation rate of $G = 4 \times 10^{15} \text{ cm}^{-3}$.

be neglected in comparison to the exponential factor for the emission energies of silicon and the splitting of quasi-Fermi levels obtained for a temperature higher than 112 K. For $T = 77$ and 112 K, the assumption is incorrect for energies lower than $\hbar\omega = 1.09$ and 1.05 eV respectively, so that the integral is overestimated. Due to the inaccuracy in the determination of the splitting of quasi-Fermi levels, a detailed analysis for these low temperatures is not necessary. Integrating N_γ over the whole spectrum:

$$N_\gamma = \int_0^\infty \frac{A(\hbar\omega)(\hbar\omega)^2}{4\pi^3 c_o^2 \hbar^3} \exp\left(\frac{-\hbar\omega + (E_{F_n} - E_{F_p})}{kT}\right) d(\hbar\omega) \quad (7.11)$$

In this expression, the factor which is diminishing when the temperature increases is the exponential term $\exp((\hbar\omega + (E_{F_n} - E_{F_p}))/kT)$ due to the decrease in the splitting of quasi-Fermi energies. Calculating the derivative of $E_{F_n} - E_{F_p} = kT \ln(np/n_i^2)$ one gets:

$$\frac{d(E_{F_n} - E_{F_p})}{dT} = \frac{(E_{F_n} - E_{F_p}) - E_G}{T} + kT \left(\frac{1}{n} \frac{dn}{dT} + \frac{1}{p} \frac{dp}{dT} \right) \quad (7.12)$$

$$\approx \frac{(E_{F_n} - E_{F_p}) - E_G}{T} + kT \frac{1}{n} \frac{dn}{dT} \quad (7.13)$$

where the term $1/p(dp/dT)$ has been neglected because for an p-doped semiconductor the hole density does not change noticeably with temperature. The factor $1/n(dn/dT)$ can also be ignored in comparison to the first term of the sum as it is

much smaller in our case. Therefore, it can be affirmed that the temperature dependence of the splitting of the quasi-Fermi levels is caused by $((E_{F_n} - E_{F_p}) - E_G)/T$.

The photoluminescence yield can also be expressed as a function of the product of the carrier densities:

$$\begin{aligned} N_\gamma &= \int_{-\infty}^{\infty} \frac{A(\hbar\omega)(\hbar\omega)^2}{n_i^2 4\pi^3 c_o^2 \hbar^3} \exp\left(-\frac{\hbar\omega}{kT}\right) d(\hbar\omega) \times np \\ &= X(T)np \end{aligned} \quad (7.14)$$

being:

$$X(T) = \int_{-\infty}^{\infty} \frac{A(\hbar\omega)(\hbar\omega)^2}{n_i^2 4\pi^3 c_o^2 \hbar^3} \exp\left(-\frac{\hbar\omega}{kT}\right) d(\hbar\omega) \quad (7.15)$$

a factor which depends on the material properties as absorbance $A(\hbar\omega)$ and intrinsic carrier density n_i and on the geometry of the sample. $X(T)$ is temperature dependent through $A(\hbar\omega)$ and n_i . This factor has units of cm^4s^{-1} and it can be interpreted as a recombination coefficient per volume.

In order to understand the tendency of the photoluminescence yield when varying the temperature I have depicted $X(T)$ and np versus temperature in Figure 7.12. The product np was calculated from the splitting of quasi-Fermi levels obtained in the previous section and increase with the temperature. The factor $X(T)$, on the contrary decreases noticeably, and it was calculated taking the $A(\hbar\omega)$ obtained from PL measurements and n_i by extrapolating data from reference [43]. So far, the diminution of the photoluminescence yield results from the factor $X(T)$. Analytically, all the terms $A(\hbar\omega)$, n_i and $\exp(-\hbar\omega/kT)$ enhance when T increases. As the intrinsic carrier density is placed in the denominator of $X(T)$, it forces the whole factor to diminish. Physically, it has been suggested [70] that the decrease of the coefficient of radiative recombination with T is due to Coulomb interaction between electron and holes, so that they attract each other. Therefore there is a higher density of electrons in the vicinity of a hole. In order to account for this Coulomb enhancement a correlation factor g_{eh} should be included in the recombination coefficient, where g_{eh} increases with decreasing temperature. Talking in terms of capture cross sections, this would imply that the latter should increase for higher temperatures.

Finally, It should be noted that lifetime measurements can not always be a good reference to evaluate the photovoltaic function of a material. In this section we have seen how PL and the splitting of quasi-Fermi levels, and therefore the open circuit voltage diminish with increasing temperature, as it is expected in a solar cell. The effective lifetime, on the contrary, is enhanced.

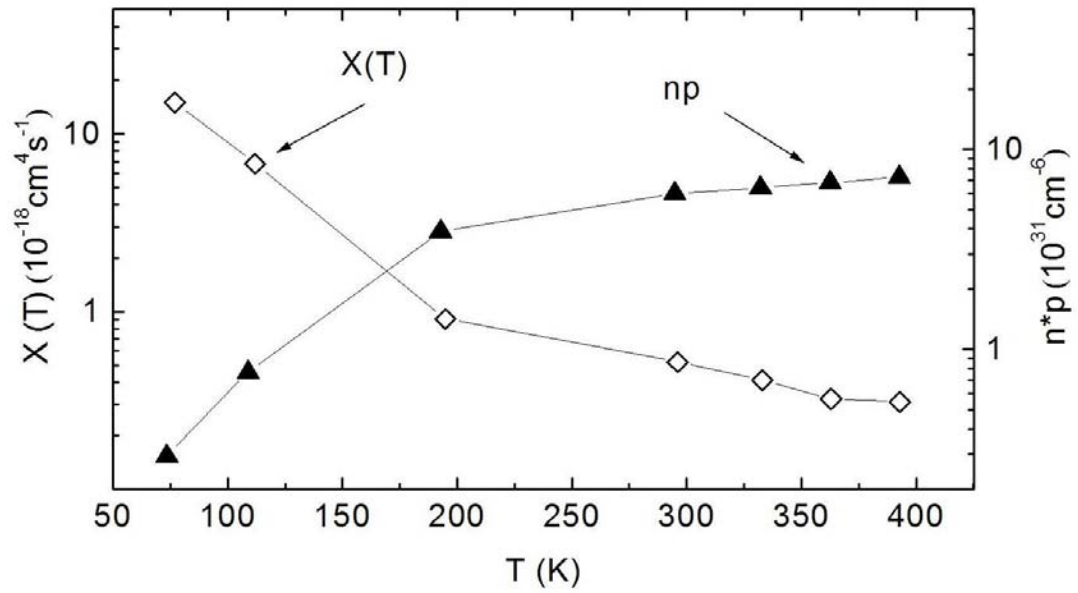


Figure 7.12: Factor $X(T)$ and the product of electron and hole densities np versus T . $X(T)$ decreases while np increase for higher temperatures

Chapter 8

a-Si:H/c-Si solar cell processing: step by step via PL

In this chapter I analyze the different steps followed in a standard deposition of a-Si:H/c-Si solar cells. Via absolute photoluminescence the splitting of quasi-Fermi energies in the bulk can be evaluated and therefore it can be estimated if the structure is improved or degraded. In contrast to other experimental measurement techniques, photoluminescence has the advantage of being a contact-less analysis method. Therefore it is not needed to complete the whole structure of the solar cell to analyze it. The study of each of the consecutive structures that are made by processing a-Si:H/c-Si heterojunctions helps to isolate and evaluate different parameters which play a crucial role in the improvement of the technology and understanding the physics underlying the performance of the solar cells, such as cleaning pretreatment, i.e. passivation of defects at the interface, or deposition of amorphous silicon, which changes the band bending of the heterostructure and therefore decrease or improve recombination at the a-Si:H/c-Si interface.

After the experimental determination of the splitting of quasi-Fermi levels, computer simulation using the program SC-Simul [18] has been done in order to obtain the same $E_{F_n} - E_{F_p}$ values as from the PL measurements, getting access to internal variables of the heterojunction like density and energetic position of interface defects. These calculations have been developed using typical physical parameters for crystalline and amorphous silicon under the assumption of a reasonable structural model for interface defects in the a-Si:H/c-Si heterostructure.

8.1 Sample description

The samples were prepared at the Institut für Physikalische Elektronik in Stuttgart. The substrate used was the same as the one studied in the previous chapters, that means, a p-typed doped silicon wafer, 250 μm thick and a specific resistivity of 0.8-1 $\Omega\text{ cm}$. The steps processing the solar cell include:

a-Si:H				a-Si:H		
TCO	(n)	(i)	(p)c-Si	(i)	(p)	Al
85 nm	8 nm	8 nm	250 μm	8 nm	20 nm	1.5 μm

Figure 8.1: Structure (geometry and electronic design) of the samples analyzed. A FZ p-type wafer with a 0.8-1 Ω cm resistance and 250 μm thickness was used for all samples.

1. a) Cleaning of samples: ultrasonic Aceton(10')/ Iso-Propanol (10') b) Remove SiO₂: HF-Dip 5% (10'') c) Defect passivation: (i)a-Si deposition (6-8 nm) at both sides of the wafer
2. Deposition of (n)a-Si (6-8 nm) at front side in order to form a pn-junction
3. (p)a-Si (20nm) deposition at the back side as back surface field to avoid recombination in the contact
4. Deposition of (i)ZnO (5nm)/ ZnO:Al (80nm) at the front side as conductive transparent layer
5. Evaporation of aluminum back contact (1.5 μm)
6. Front contact fingers: Ag (800 nm)/ Al (200 nm)

Figure 8.1 shows the complete cell with the different layers that were deposited consecutively on the same silicon wafer. After each of the above steps a piece of the wafer was cut for experiments and processing was continued with the remaining piece of the wafer. In our series, after the deposition of the (i)a-Si:H layer (process step 1), (n)a-Si:H was also deposited on both sides of the wafer (process step 2). With such a symmetrical structure the analytical evaluation of photoluminescence results becomes easier.

8.2 Experimental results and simulation

Splitting of quasi-Fermi levels was calculated from photoluminescence measurements at each of the described samples. These were excited with 1.6×10^{18} photons $\text{cm}^{-2} \text{s}^{-1}$ ($\sim 4 \times AM1.5$) by a laser diode with a wavelength $\lambda = 782 \text{nm}$. Figure 8.2 shows the measured photoluminescence curves of the whole series in absolute units. For the calculation of the splitting of quasi-Fermi levels, the same procedure as in Chapter 6 was used for the symmetric structures. For the non-symmetric

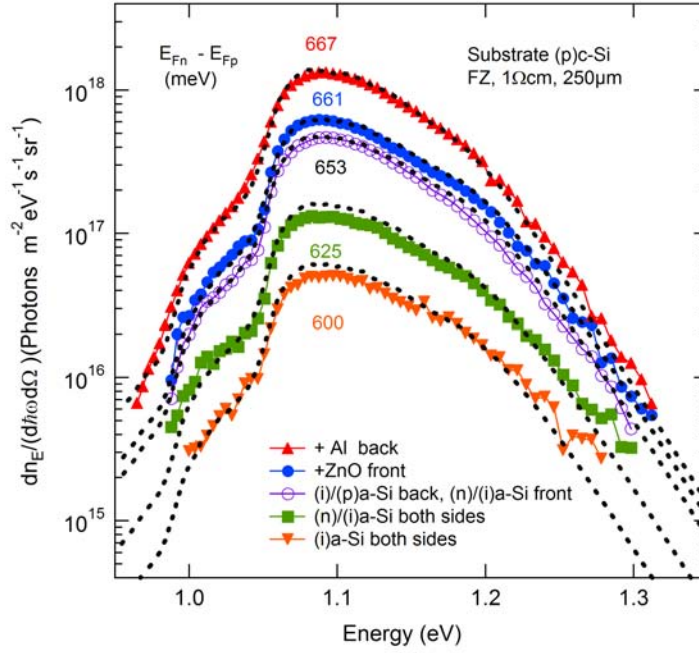


Figure 8.2: Calibrated photoluminescence after each step of a-Si:H/c-Si solar cell processing and calculated splitting of quasi-Fermi levels. $E_{Fn} - E_{Fp}$ were obtained by fitting the spectrum to the analytical calculated curves (dashed line).

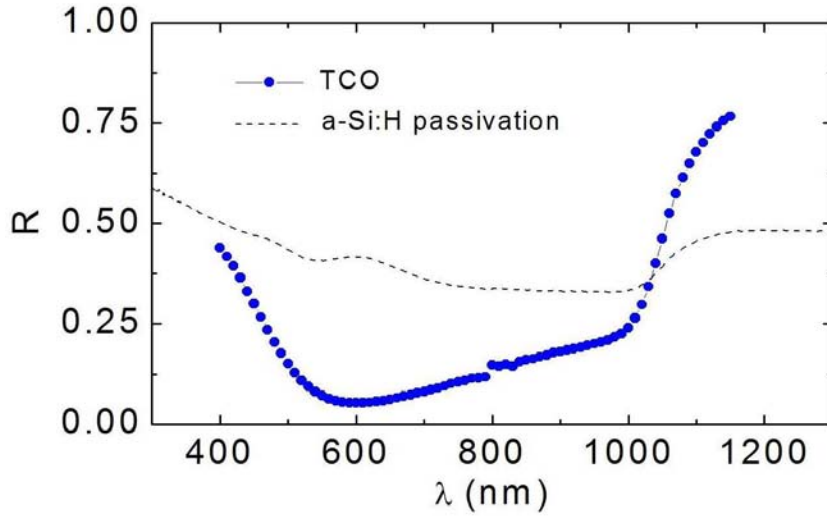


Figure 8.3: Reflection coefficient for the studied (p)c-Si substrate with a-Si:H passivation and after deposition of TCO. R is reduced for shorter wavelengths due to the TCO layer.

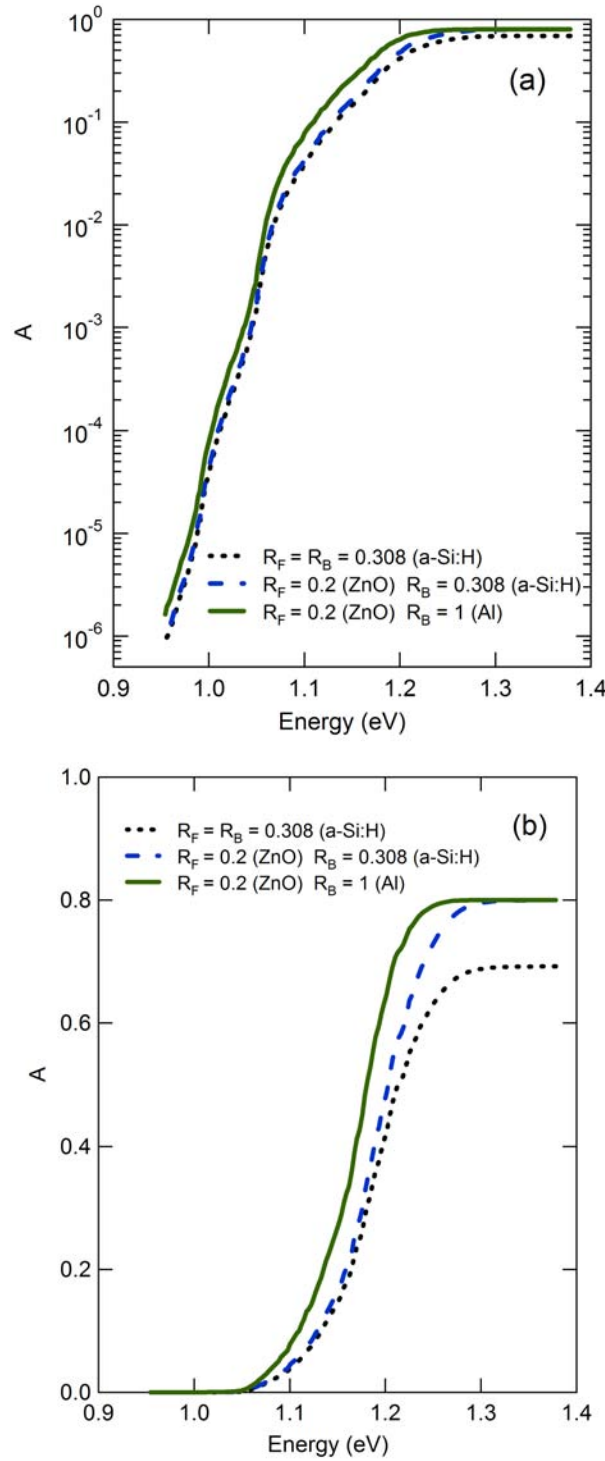


Figure 8.4: Calculated absorbance of the (p)a-Si wafer examined for different reflection coefficients at the front and back in logarithmic (a) and linear (b) scale. For the symmetric samples the same reflectivity at the front and back of the wafer has been assumed ($R_F = R_B = 0.308$), the addition of a ZnO layer reduces the reflection at the front ($R_F = 0.2$) which results in an increase of A at high energies. The addition of a back contact produces a reflector ($R_B = 1$) and A increases for energies ($\hbar\omega$) < 1.25 eV.

structures, the absorbance has been calculated assuming a different reflection at the back and front of the wafer. Solving the formula (3.15) for constant splitting of quasi-Fermi levels, $A(\hbar\omega)$ is given by:

$$A(\hbar\omega) = \frac{(1 - R_f(\hbar\omega))(1 + R_B(\hbar\omega) \exp(-\alpha(\hbar\omega)d))(1 - \exp(-\alpha(\hbar\omega)d))}{1 - R_F(\hbar\omega)R_B(\hbar\omega) \exp(-2\alpha(\hbar\omega)d)} \quad (8.1)$$

Figure 8.2 also shows the curves generated from the Planck's Generalized Law (dashed) which fit the PL spectrum used for the derivation of the quasi-Fermi levels in logarithmic. For the samples from the process step 1 to 3 with the thin amorphous layer only, identical reflection coefficients $R_F = R_B \approx 0.3$ were taken for the evaluation. $E_{F_n} - E_{F_p}$ increases after each processing step, starting from 600 ± 4 meV for the wafer with symmetrical (i)a-Si:H passivation till 653 ± 4 meV with (p)a-Si:H back layer.

For the samples obtained after step 4 and 5 the PL yield increases further. The results for $E_{F_n} - E_{F_p}$ are influenced by the reflection properties which change the absorbance. Figure 8.3 shows the reflection of the silicon wafer passivated with an amorphous silicon layer and of the sample corresponding to the 4th step, i.e., after the deposition of the TCO layer. The reflection is strongly reduced by the TCO, from around 0.33 for the a-Si:H passivation to a range between 0.1 and 0.25. This causes a higher coupling of photons into the wafer. The increment in the reflection for large wavelengths is due to the reflection at the back side of the wafer.

Figures 8.4 (a) and (b) show the calculated absorbance ($A(\hbar\omega)$) from quantitative photoluminescence measurements as explained in Chapter 6, in logarithmic and linear scale respectively. It can be seen that changes in the reflection due to the ZnO and aluminum layers in our series varies the absorptivity of the wafer. The dashed line corresponds to the addition of ZnO, i.e., increase of the photons coupled into the (p)c-Si. The addition of an aluminum layer which acts as a mirror (reflectivity $R_B = 1$) does not have any effect at high energies but increases A for $\hbar\omega < 1.3$ eV. This nominally enhances the photoluminescence output even if the splitting of quasi-Fermi levels would be unchanged.

$R \approx 0.1$ for the ZnO layer (see Figure 8.3) at wavelength $\lambda = 782$ nm. In comparison to the reflection without ZnO ($R \approx 0.3$), a gain of approximately 22% is obtained. Translating this increment into a hypothetic increase in splitting of quasi-Fermi levels assuming that each absorbed photon generates one electron-hole pair, yields:

$$\Delta(E_{F_n} - E_{F_p}) = kT \ln \left(\frac{\Phi_{\gamma, ZnO}}{\Phi_{\gamma}} \right) = kT \ln \left(\frac{0.9\Phi_i}{0.7\Phi_i} \right) = 7meV \quad (8.2)$$

where $\Phi_{\gamma, ZnO}$, Φ_{γ} are the photon fluxes absorbed by the silicon substrate with the ZnO layer and without the layer, respectively, and Φ_i is the photon flux incident

into the wafer.

For the calculation of $E_{F_n} - E_{F_p}$ when the ZnO layer is deposited on the wafer, a higher transmission from the wafer in the direction of the detector has been assumed, due to the lower reflection of the conductive layer. A value of $R_F = 0.2$ was taken for the calculation of the absorptivity given by equation (8.1) and shown in Figure 8.4. In the experimental results in Figure 8.2 we find a difference of 8 meV between the structure with the ZnO and without it. Recalculating the absorbance for the sample with the Al back contact (see Figure 8.4), the splitting of quasi-Fermi levels increases by 6 meV.

Recombination at the interface influences strongly the splitting of quasi-Fermi levels in terms of excess carrier concentration in the volume and due to this, a correct representation of interface defects is needed. It has been assumed that there is a very good surface passivation of defects via HF-dip etching and an introduction of defects by the deposition of a-Si:H so that defects at the interface may have the same structural behavior as dangling bonds in the amorphous layer. Therefore the distribution taken for the defects at the interface was a Gaussian profile. These induced defects have amphoteric character, i.e., they could be positively, or negatively charged. Band tails were not included in the interface defect layer. In the simulation, the a-Si:H/c-Si interface was considered as a 2 nm interface layer with a defect density which is interpreted as an interface defect density (N_{if}). The Gaussian energetic distribution of the defects is described by:

$$N_{if}(E) = \frac{N_{if}}{\sigma\sqrt{2\pi}} \exp \left[-\frac{1}{2} \left(\frac{E - E_P}{\sigma} \right)^2 \right] \quad (8.3)$$

where E_P is the peak energy and σ is the width of the distribution. Thus, parameters that describe the interface defect distribution are the correlation energy $U_{corr} = 0.25$ eV (see Appendix B), similar to the a-Si:H structure, σ and E_P , both of them were varied in the simulation.

In order to evaluate qualitatively recombination rates at the interface, a defect distribution width of $\sigma = 0.2$ eV and the following capture coefficient values, within values found in literature [19, 71]: $c_n^{D+} = 10^{-7} \text{ cm}^3\text{s}^{-1}$, $c_n^{D0} = 10^{-8} \text{ cm}^3\text{s}^{-1}$, $c_p^{D-} = 10^{-7} \text{ cm}^3\text{s}^{-1}$ and $c_p^{D0} = 10^{-8} \text{ cm}^3\text{s}^{-1}$, were used.

The first problem that needed to be solved was finding the energetic position of the defects at the interface. In order to get an answer to this problem, the first two analyzed samples (passivation of c-Si with (i)a-Si:H and addition of (n)a-Si:H to both sides of the wafer) had to be simulated. The energy position of the interface defect distribution was shifted along the bandgap from $E_P - E_V = 0.2$ to 0.9 eV. Good agreement between simulation and experiment for the symmetrical (i)a-Si:H/(p)c-Si/(i)a-Si:H structure was found for a defect density of $3.2 \times 10^{18} \text{ cm}^{-3}$, which can be interpreted in a superficial defect density, N_{if} , of 6.4×10^{11}

cm^{-2} . Similar values were found via dynamic surface photovoltage measurements for wafers precleaned with HF-dip prior to a-Si:H deposition [41].

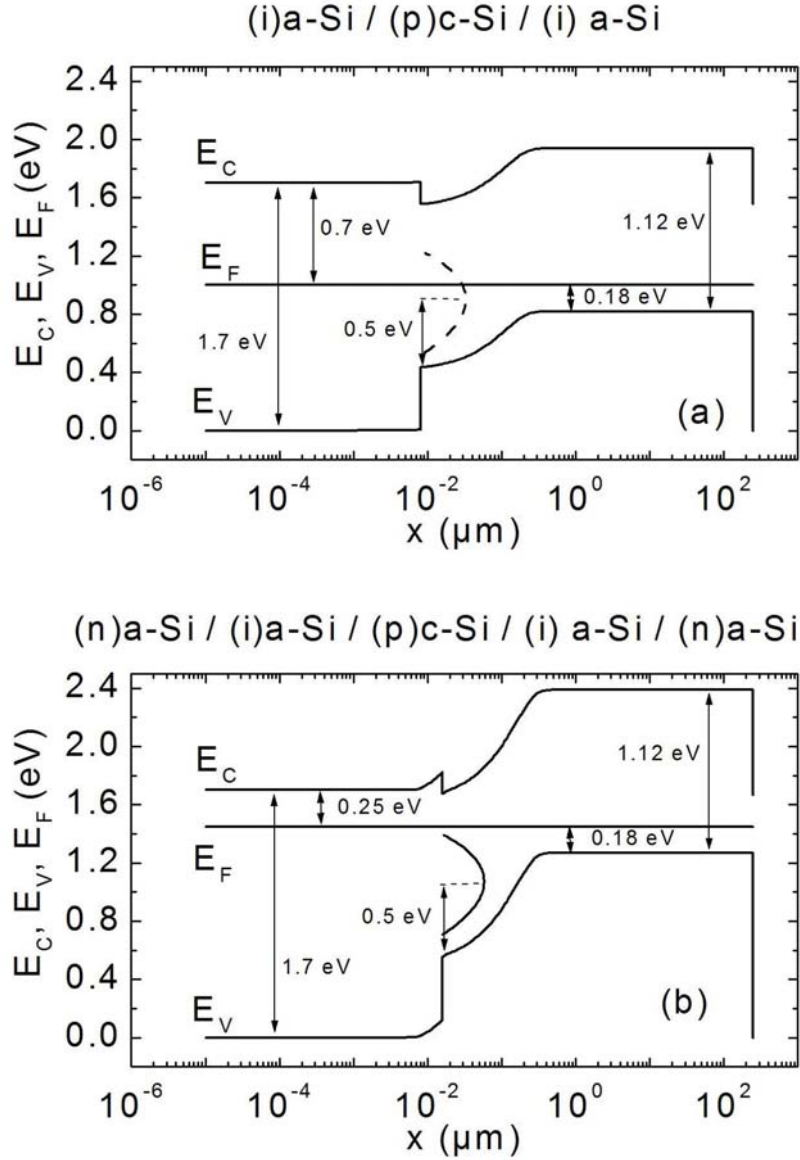


Figure 8.5: Band diagram in thermodynamic equilibrium of a p-type wafer both sides passivated with (a) (i)a-Si:H and (b) (n)a-Si:H/(i)a-Si:H. In the diagram the energetic distribution of defects at the interface is schematically shown.

Band diagrams in thermodynamic equilibrium of both passivation structures are outlined in Figures 8.5(a) and (b). The band bending of (n)a-Si:H/(i)a-Si:H passivation is stronger than for the passivation with (i)a-Si:H. As the minority carrier density is given by $n = N_C \exp(-(E_C - E_{F_n})/kT)$, there is an increase in the

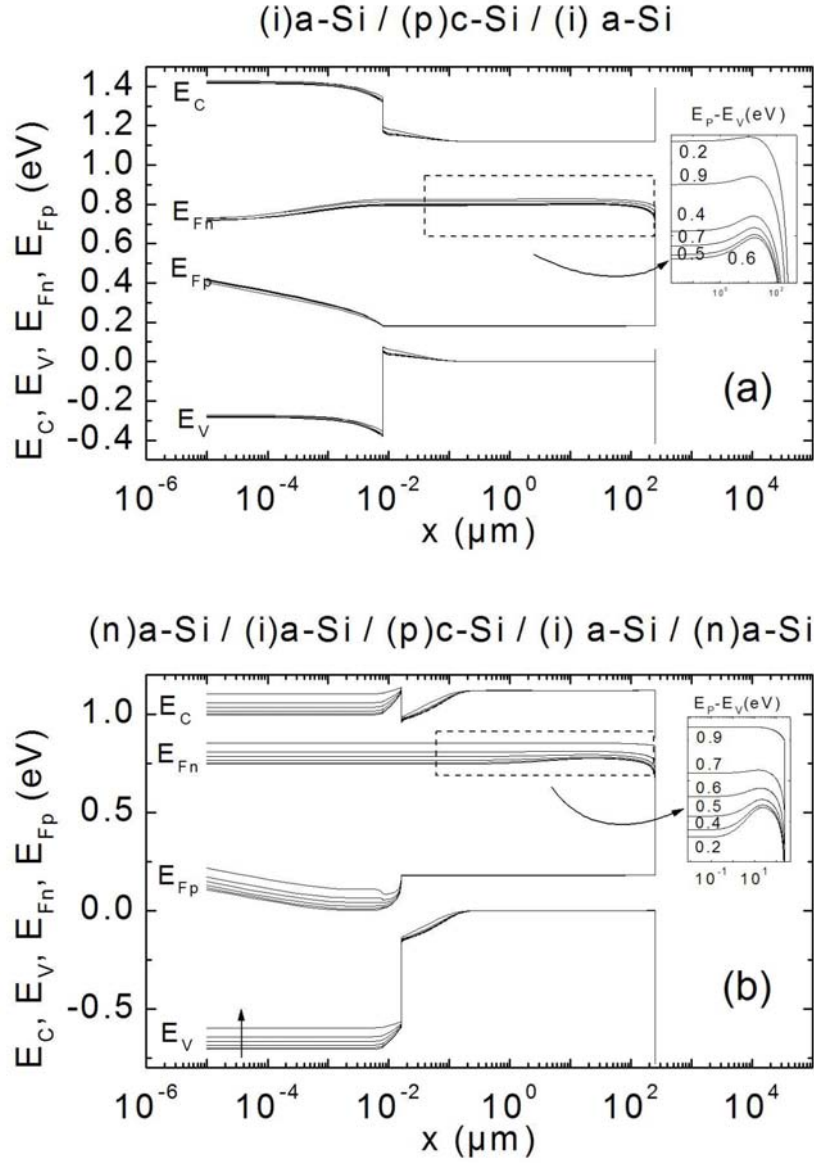


Figure 8.6: Calculated band diagram under illumination ($\phi = 1.6 \times 10^{18} \text{cm}^{-2} \text{s}^{-1}$ and $\lambda = 782 \text{ nm}$) of a p-type wafer both sides passivated with (a) (i)a-Si:H and (b) (n)a-Si:H/(i)a-Si:H. On the upper right corner the change of the quasi-Fermi levels for the electrons for different interface defect energetic positions is shown ($T = 300 \text{ K}$).

dn/dx , so that the diffusion current is increased at the interface and thus also recombination. Due to this, it should be expected intuitively to get less splitting of quasi-Fermi levels when an (n)a-Si:H layer is added to the initial passivation with (i)a-Si:H. This first vision about recombination in the heterostructures cannot be easily extended when they are illuminated because band bending changes

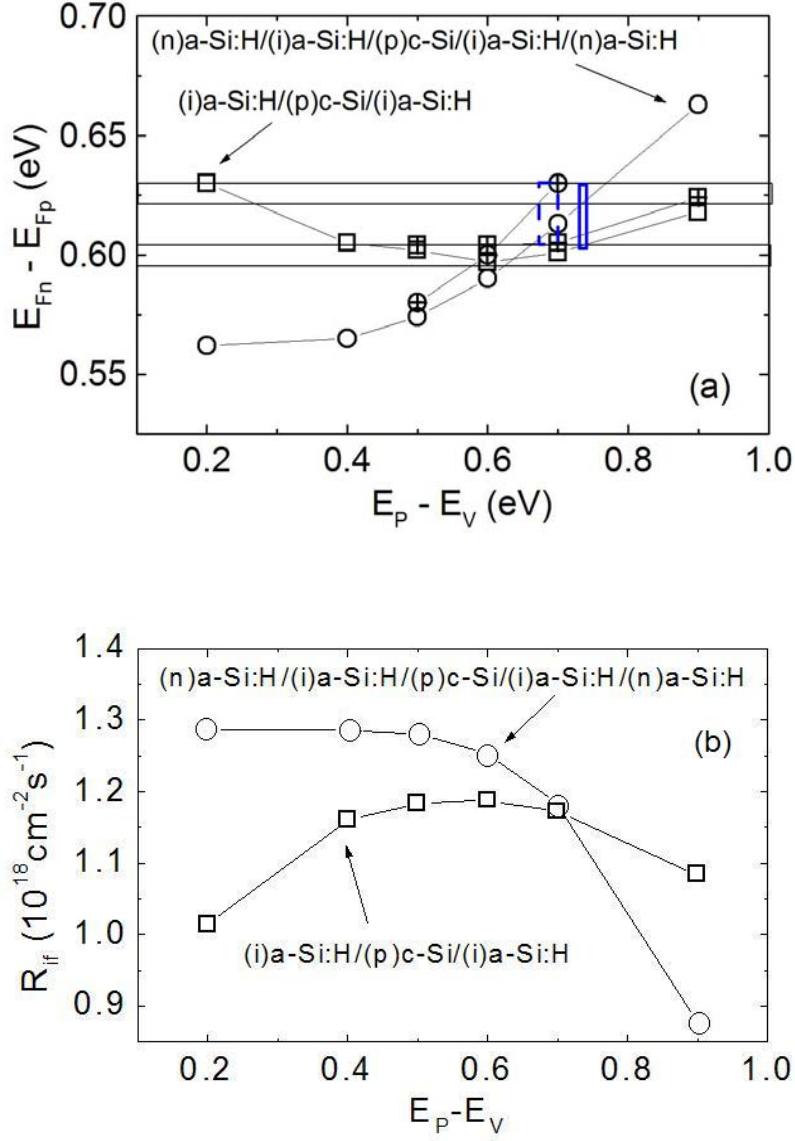


Figure 8.7: (a) Splitting of quasi-Fermi levels for different energetic positions of the peaks defect distribution at the interface for (i)a-Si:H and (n)a-Si:H/(i)a-Si:H passivated wafers. The simulation was done for two different parameter inputs: $\sigma = 0.2$ eV (open squares and circles) and $\sigma = 0.1$ eV (crossed squares and circles). The capture and coefficients were also different (see text). The experimental results can be reproduced in the numerical calculation by an energy peak around $E_p - E_v = 0.7$ eV for interface defects. (b) Total recombination rate at the interface for the same structures as in (a) versus energetic position of the defect peak between valence and conduction band.

and carriers are defined through quasi-Fermi energies. In that case, it is necessary

to solve continuity, Poisson and transport equations by e.g. numerical simulation. The resulting band diagrams under illumination are shown in Figures 8.6(a) and (b). The photon flux and wavelength used for the simulation were $\phi = 1.6 \times 10^{18}$ photons $\text{cm}^{-2} \text{s}^{-1}$ and $\lambda = 782$ nm, in the experiment band diagrams under illumination change when shifting the energetic position of defects. Both structures show a different splitting of quasi-Fermi levels. In order to understand and clarify these differences, recombination and the influence of defect densities at the interface will be discussed in the following section.

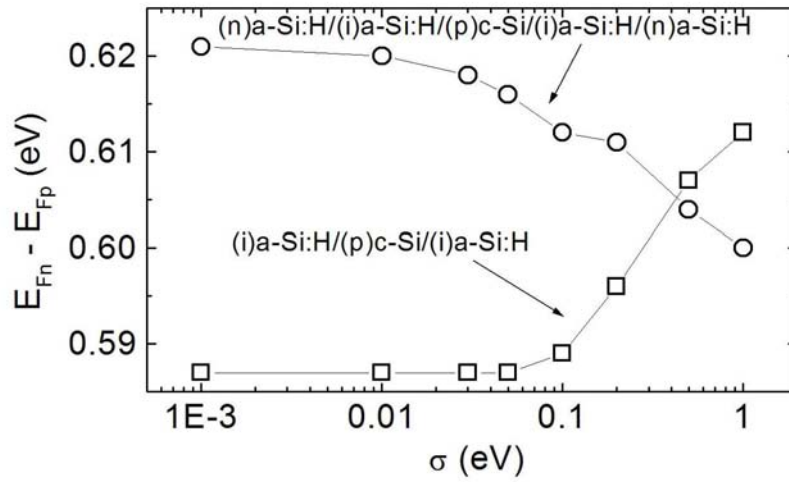


Figure 8.8: Splitting of quasi-Fermi levels of the symmetrical structures passivated with (i)a-Si:H and (n)a-Si:H/(i)a-Si:H versus width of the Gaussian distribution of defects at the interface. A continuous distribution of defects along the band gap does not reproduce the experimental results as the splitting of quasi-Fermi levels decreases from the first ((i)a-Si:H passivation) to the second step ((n)a-Si:H deposition) in the processing of the solar cell.

In the simulation I integrated the product of carrier densities over the crystalline wafer and obtained the averaged value of np . This integral equals the photoluminescence yield, which was considered spatially constant distributed for a very well passivated c-Si substrate. The average splitting of quasi Fermi levels was obtained from this \overline{np} :

$$E_{F_n} - E_{F_p} = kT \ln \left(\frac{\overline{np}}{n_0 p_0} \right) \quad (8.4)$$

Figure 8.7(a) shows the comparison of the splitting of quasi-Fermi levels obtained for both structures when varying the energy position of defects. The passivation with (i)a-Si:H reaches a minimum at midgap while adding (n)a-Si:H has a completely different behaviour, in that case $E_{F_n} - E_{F_p}$ increases when defects are moved

towards the conduction band. From the experimental results a difference of (25 ± 8) meV between the splitting of quasi-Fermi levels of both samples was found: it was calculated to be (600 ± 4) meV when the wafer was passivated with (i)a-Si:H and $E_{F_n} - E_{F_p}$ increases up to (625 ± 4) meV with the addition of an (n)a-Si:H layer. This result is marked with horizontal boxes in Figure 8.7(a) for the parameters mentioned above. The vertical box (solid line) includes the range of the position of defects which agrees with the experimental results for the parameters mentioned above. Changes in width (σ) and capture coefficients imply a modification of defect occupation and therefore variation of the recombination at the interface. This results in a wide parameter space for the simulation. For this reason I also show results when these parameters are varied. The crossed circles and squares in Figure (8.7(a)) represent the splitting of quasi-Fermi levels for the values: $\sigma = 0.1$ eV, $c_n^{D+} = 8 \times 10^{-8} \text{ cm}^3\text{s}^{-1}$, $c_n^{D0} = 4 \times 10^{-8} \text{ cm}^3\text{s}^{-1}$, $c_p^{D-} = 4 \times 10^{-8} \text{ cm}^3\text{s}^{-1}$ and $c_p^{D0} = 8 \times 10^{-9} \text{ cm}^3\text{s}^{-1}$. The same tendency can be observed when shifting the energy peak of defects to the conduction band for both structures for these chosen parameters. The box with a dashed line indicates again the range of possible positions for the energy peak of the interface defect distribution. From the addition of the possible ranges of $E_P - E_V$ within the boxes, it is obtained that the energy peak of the interface defect distribution should be around 0.7 eV.

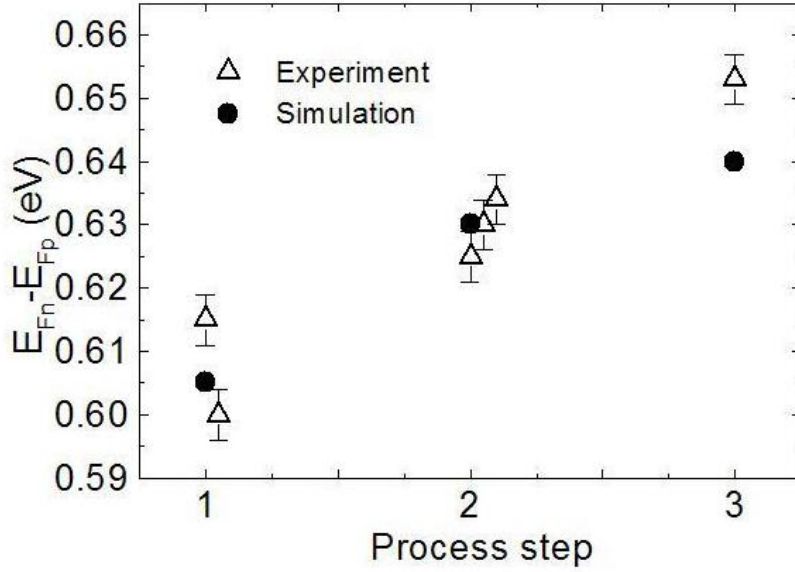


Figure 8.9: Splitting of quasi-Fermi levels from simulation and quantitative photoluminescence measurements for the first three process steps (1:(i)a-Si:H/(p)c-Si/(i)a-Si:H, 2:(n)a-Si:H/(i)a-Si:H/(p)c-Si/(i)a-Si:H/(n)a-Si:H, 3:(n)a-Si:H/(i)a-Si:H/(p)c-Si/(i)a-Si:H/(p)a-Si:H) shows good correlation with $E_{F_n} - E_{F_p}$ increasing progressively with the structures.

Among other studies [72, 51] a continuous interface defect distribution through

the band gap of c-Si has been derived. I also simulated the structure passivated with (i)a-Si:H (first step in the series) and with (n)a-Si:H/(i)a-Si:H (second step in the series) varying the width σ of the Gaussian distribution. Figure 8.8 shows the splitting of quasi-Fermi levels for both structures when there is a continuous defect distribution in the gap ($\sigma = 1$ eV). It does not increase following the processing steps but decreases, on the contrary to the experimental results. However, the mentioned studies [72, 51], show an increment of the density of states for energies close to the band edges and the energy peak of the distribution tend also to be closer to the conduction band.

Total recombination rate (parameters with $\sigma = 0.2$ eV) at the interface is shown in Figure 8.7(b). As expected, there is a clear anticorrelation between the splitting of quasi-Fermi levels and total recombination rate. A high interface recombination results in a decrease in minority carrier density and thus reduction of $E_{F_n} - E_{F_p}$ in the volume of the wafer.

The next step of the series of heterodiode deposition was the formation of a "back surface field" by adding a (p)a-Si:H in order to reduce recombination at the back contact. The heterostructure with a 20 nm (p)a-Si:H layer has a splitting of quasi-Fermi levels of 653 ± 4 meV. Figure 8.9 shows both the splitting of quasi-Fermi levels obtained from experiments and from simulation with $\sigma = 0.1$ eV. The scatter in the experimental data results from PL-measurements at different positions on the sample. There is a clear progressive increment of $E_{F_n} - E_{F_p}$ for both experimental and simulation results.

The effect of the (p)a-Si:H layer is depicted in Figure 8.10(a) in terms of the spatial variation of E_{F_n} and E_{F_p} of the three structures in Figure 8.9. In addition to the previous structures, simulation without any kind of "back surface field" has been done in order to get a better understanding of this effect. The splitting of quasi-Fermi levels for the latter was 522 meV. A detailed band diagram of all the structures at the back of the wafer is shown in Figure 8.10(b). Inspection of E_{F_n} for wafer structures 2 and 3 shows that the (p)a-Si:H layer leads to an increase in $E_{F_n} - E_{F_p}$ mainly at the (right) back side of the wafer while a direct contact of the (p)c-Si wafer with metal decreases considerably this splitting. This variation in E_{F_n} is maintained to a smaller degree in the whole device.

In order to compare the experimental with the simulated results the open-circuit voltage of the analysed solar cell under AM1.5 illumination was electrically measured [73] obtaining a value of 590 mV. The simulation yields $V_{OC} = 591$ mV with the fitted parameters from the wafer modelling under the same AM1.5 illumination conditions.

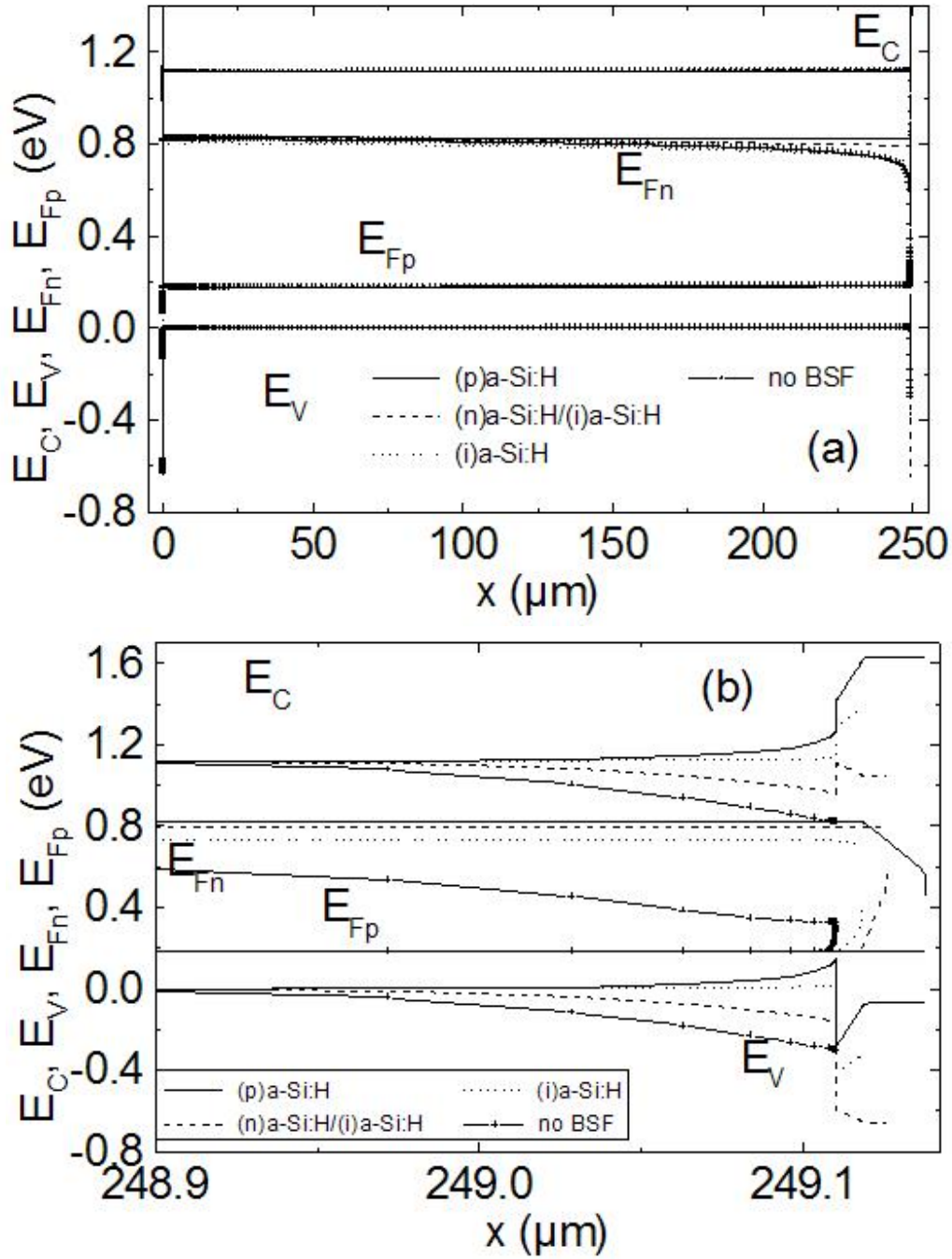


Figure 8.10: Band diagram and splitting of quasi-Fermi levels versus depth in the wafer (a) and at the back side (b) for the three different structures: passivation of p-type crystalline silicon at both sides with (i)a-Si:H, addition of (n)a-Si:H to form a pn-junction and formation of back surface field with (p)a-Si:H to reduce recombination.

8.3 Interpretation and discussion

After each of the processing steps of the a-Si:H/c-Si solar cell, quantitative PL yields increase progressively as it can be seen in Figure (8.2). The variation in the

occupation of interface defects which implies a reduction of recombination due to the Fermi level of the doped layer is suggested to be responsible for the increase in photoluminescence of the symmetric structures (i)a-Si:H/(p)c-Si/(i)a-Si:H and (n)a-Si:H/(i)a-Si:H/(p)c-Si/(i)a-Si:H/(n)a-Si:H. This diminished recombination at the interface increases the minority carrier density in the volume. This is confirmed in Figures 8.7(a) and (b), where an anticorrelation between the interface recombination and the splitting of the quasi-Fermi levels occurs. From comparison between the experimental and simulated splitting of quasi-Fermi levels for different parameters, it is suggested that the interface defect distribution is about 0.7 eV above E_V .

In order to understand the variation in the splitting of quasi-Fermi energies when defects are shifted through the band gap from the valence to the conduction band, the recombination at the interface has been studied.

I examined the occupation of defects and changes in the splitting of quasi-Fermi levels at the interface. In Figure (8.11) I plotted the densities of neutral, positively and negatively charged defects for both types of passivation in the dark (thermal and chemical equilibrium) and under illumination. The total interface defect density is given by the gaussian profile N_{if} from equation (8.3). The occupation probabilities in the dark are described by dangling bond statistics specified by formulas (B.3), (B.4) and (B.5) in Appendix B and by formulas (C.5) in Appendix C under illumination. Figures (8.12(a),(b) and 8.13(a), (b)) show numerical results of energetic defect distributions D^- , D^0 , D^+ as product of the total defect density N_{if} and the occupation probabilities. In equilibrium, the occupation of defects is determined by the position of the Fermi energy. For energies lower than E_F the levels are filled with electrons and due to this the density of negatively charged defects is larger than that of the positively charged ones. Energy levels above E_F are 'empty' and therefore positively charged defects govern these regions. At room temperature, neutral defects can capture or emit an electron, thus, they can be below or above the Fermi level. Differences of the E_F in both structures derive from different doping in a-Si:H. The (n)a-Si:H/(i)a-Si:H passivation is equivalent to a (n)a-Si:H passivation, as the (i)a-Si:H layer is very thin and does not change the position of E_F in comparison to the structure with a (n)a-Si:H film. The Fermi level is also shifted, when the defects are moved from the valence band to the conduction band, because due to its high density ($6.4 \times 10^{18} \text{ cm}^{-3}$) in comparison to the density of phosphorous atoms ($9.24 \times 10^{15} \text{ cm}^{-3}$) in the (p)c-Si substrate, doping at the interface is modified. For illuminated samples, the occupation of interface defects is determined by the quasi-Fermi energies.

Passivation with (i)a-Si:H is dominated by neutral and positively charged defects while passivation with (n)a-Si:H/(i)a-Si:H is governed by neutral and negatively charged defects. Therefore when studying the recombination at the (i)a-Si:H passivation I concentrate on the rates which give the capture of free electrons into

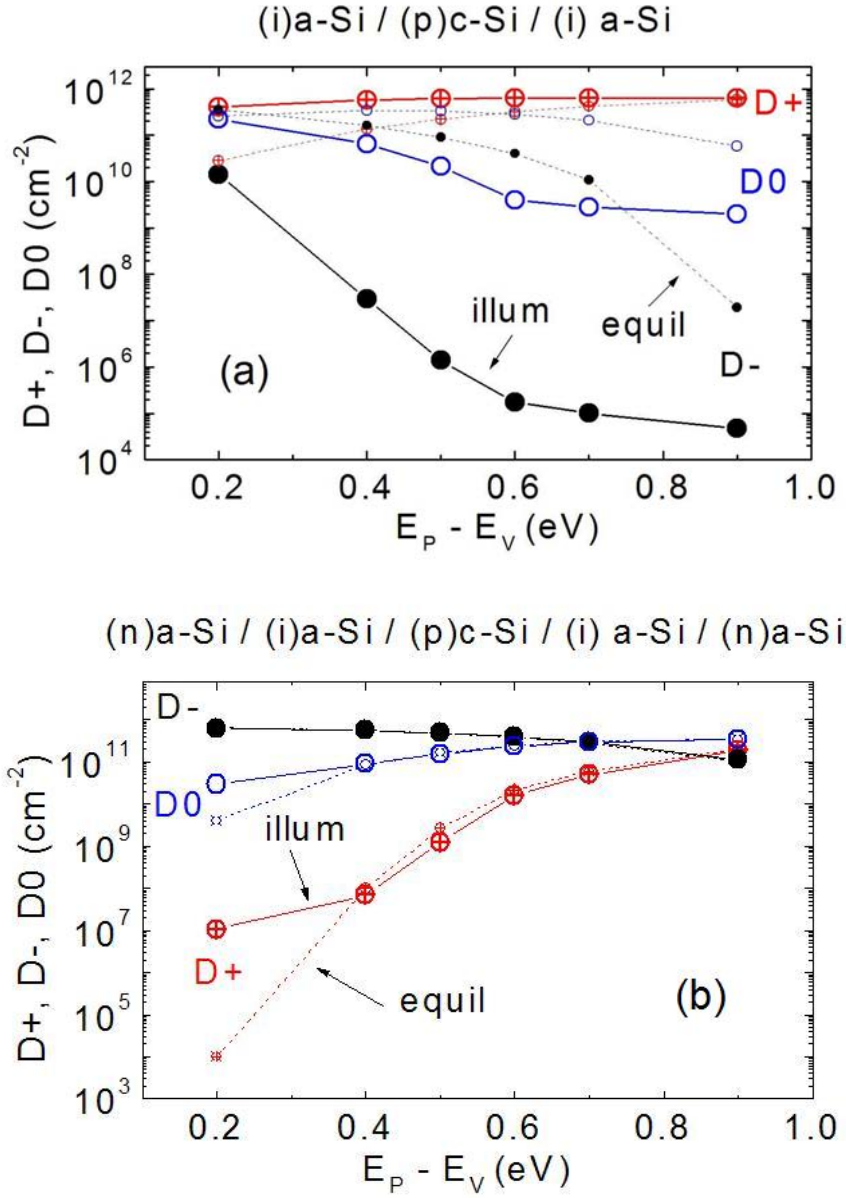


Figure 8.11: Densities of neutral, positively and negatively charged defects for the (a)(i)a-Si:H and (b)(n)a-Si:H/(i)a-Si:H passivation when the interface defect energy distribution peak is shifted along the bandgap from the valence to the conduction band.

positively charged defects ($R_n^{D^+}$), emission of electrons from neutral defects into the conduction band ($G_n^{D^0}$), capture of free holes into neutral defects ($R_p^{D^0}$) and emission of holes from positive charged defects into the valence band ($G_p^{D^+}$) for being all these rates determined by the densities of neutral and positively charged defects. For the same reason, I analyzed the rates for the capture of free electrons

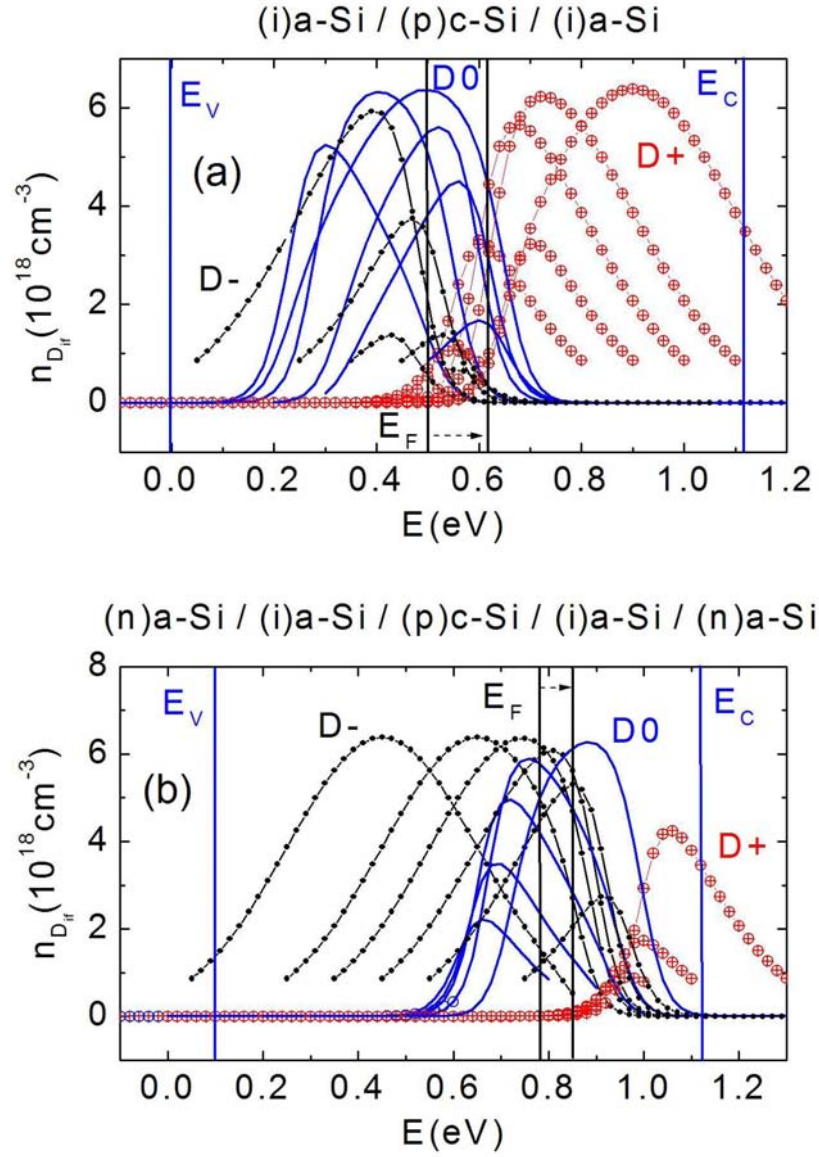


Figure 8.12: Densities of neutral, positively and negatively charged defects versus energy for the (i)a-Si:H (a) and (n)a-Si:H/(i)a-Si:H (b) passivation when the interface defect energy distribution peak for different energetic positions of the defect peak in the gap ($T = 300 \text{ K}$, no illumination).

into neutral defects ($R_n^{D^0}$), emission of electrons from negatively charged defects into conduction band ($G_n^{D^-}$), capture of free holes into negatively charged defects ($R_p^{D^-}$) and emission of holes from neutral defects into the valence band ($G_p^{D^0}$), which are the ones depending on densities of neutral and negatively charged defects, when analyzing the (n)a-Si:H/(i)a-Si:H passivation.

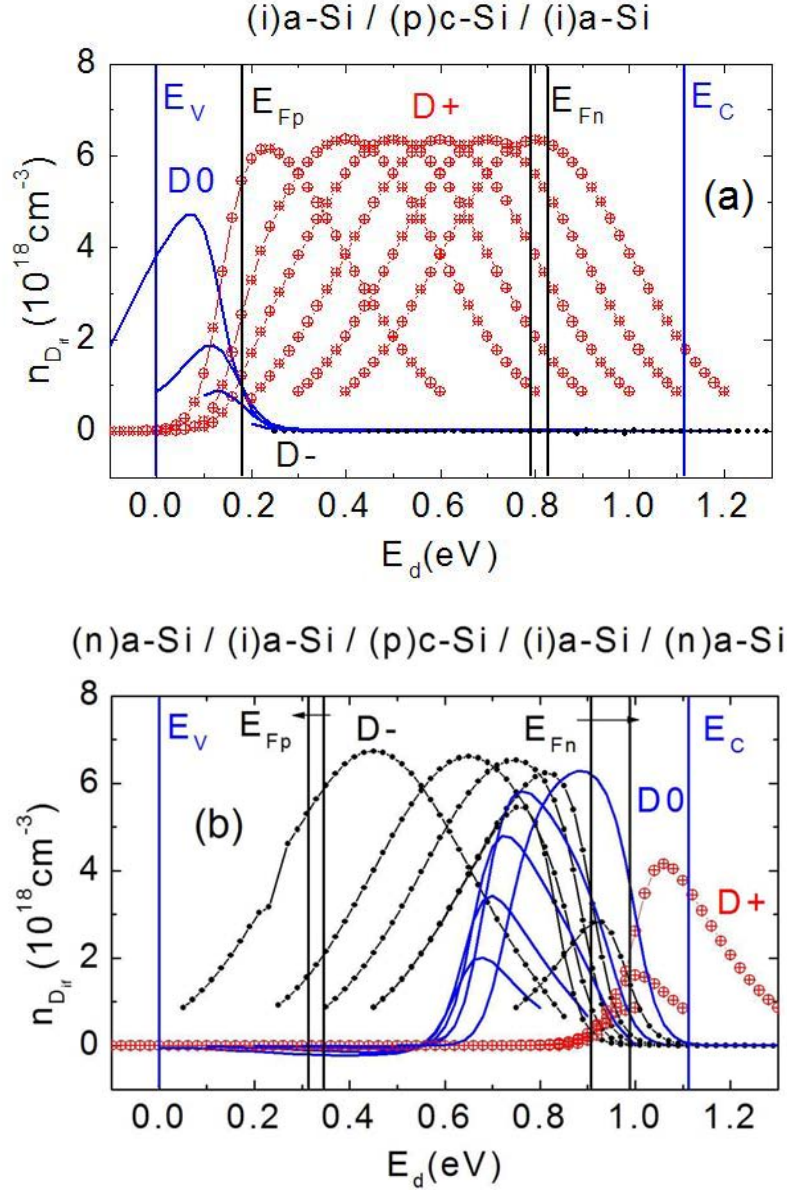


Figure 8.13: Densities of neutral, positively and negatively charged defects versus energy for the (i)a-Si:H (a) and (n)a-Si:H/(i)a-Si:H (b) passivation when the interface defect energy distribution peak for different energetic positions of the defect peak in the gap under illumination ($T = 300 \text{ K}$, $\Phi = 1.6 \times 10^{18} \text{ cm}^{-2}\text{s}^{-1}$).

A sketch of the predominant recombination rates is shown in figure (8.14). For the (i)a-Si:H passivation the recombination centers or defects are more effective when they are situated in the midgap. This agrees with the Shockley-Read-Hall recombination theory [19]. Due to this, the recombination at the interface is the largest for $E_P - E_V = 0.6 \text{ eV}$. When defects are close to valence band or conduction

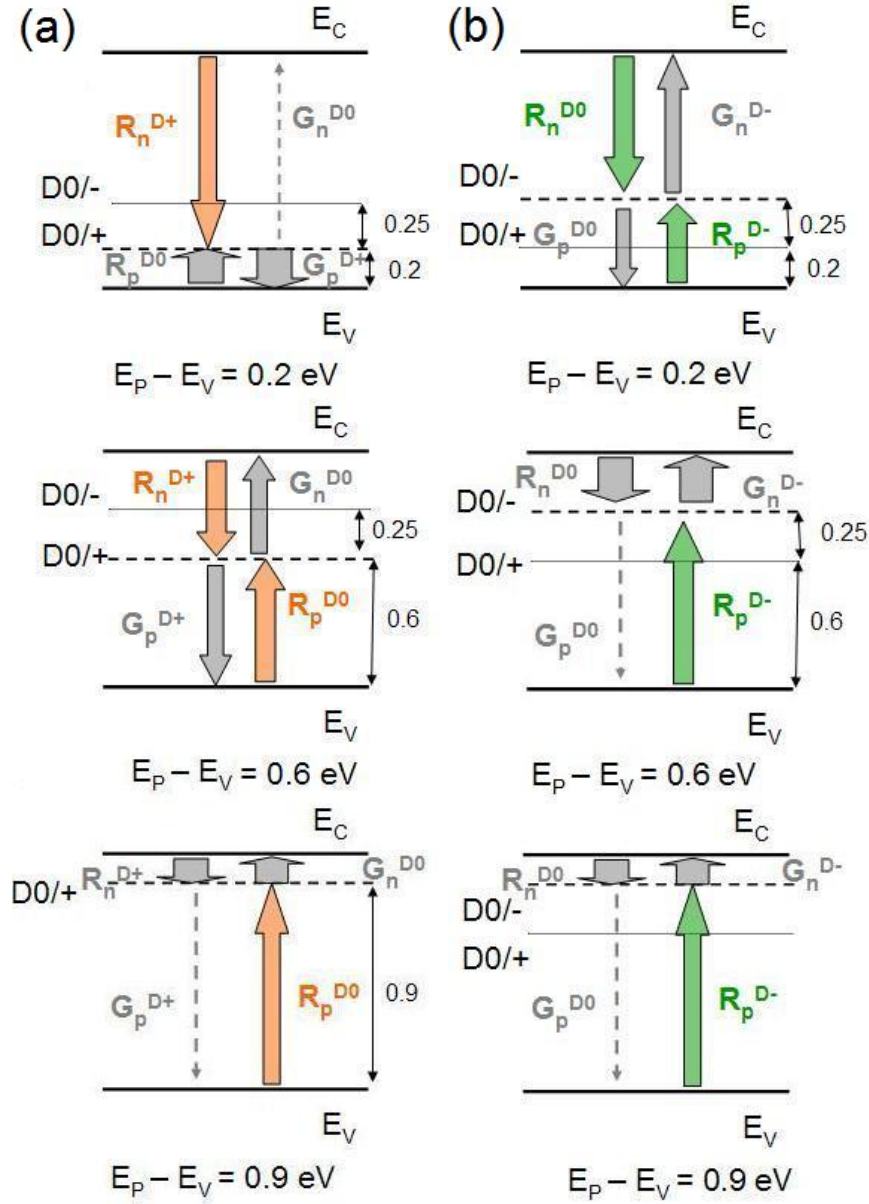


Figure 8.14: Predominant transition rates of electrons and holes in the a-Si:H/c-Si interface from numerical simulation for (a)(i)a-Si:H and (b)(n)a-Si:H/(i)a-Si:H passivation on c-Si wafers; peak of interface defect distribution at different positions $E_P - E_V = 0.2$ eV, 0.6 eV and 0.9 eV.

band recombination is reduced. As it can be seen in figure (8.14(b)), for $E_P - E_V = 0.2$ eV, the emission and capture rates between defects and the valence band are very high, but they compensate each other, do not control the total recombination. The mean recombination occurs via capture of free electrons by positively charged defects. When interface defects are situated in the middle of the gap, all recombination rates are similarly determining and therefore recombination is most effective.

For $E_P - E_V = 0.9$ eV, there is a similar situation as the first case discussed: the emission and capture rates between defects and conduction band are high but they compensate each other; the recombination is dominated by the capture of free holes into neutral defects. This rate is less for $E_P - E_V = 0.9$ eV than in $E_P - E_V = 0.2$ eV as neutral defect density is lower.

Equivalent arguments can be applied for the (n)a-Si:H/(i)a-Si:H passivation, but it should be noticed that in this structure the recombination is mainly governed by neutral and negatively charged defects. With the correlation energy between negatively charged defects and positive and neutral defects of 0.25 eV, when positive and neutral defects are situated at 0.2, 0.6 and 0.9 eV, negatively charged defects are centered at 0.45, 0.85 and 1.15 eV.

The diagrams (8.14(a)) show that recombination is most effective for $E_P - E_V = 0.2$ eV, and the negative defects near midgap. In the other two cases ($E_P - E_V = 0.6$ eV and $E_P - E_V = 0.9$ eV) the negative defects are closer to the conduction band and emission and capture rates of free electrons by defects are high but compensate each other and recombination is dominated by capture of free holes by negatively charged defects.

The effect of a "back surface field" has been illustrated in Figures 8.10(a) and (b). The addition of a (p)a-Si:H layer enhances considerably the splitting of quasi-Fermi levels from 522 meV (without any a-Si:H layer at the back of the wafer) to 653 meV ((i)a-Si:H/(p)a-Si:H passivation). The diffusion of electrons to the contact and corresponding increase in recombination at the back interface is avoided by the deposition of a (p)a-Si:H as "back surface field". Due to band matching the (p)a-Si:H is the best passivation layer for a reduction of electron density at the interface and therefore less recombination over defects.

For the non-symmetrical samples after ZnO and Al deposition, changes in PL yield are mainly due to variations in the coupling of light into and also PL out of the wafer. The increase in $E_{F_n} - E_{F_p}$ when the ZnO layer is added can be explained by a higher excitation and larger emission flux due to variations in the reflection and absorptivity of the wafer which lead to an increase of the quasi-Fermi level splitting. Similarly, reflection of PL radiation at the Al back contact increases the PL yield, which is taken into account for the determination of $E_{F_n} - E_{F_p}$ so that no further increase in comparison with the ZnO structure is expected. In our experiments the structure with Al shows a still higher $E_{F_n} - E_{F_p}$. Thus, the deposition of Al at the back side of the wafer do improve the open circuit voltage of solar cell. Diffusion of Al into the (p)a-Si:H layer may enhance the passivation properties of the back interface, reducing recombination and explaining this increase of the splitting of quasi-Fermi levels.

Chapter 9

Photoluminescence at different operating modes of an illuminated heterodiode

9.1 Photoluminescence of solar cells at open circuit and short circuit

Photoluminescence is analyzed for two modes of operation of heterodiodes. At open circuit voltage (V_{oc}) there is no current extracted from the cell and thus, all carriers generated should recombine to establish the steady-state. At short circuit current (J_{sc}), a strong extraction of carriers occurs. Therefore a high non-radiative recombination takes place at the contacts and the radiative recombination rate is reduced.

Photoluminescence, local profiles of carrier concentrations and splitting of quasi-Fermi levels of a-Si:H/c-Si heterojunctions at both operation modes have been numerically modelled. Interface defect densities have been varied in order to study the variation in PL yields. The simulations were done for a temperature of 300 K and a photon flux of $\Phi = 10^{18} \text{cm}^{-2} \text{s}^{-1}$ with a monochromatic irradiation at a wavelength of $\lambda = 782 \text{ nm}$. The structure simulated was a p-type crystalline silicon substrate with a doping density of $9.24 \times 10^{15} \text{cm}^{-3}$ and a thickness of $250 \mu\text{m}$; for the window layer a 30 nm thick (n)a-Si:H was used. The interface defects have been introduced by a thin (p)c-Si layer with the same parameters as the substrate, containing a higher concentration of defect states with $N_{if} = (0, 2 \times 10^{11}, 6 \times 10^{11}, 2 \times 10^{12}, 2 \times 10^{13}, 2 \times 10^{14} \text{cm}^{-2})$. $N_{if} = 0 \text{cm}^{-2}$ means that minority carriers in the defect regime have lifetimes like in the bulk. The defects have a very narrow Gaussian distribution ($\sigma = 0.001 \text{ eV}$) positioned in the middle of the gap ($E_p = E_V + 0.55 \text{ eV}$) with capture cross sections $2.2 \times 10^{-15} \text{cm}^2$ and $2.2 \times 10^{-16} \text{cm}^2$ for the capture by positive and neutral defects and $1.8 \times 10^{-15} \text{cm}^2$ and $1.8 \times 10^{-16} \text{cm}^2$ for the capture of holes

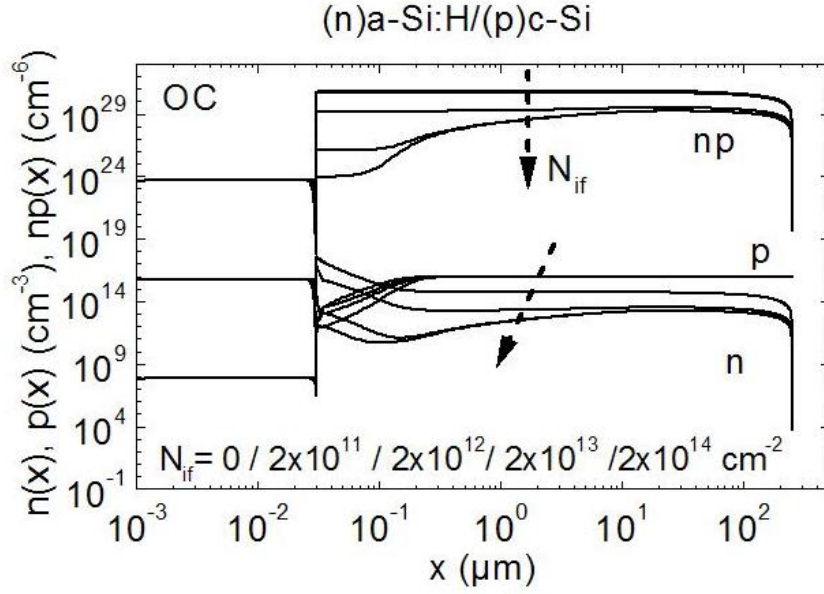


Figure 9.1: Simulated local carrier densities $n(x)$, $p(x)$ and its product $(n(x)p(x))$ of a (n)a-Si:H/(p)c-Si solar cell in open circuit voltage for different interface defect densities $N_{if} = 0, 2 \times 10^{11}, 2 \times 10^{12}, 2 \times 10^{13}, 2 \times 10^{14} \text{ cm}^{-2}$.

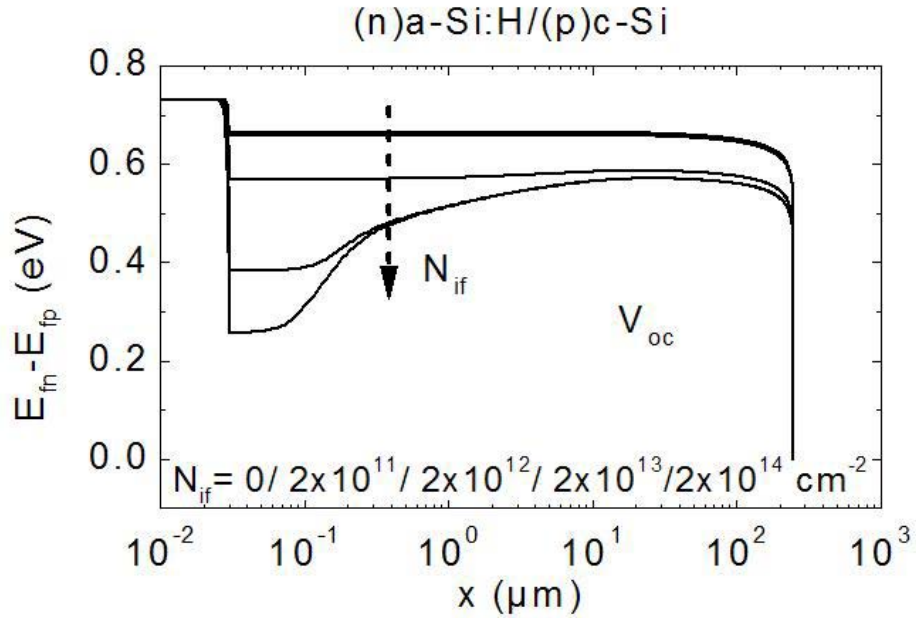


Figure 9.2: Simulated splitting of quasi-Fermi levels ($E_{Fn} - E_{Fp}$) of a (n)a-Si:H/(p)c-Si solar cell in open circuit for different interface defect densities N_{if} . For very low interface defect densities $E_{Fn} - E_{Fp}$ in the bulk does not vary spatially.

by negative and neutral defects respectively. The thickness of the interface defect layer is 5 nm. The boundary conditions at the front and back of the solar cell in the simulation are given by an ohmic contact between the metal and the semiconductor.

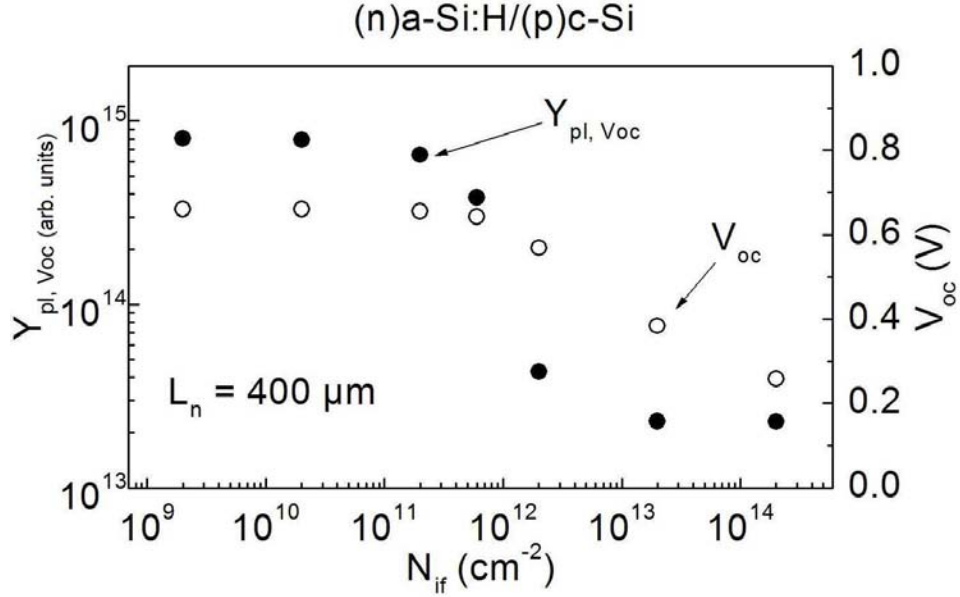


Figure 9.3: Comparison of the simulated photoluminescence yield in open circuit $Y_{pl,OC}$ and electrical open circuit voltage V_{OC} for an (n)a-Si:H/solar cell for different interface defect densities N_{if} .

Figure 9.1 shows the local charge carrier densities under illumination in open circuit for various interface defect densities N_{if} . With increasing N_{if} , the density of minority carriers is considerably reduced in the bulk. This is also reflected in the product $n \cdot p$, whose logarithm is proportional to the splitting of quasi-Fermi levels in the device. Figure 9.2 shows the corresponding $E_{F_n} - E_{F_p}$. At high interface defect densities (ca. $N_{if} > 10^{13} \text{ cm}^{-2}$) the splitting in the bulk saturates. However, such large N_{if} are not realistic for good quality solar cells, which have interface defect densities $N_{if} \in (10^{11} \dots 10^{12} \text{ cm}^{-2} \text{ s}^{-1})$. For the selected set of geometrical parameters of the hetero-junction the splitting of quasi-Fermi levels and photoluminescence yield are very sensitive against the density of defects at the interface when the device is in V_{oc} modus.

In Figure 9.3 the numerically calculated open circuit voltages V_{oc} and the luminescence yield $Y_{pl,Voc}$ from spatial integration of the products of carrier densities $n(x)p(x)$ over the absorber thickness d are displayed, both versus interface defect density N_{if} , demonstrating the different regimes of sensitivity of these magnitudes. V_{oc} feels interface defect densities from some $2 \times 10^{11} \text{ cm}^{-2}$ and varies by a factor of 2 when N_{if} reaches 10^{14} cm^{-2} . The luminescence $Y_{pl,Voc}$ is extremely sensitive

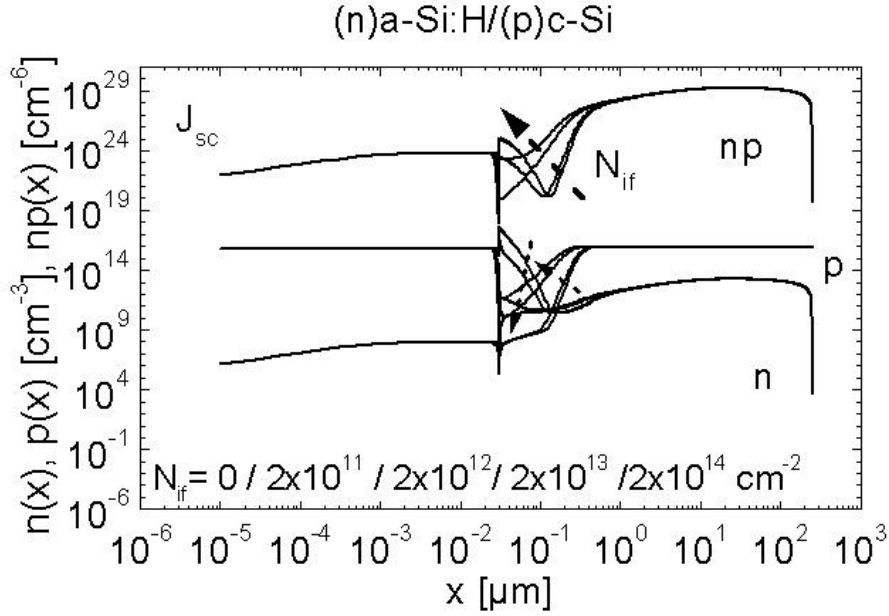


Figure 9.4: Simulated local carrier densities $n(x)$, $p(x)$ and its product $(n(x)p(x))$ of an (n)a-Si:H/(p)c-Si solar cell in short circuit for different interface defect densities N_{if} .

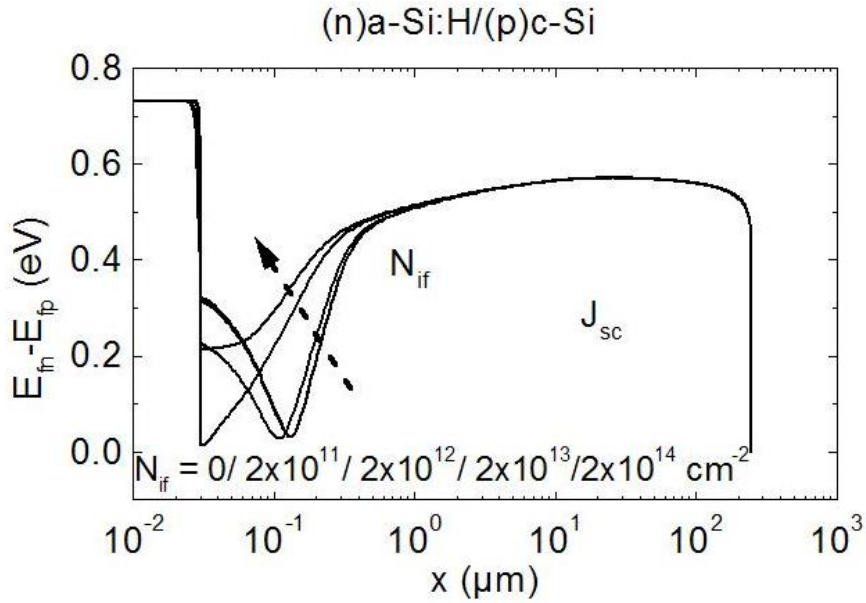


Figure 9.5: Simulated splitting of quasi-Fermi levels $(E_{Fn} - E_{Fp})$ of an (n)a-Si:H/(p)c-Si solar cell in short circuit for different interface defect densities N_{if} .

(factor 30) against a variation of N_{if} in $5 \times 10^{10} \text{cm}^{-2} < N_{if} < 2 \times 10^{12} \text{cm}^{-2}$.

Figures 9.4 and 9.5 show also the local carrier densities and its product in logarithmic scale and the splitting of quasi-Fermi levels under illumination but in short circuit. Variations in the interface defect densities do not affect the distribution of carriers nor the $E_{Fn} - E_{Fp}$ in the c-Si bulk. Close to the interface, minority and majority densities are governed also by the continuity equation and they are noticeably different than in open circuit conditions due to the extraction of carriers towards contacts.

9.1.1 Simulation of $Y_{pl,Voc}/Y_{pl,Isc}$ and estimation of interface defect densities

As the PL yields at short circuit conditions, $Y_{pl,Isc}$ are very insensitive to the interface quality and whereas in the open circuit, the luminescence is substantially affected by the interface defect density, the ratio $Y_{pl,Voc}/Y_{pl,Isc}$ has been used to estimate the interface N_{if} .

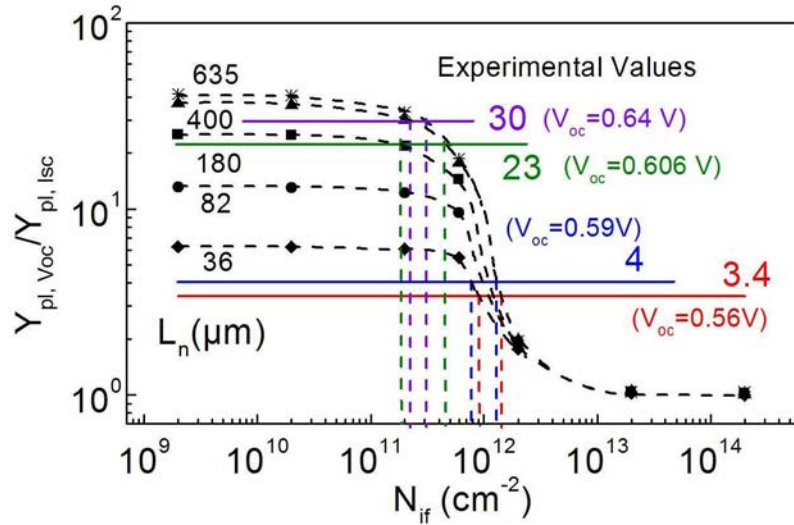


Figure 9.6: Variation of the ratio $Y_{pl,Voc}/Y_{pl,Isc}$ with increasing defect density, determined from simulated PL yields at short circuit and open circuit ($\Phi = 10^{18} \text{cm}^{-2} \text{s}^{-1}$). The horizontal lines show the values obtained from experimental measurements of solar cells. A range for the interface defect densities can be estimated for the different diffusion lengths simulated.

In order to estimate the defect density at the interface, an a-Si:H/c-Si solar cell was simulated with variation of the defect density in the bulk (different bulk lifetimes, i.e, different diffusion

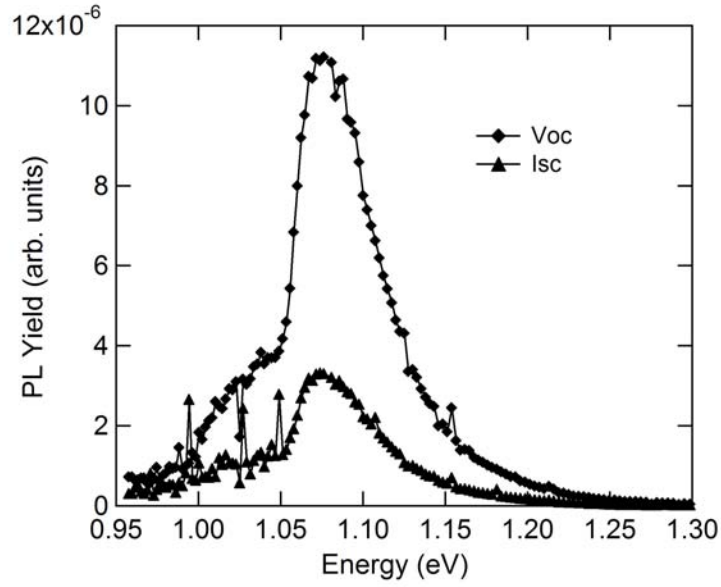


Figure 9.7: PL yield in short-circuit and open-circuit for an (n)a-Si:H/(p)c-Si solar cell. The ratio $Y_{pl,V_{oc}}/Y_{pl,I_{sc}}$ is 3.4.

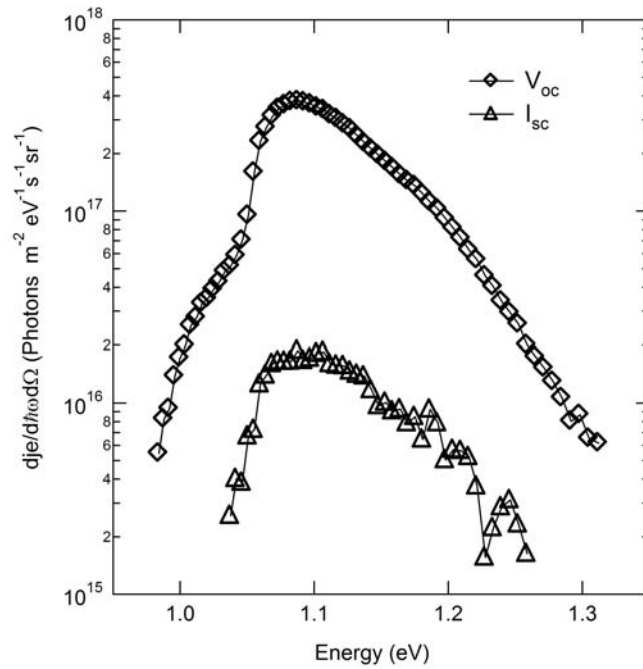


Figure 9.8: PL yield in short-circuit and open-circuit for an (n)a-Si:H/(p)c-Si solar cell. The ratio $Y_{pl,V_{oc}}/Y_{pl,I_{sc}}$ is 23.

lengths ($L_n = 36, 82, 180, 400$ and $635 \mu m$). In addition, the interface defect density was varied independently. The photoluminescence yield was calculated as the integral $\int B(T)n(x)p(x)dx$, where $B(T)$ is the radiative recombination coefficient. The simulation was performed at open circuit and short circuit conditions and the ratio between both modes of operation is shown in Figure 9.6 versus N_{if} . PL ratios are smaller at lower diffusion lengths up to $N_{if} = 5 \times 10^{12} cm^{-1}$. For interface defect concentrations larger than the latter, the ratio saturates for all L_n due to the high recombination rate at the interface. In this case, for large diffusion lengths, high carrier densities reach the interface and they recombine at the interface defects. The higher the diffusion length, the smaller the N_{if} at which the ratio starts to decrease. This happens because for higher diffusion lengths, the carrier density can diffuse over larger distances and therefore reach the interface and recombine. Another effect to be noticed is, that the ratio $Y_{pl,Voc}/Y_{pl,Isc}$ does not increase for large L_n for high interface defect densities. If the diffusion length is larger than the thickness of the wafer, the same number of electrons (as for $L_n = d$) reach the surface and recombine there.

The photoluminescence yield was measured at open circuit and short circuit conditions and the ratio $Y_{pl,Voc}/Y_{pl,Isc}$ was calculated for 4 different a-Si:H/c-Si solar cells. All these cells have similar substrates but were processed with different procedures. Figures 9.7 and 9.8 show the experimental photoluminescence spectra of two a-Si:H/c-Si solar cells in linear and logarithmic scala respectively. Both PL curves at I_{sc} and V_{oc} have the same spectral distribution but at short circuit condition PL is reduced due to the substantial extraction of carriers to the contacts. The ratio of $Y_{pl,Voc}/Y_{pl,Isc}$ amounts to 23 and 3.4, so that the interface defect density is larger for the lower value 3.4.

The values of the experimental PL ratios are those introduced in Figure 9.6. The interface defect density can be estimated if the diffusion length is known. For unknown L_n it is only possible to determine a range for N_{if} . High values of $Y_{pl,Voc}/Y_{pl,Isc}$ account for larger diffusion lengths and smaller interface defect densities, as expected. For example, for a ratio of 30 and 4, $N_{if} \in (2 \times 10^{11} \dots 3 \times 10^{11} cm^{-2})$ and $N_{if} \in (8 \times 10^{11} \dots 1.4 \times 10^{12} cm^{-2})$. In the Figure $Y_{pl,Voc}/Y_{pl,Isc}$ the open circuit voltages are also shown. The higher the photoluminescence ratio, the larger is the open circuit voltage, as it is predicted by the Planck's generalized Law.

9.2 I-V-characteristics from photoluminescence

From the splitting of quasi-Fermi levels estimated from PL it is possible to calculate a potential drop $V = (E_{Fn} - E_{Fp})/q$. In this section, I compare it with the potential difference between the contacts measured electrically at the same extracted current. From this comparison, it is possible to identify where the losses in the splitting of quasi-Fermi levels in the solar cell take place.

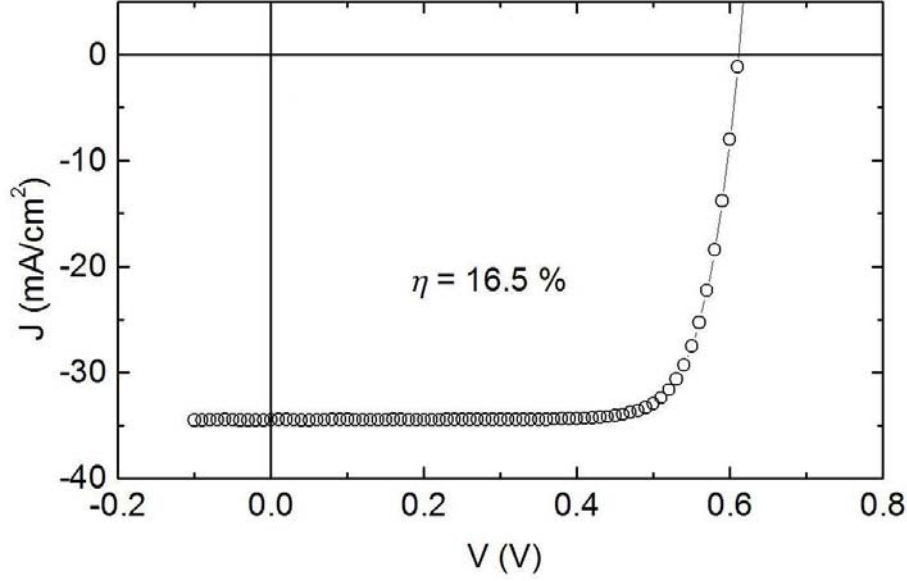


Figure 9.9: I-V-curve of a high efficiency (16.5%) a-Si:H/c-Si solar cell measured under 1.5 AM equivalent photon-flux and processed at the Hahn Meitner Institute (Berlin).

The examined solar cell was completely processed at the Hahn Meitner Institute (HMI) in Berlin using a $220\text{ }\mu\text{m}$ float zone wafer, $0.5\text{-}2\text{ }\Omega\text{cm}$ and texturized with non regular pyramids at front and back side. The (n)a-Si:H layer has a thickness of 8 nm. At the back a 30 nm (p)a-Si:H wafer for a back surface field was deposited. ZnO (80nm) was used as conductive antireflection layer. The contacts at both sides are evaporated Aluminum. The I-V-characteristics measured under 1.5 AM equivalent excitation at the HMI is shown in Figure 9.9. The solar cell has an efficiency of 16.5 %.

For the photoluminescence measurements, the front side of the solar cell was illuminated by a laser beam with a wavelength of 514 nm and an AM1.5 equivalent photon flux ($\Phi \approx 2.5 \times 10^{17} \text{ cm}^{-2} \text{ s}^{-1}$). The optics of the setup was modified in order to focus the illuminated area over the sample as homogeneous as possible, getting variations of around 15%. Figure 9.10 shows the quantitatively measured PL of the solar cell in open circuit conditions. The absorptivity of this heterostructure can not be properly described by non wavelength dependent reflection coefficients. The texturized surface builds a much complex optical system, which would need energy dependent reflection coefficients at the front ($R_F(\hbar\omega)$) and at the back ($R_B(\hbar\omega)$) of the wafer. Therefore, for the calculation of the splitting of the quasi-Fermi levels I used the same procedure described in chapter 7 where the absorption coefficient and thus $A(\hbar\omega)$ were not known. For photon energies $\hbar\omega \geq 1.25\text{ eV}$, the absorptivity of the silicon wafers is given by $A(\hbar\omega) \approx (1 - R_F)$, being R_F the reflection at the front of the wafer. In Figure 9.11 the reflection measured from the solar cell is

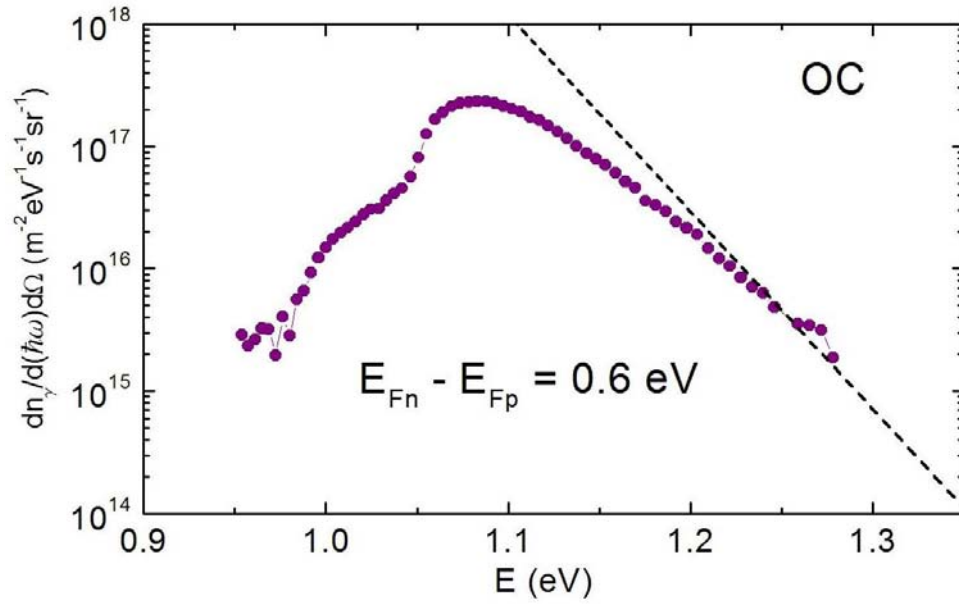


Figure 9.10: Quantitative photoluminescence from an a-Si:H/c-Si solar cell in open circuit voltage (OC) and derived splitting of quasi-Fermi levels.

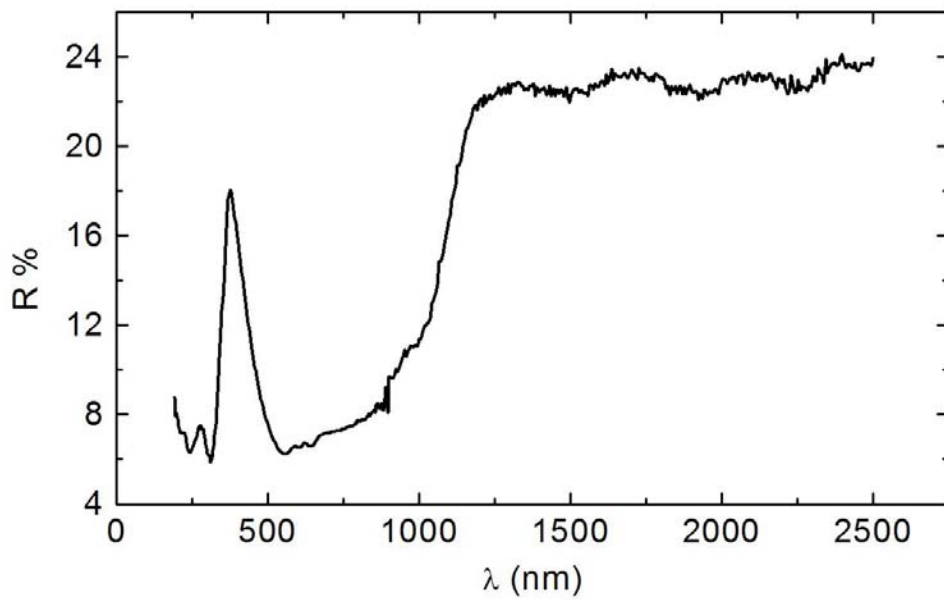


Figure 9.11: Reflection measured from the a-Si:H/c-Si solar cell. For $\hbar\omega > 1.25 \text{ eV}$ ($\lambda < 992 \text{ nm}$), $R(\hbar\omega) \approx R_F(\hbar\omega) \approx 11\%$ has been assumed.

shown. For high photon energies ($\hbar\omega \geq 1.25$ eV), it has been considered that the measured $R(\hbar\omega)$ is mainly due to the reflection at the front of the wafer. A value of $R = R_F = 0.11$ was measured. The splitting of quasi-Fermi levels $E_{F_n} - E_{F_p} = 0.600 \pm 0.004$ eV was obtained adjusting the curve generated from the Planck's generalized Law for high photon energies (at $\hbar\omega \approx 1.25$ eV), which is shown in Figure 9.10 with a black dashed line.

The measurement of the I-V-characteristics with a digital multimeter and the luminescence at the wavelength of maximum emission ($\lambda \approx 1140$ nm, $\hbar\omega = 1.08$ eV) was done consecutively from $V = V_{OC}$ till $V = 0V$. Assuming $V = (E_{F_n} - E_{F_p})/q$ (q is the electron charge) and as the splitting of quasi-Fermi levels is proportional to the logarithm of the PL yield, the voltage of the PL-IV curve has been computed as:

$$V_i = V_{OC} - \frac{kT}{q} \ln \left(\frac{dn_{\gamma, V_{OC}}(1.08eV)}{dn_{\gamma, V_i}(1.08eV)} \right) \quad (9.1)$$

This calculation implies that the minority carrier distribution and thus the splitting of quasi-Fermi levels are spatially constant independent of the extracted current. Furthermore, in the measured wafers, PL has the same spectral distribution at each operation point, so that the difference between PL-yields at maximum is the same as the difference for higher photon energies, where $E_{F_n} - E_{F_p}$ is derived. Therefore, once the splitting of quasi-Fermi levels and its derived potential drop is calculated for open circuit conditions, $E_{F_n} - E_{F_p}$ and V can be easily derived by comparison of PL-yields at maximum using 9.1.

In order to identify if series resistance losses are included in the PL-I-V curve, I have extracted the R_s value of the electrically measured curve and compared it with the I-V-curve obtained from PL. The calculation of R_s was made according to the method explained in [74], where the lumped series resistance is computed for an illuminated and dark I-V-curve which are shown in Figure 9.12. In our case, there is no variation of the series resistance with and without illumination and it has a value of 3.16Ω . For the calculation of the I-V-curve without the effects of R_s , it has been assumed that the parallel resistance is very high ($R_p = \infty$), as the solar cell has a very high efficiency, and thus it can be neglected. The equivalent circuit of the solar cell without and with a series resistance is given by Figure 9.13(a) and 9.13(b) respectively. Solving the equations of the circuit (b), from which we have the current and voltage values from the measurement it is possible to get the reverse current J_o and the current generated by illumination J_L :

$$J = J_o \left\{ \exp \left[\frac{q(V - JR_s)}{kT} \right] - 1 \right\} - J_L \quad (9.2)$$

$$J_L = J_o \left\{ \exp \left[\frac{q(V_{oc})}{kT} \right] - 1 \right\} \quad (9.3)$$

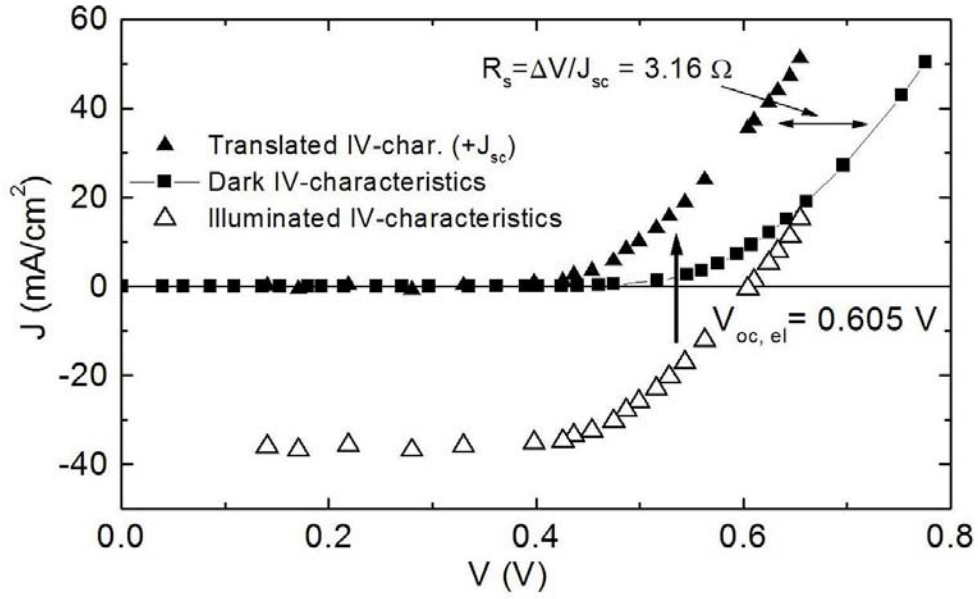


Figure 9.12: Measured illuminated and dark I-V-characteristics. The series resistance has been calculated shifting the illuminated I-V-characteristics by the photocurrent J_{sc} according to the method explained in [74].

$$J_o = \frac{J_{sc}}{\left[\exp\left(\frac{-qJ_{sc}R_s}{kT}\right) - \exp\left(\frac{qV_{oc}}{kT}\right) \right]} \quad (9.4)$$

The I-V-curve of the circuit (a) without series resistance is given by:

$$J = J_o \left[\exp\left(\frac{qV_D}{kT}\right) - 1 \right] - J_L \quad (9.5)$$

with $J_L = 35.9 \text{ mAcm}^{-2}$ and $J_o = 2.46 \times 10^{-9} \text{ mAcm}^{-2}$.

The PL-I-V curve and the I-V-characteristics without R_s are shown in Figure 9.14. The error from the inaccuracy in the determination of the splitting of quasi-

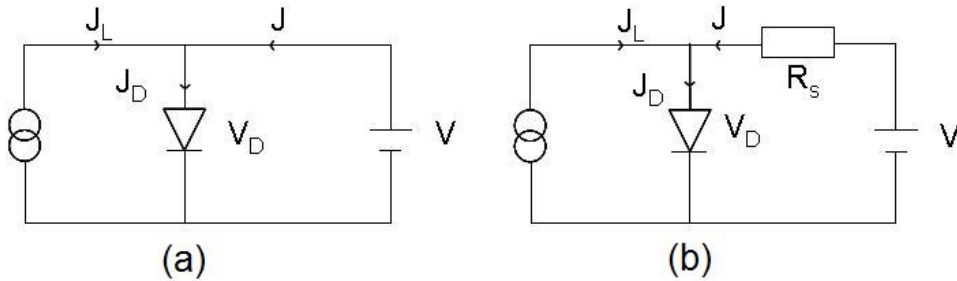


Figure 9.13: Equivalent circuit of a solar cell (a) without and (b) with series resistance R_s .

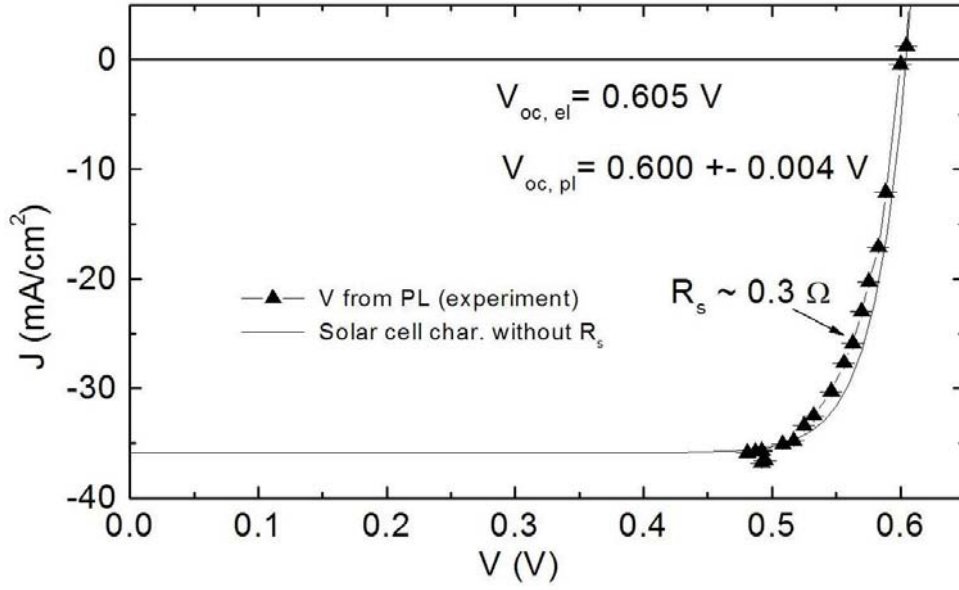


Figure 9.14: I-V-curve without R_s and photoluminescence at different operation points of the solar cell as in Figure 9.9.

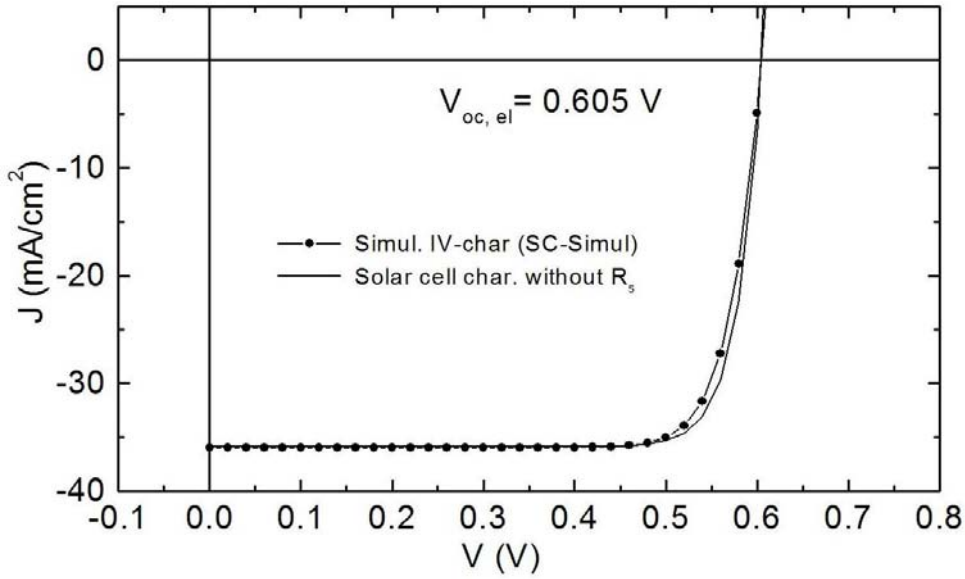


Figure 9.15: Simulated I-V-curve of a high efficiency a-Si:H/c-Si solar cell and calculated solar cell characteristic without series resistance with the same open circuit voltage ($V_{oc} = 0.605$ V) and short circuit current ($J_{sc} = 35.9$ mA/cm²) as the electrically measured I-V-curve.

Fermi levels is also included in the graph. The difference between both curves can be explained introducing a small series resistance $R_s = 0.3\Omega$ to simulate the IV-characteristics derived from photoluminescence using the circuit from Figure

9.13(b). At open circuit voltage, as there is no current flowing through the cell, and therefore there is also no voltage drop at R_s , both measured V_{OC} should be equal. In our case, the electrically measured and from photoluminescence derived open circuit voltage have the values $V_{OC,el} = 0.605$ V and $V_{OC,pl} = 0.600 \pm 0.004$ V, being ± 0.004 V the inaccuracy implied by PL measurements (see Appendix A). For short circuit conditions, it is expected that photoluminescence is reduced because carriers which are extracted do not contribute to PL. In opposite to open circuit conditions, at J_{sc} there is a large difference between both measured voltages: $V_{sc,el} = 0$ V and $V_{sc,pl} = 0.48$ V.

With the goal to understand the previous results I have simulated the I-V- and PL-I-V-curve of an a-Si:H/c-Si solar cell with the SC-Simul program. The input parameters have been selected so that this heterostructure has the same open circuit voltage and short circuit current as the measured one and the effective lifetime is around $350 \mu s$. The simulated solar cell has a 10 nm n-doped amorphous silicon film and a 2 nm defect layer with a $N_{if} = 10^{12} cm^{-2}$ in the front and back side of the silicon wafer. The defects were simulated by a very thin Gauss distribution ($\sigma = 0.001$ eV) in the middle of the gap and same parameters as the c-Si substrate. The back side was simulated as a (p)a-Si:H layer (30 nm thickness). Contacts are simulated by an ideal ohmic contact so that no voltage drop through a contact series resistance is expected.

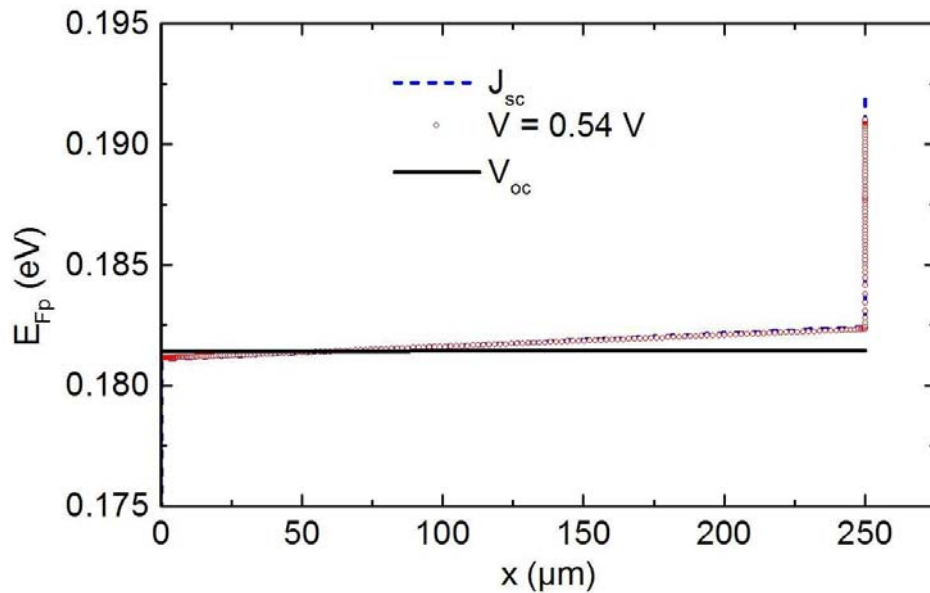


Figure 9.16: Simulated E_{Fp} for different applied voltages: V_{oc} , $V = 0.54$ V and $V = 0$ V (J_{sc}). It can be noted a voltage drop at the back of the wafer for high currents.

Figure 9.15 shows the measured IV-characteristic without series resistance (continuous line) together with the simulated IV-curve (circles). The simulated curve does

not follow the curve without series resistance in Figure 9.15. The applied voltage is given by $V = (E_{F_p}(0) - E_{F_n}(d))/q$, being $E_{F_n}(0)$ the quasi-Fermi level of electrons at the front of the wafer and $E_{F_p}(d)$ the quasi-Fermi level of holes at the back of the wafer. In Figure 9.16, E_{F_p} is shown for three different operation points: V_{oc} , $V = 0.54$ V and J_{sc} . There is a voltage drop at the back contact for high current, which can be modelled by a series resistance $R_s = 0.3\Omega$. As this voltage drop occurs just in a very small region close to the back contact, the integral in the volume of the charge carriers np as well as PL are not affected.

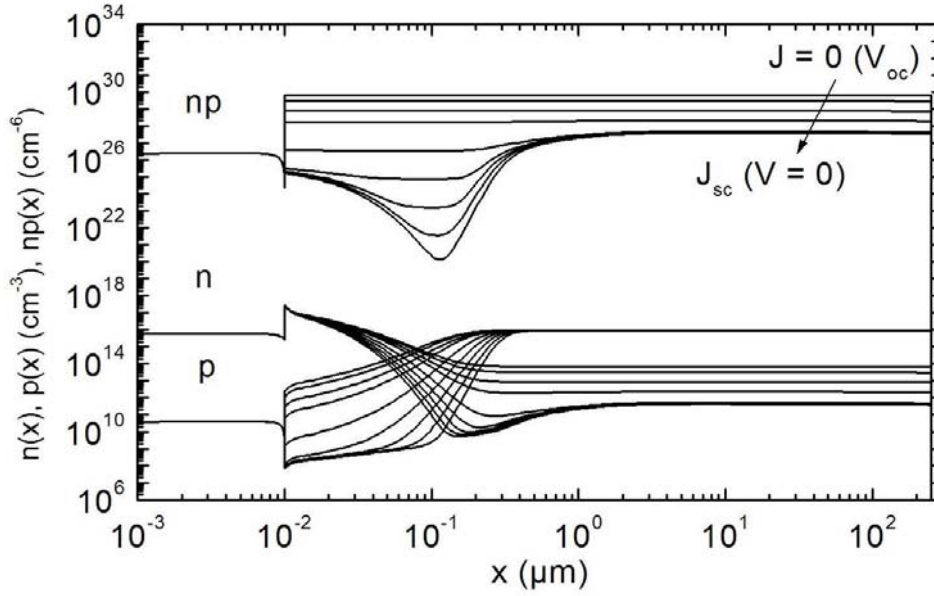


Figure 9.17: Simulated spatial distributions of electron and hole densities of a a-Si:H/c-Si solar cell for different operation points between open circuit voltage and short circuit conditions.

Figures 9.17 and 9.18 show the simulated local distribution of electrons (n) and holes (p) and their product, and the band diagram, respectively, of the a-Si:H/c-Si structure for different operating points from open circuit voltage to short circuit conditions. From PL, the difference between the quasi-Fermi levels of electrons obtained, is the averaged over the volume. At open circuit conditions, the splitting of quasi-Fermi levels of electrons and holes are constant in Figure 9.18 and therefore $E_{F_n}(x) = E_{F_n}$ and $E_{F_p}(x) = E_{F_p}$. Thus, $V = (E_{F_p}(0) - E_{F_n}(d))/q = (E_{F_p} - E_{F_n})/q$, where $E_{F_p} - E_{F_n}$ is the difference of the chemical potential calculated from photoluminescence. Due to the extraction of carriers by the contacts, n and p are not constant. This spatial variation is also reflected in the quasi-Fermi levels as the gradient of E_{F_n} and E_{F_p} describes the current densities of electrons and holes respectively [29]: $j_n = \sigma_n \text{grad}(E_{F_n})/q$ and $j_p = \sigma_p \text{grad}(E_{F_p})/q$ being σ_n and σ_p the conductivities of electrons and holes. For a p-type semiconductor the gradient is mainly in E_{F_n} and the current is produced by the electrons. Due to the spatial

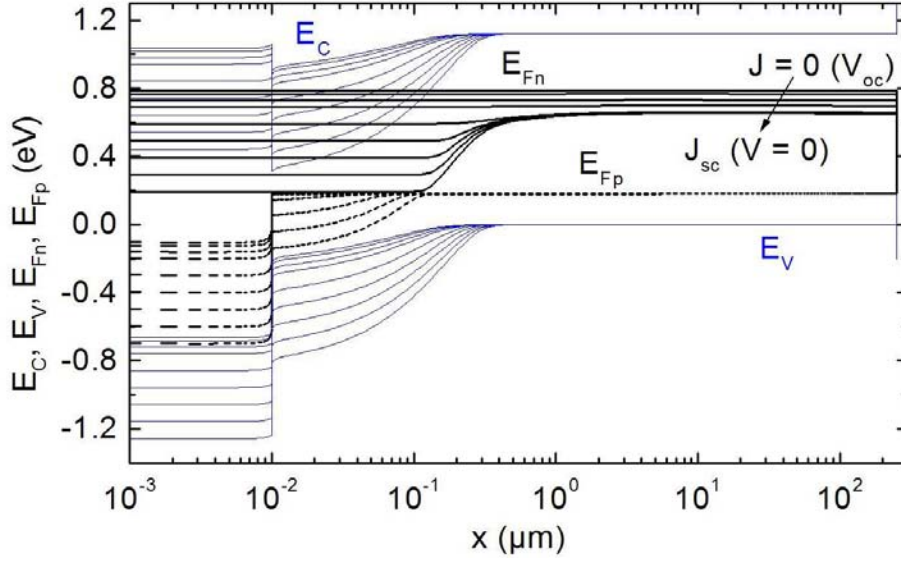


Figure 9.18: Simulated spatial distribution of E_C , E_V , E_{F_n} and E_{F_p} of a a-Si:H/c-Si solar cell for different operation points between open circuit voltage and short circuit conditions.

deviation of E_{F_n} , the averaged $E_{F_p} - E_{F_n}$ is not the same as $(E_{F_p}(0) - E_{F_n}(d))$. Thus $V = ((E_{F_p}(0) - E_{F_n}(d))/q \neq (E_{F_p} - E_{F_n})/q$ for voltages larger than 0.5 V in Figure 9.18. This can be easily detected at short circuit conditions, where the current is as large as a consequence of a huge gradient in the quasi-Fermi levels of electrons between the bulk and the contacts. With this gradient, in order to get all carriers extracted to the contacts, they should have an infinite mobility. As an infinite mobility is not realistic, some electron-hole pairs recombine in the volume and PL is detected.

In Figure 9.19 the I-V-characteristic curve obtained from the voltages calculated from the simulated PL of the studied structure is shown. The calculation has been developed integrating the product of carrier densities $n(x)p(x)$:

$$V = \frac{kT}{q} \ln \left(\frac{\frac{1}{d} \int_0^d n(x)p(x)dx}{n_0p_0} \right) \quad (9.6)$$

where d is the thickness of the wafer. In the simulation the voltage is obtained considering the spatial distribution of carriers. In Figure 9.19, it is also shown the ideal curve which was already depicted in Figure 9.15. The simulated PL-I-V-characteristic fits this curve in the range $V_{MPP} \leq V \leq V_{OC}$ ($V_{MPP} = 0.51$ V, $J_{MPP} = -33.67$ mA cm⁻²). In the Figure it is also shown the PL-IV-characteristic obtained from luminescence measurements (closed triangles). The PL-I-V-characteristics do not fit the I-V-curve without series resistance, showing less potential drop as the ideal characteristics when the same current is extracted. It is suggested that this effect is due to a voltage drop due to transport resistance of the holes in the bulk.

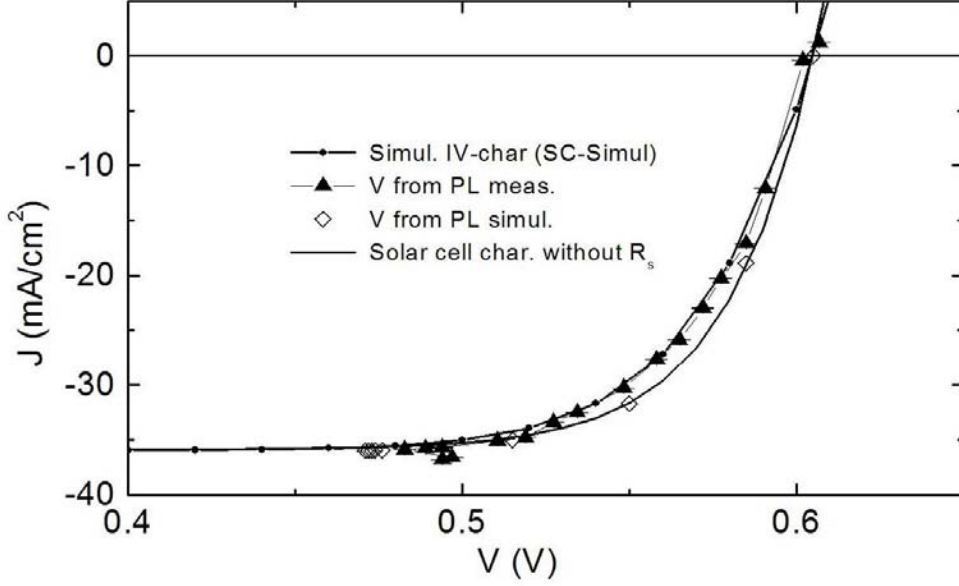


Figure 9.19: Simulated (open diamonds) and measured (closed triangles) PL-I-V-curve for a high efficiency (a)-Si:H/c-Si solar cell. The corrected IV-curve without series resistance for the same open circuit voltage and short circuit current is shown with a continuous line. The simulated I-V-curve is marked with closed circles. The PL-I-V-curve contains also the error bars derived from the error in the calculation of the splitting of quasi-Fermi levels.

This voltage difference is given by: $\Delta V = \text{grad}(E_{Fp})/q = j_p d / \sigma_p$. This fact has also been also detected by Ferraioli et al. [75]. Another reason could be that the profiles of the carrier densities in the measured solar cells are not as homogeneous as in the simulation and these inhomogeneities are reflected in the voltages derived from PL.

In Figure 9.19, all curves derived from photoluminescence show a large error for currents $> I_{MPP}$ due to the difference in the voltage between front and back contacts and the voltage derived from PL. This produces the differences in V between the open diamonds and the filled circles at the same current extraction for voltages $V < 0.5$ V in Figure 9.20. As photocurrent results in a p-type semiconductor from a gradient in the quasi-Fermi level of electrons, the higher the current the more inhomogeneous E_{F_n} is. This is depicted more in detail in Figure 9.20. For large currents E_{F_n} is much higher in the volume as at the contacts and therefore

$$E_{F_n}(0) - E_{F_n}(d) \ll kT \ln \frac{\frac{1}{d} \int_0^d n(x)p(x)dx}{n_o p_o} \quad (9.7)$$

The quasi-Fermi levels of electrons and holes for V_{oc} , I_{sc} and an intermediate external voltage $V = 0.4$ V are shown. The splitting of quasi-Fermi levels obtained from the integration of the product np and derived voltages drops are displayed

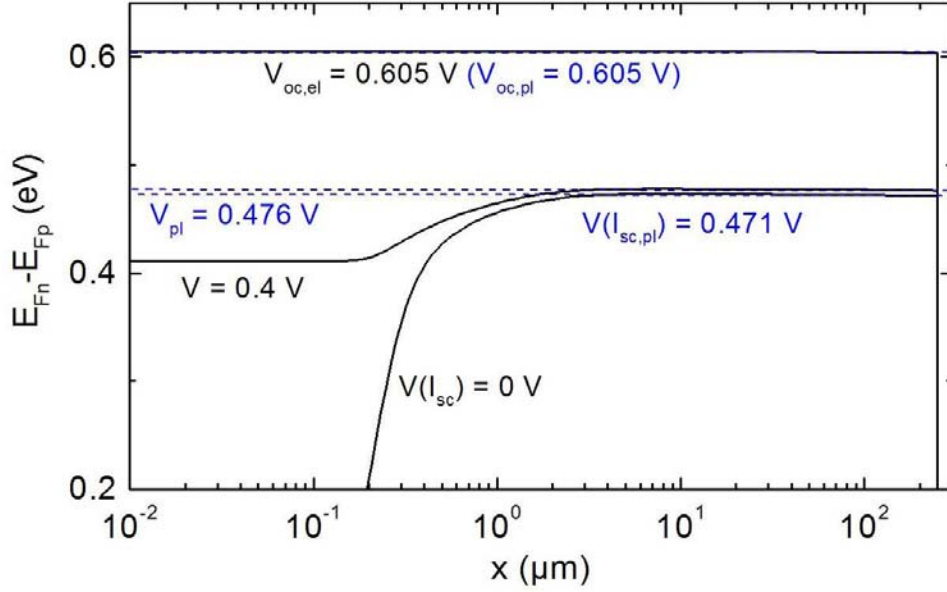


Figure 9.20: Simulated spatial distribution of E_{F_n} for open circuit ($V = V_{OC}$, short circuit ($V = 0$ V) and an intermediate voltage $V = 0.4$ V. The voltages derived from the integral of the product of carrier densities are shown with dashed lines, so that the differences between the electrically measured voltages and the voltages derived from PL can be easily distinguished.

with dashed lines. They differ strongly from the electrically measured values for currents close to J_{sc} .

9.3 Error estimation between voltages derived from PL and electrically measured voltages

In this section I analyze the error in the voltage drop derived from photoluminescence measurements. The error obtained from the high efficiency solar cell simulated in the previous section is examined. Figure 9.21 shows the difference between the external voltage and the voltage derived from PL and the average value of np for the (n)a-Si:H/(p)c-Si simulated solar cell. There are two regions in both curves. For $0 \leq V \leq 0.4$ V, the integral of np , i.e. the emitted PL, does not vary because the current extracted is approximately constant. Therefore, the error in the calculated voltage decreases when the external voltage increases from 0 to 0.4 V, getting closer to the value of the voltage drop derived from the splitting of quasi-Fermi levels in the volume. The error between the electrically measured external voltage drop and the voltage difference derived from PL decreases till it diminishes completely at V_{oc} conditions where there are not voltage drops at series resistance as no current flows through the cell. These differences account for ca. $0.5 \times kT$ at MPP to 0 at OC. In this second region ($V > 0.4$ V), in the simula-

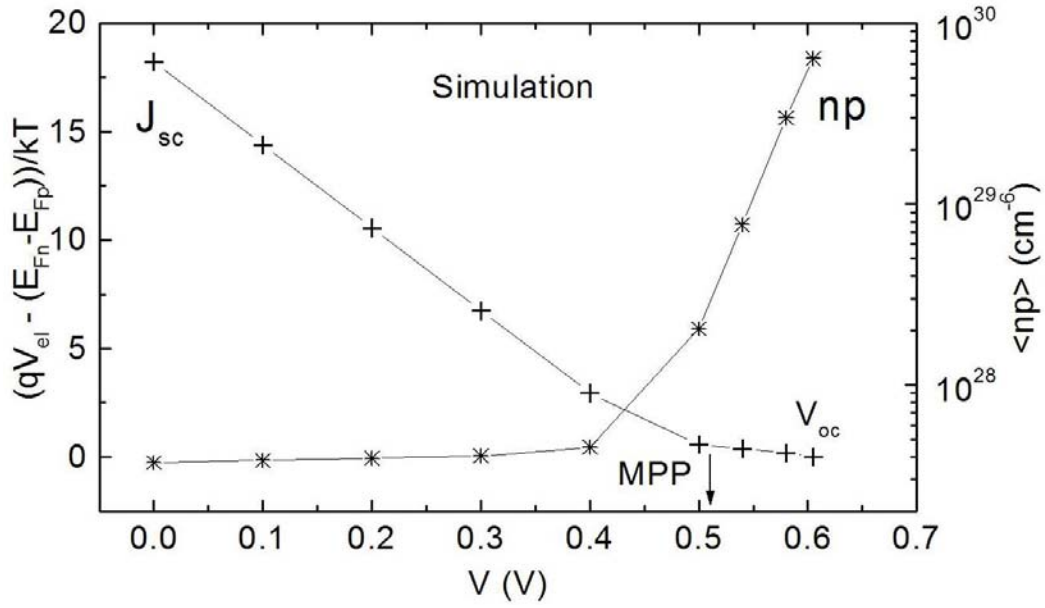


Figure 9.21: Difference between the electrically measured voltage and the voltage drop derived from PL simulation versus the external voltage (crosses). The stars show the integral of the simulated np also versus the applied voltage.

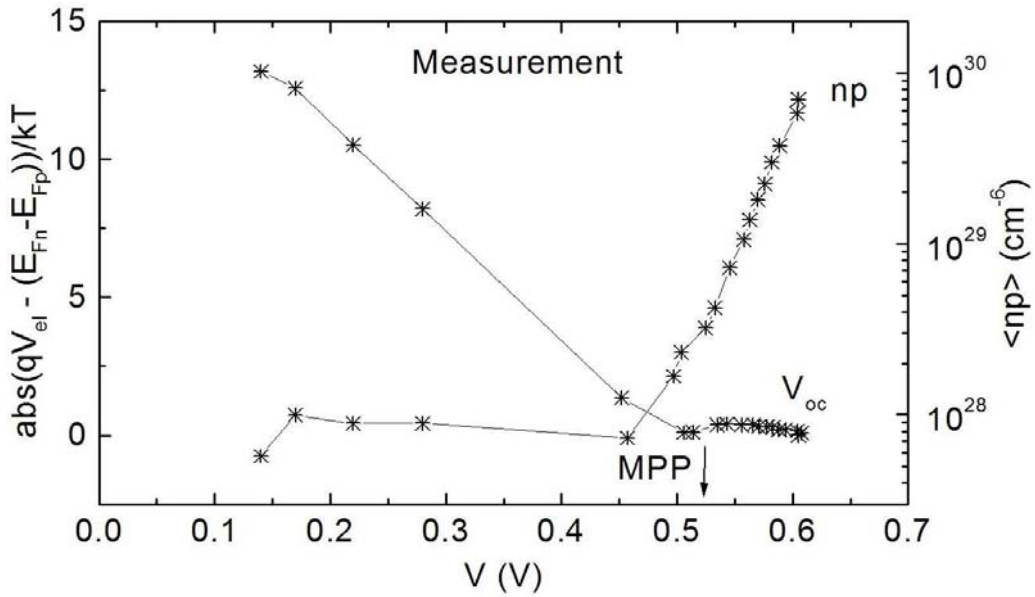


Figure 9.22: Difference between the I-V-curve without series resistance and the voltage derived from PL measurements versus the external voltage (crosses). The stars show the integral of the np derived from the measured PL yield also versus the applied voltage.

tion the difference between both voltages could be seen; which is mainly due to a local diminution of the quasi-Fermi levels of holes in a region very close to the

contacts which is not accounted by the PL. For $V < 0.4$ V the of error derives from the inhomogeneity of the profile of electrons when high currents close to J_{sc} are extracted from the cell, and therefore the splitting of quasi-Fermi levels in the volume is different than at the contacts.

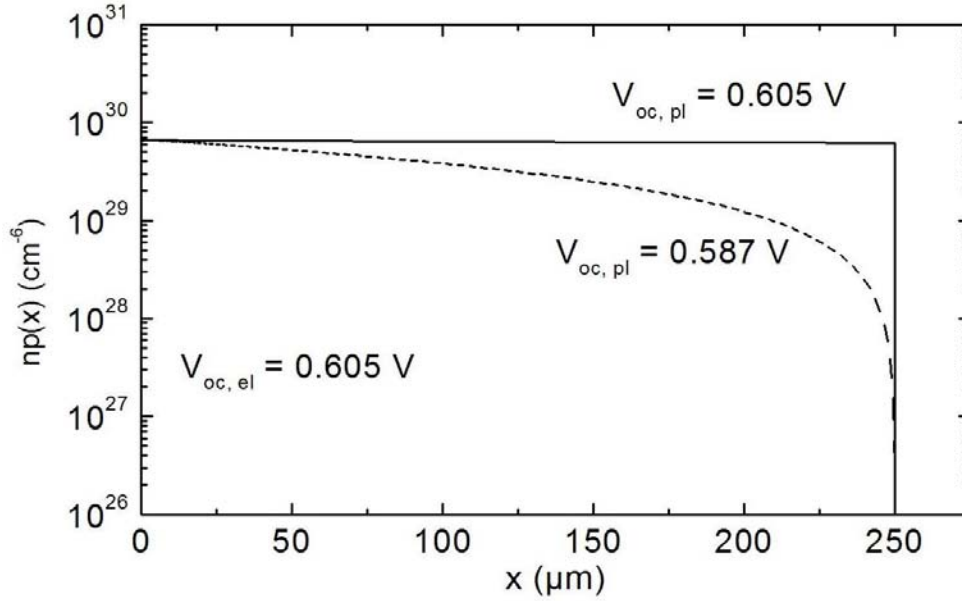


Figure 9.23: Product of carriers in the c-Si bulk for the previously simulated structure and for a not high efficiency a-Si:H/c-Si solar cell with the same $V_{oc} = 0.605$ V. An important decrement in the minorities for the solar cell without (p)a-Si:H due to a higher recombination at the back contact occurs.

In the simulated high efficiency (a)-Si/c-Si solar cell, the open circuit voltage calculated from PL and the electrically measured are equal. This solar cell is optimized to avoid recombination at the back and front of the solar cell, so that the splitting of quasi-Fermi levels is nearly constant in the bulk and does not diminish at the contacts. For non-optimized solar cells, high recombination via defects could take place in the bulk and at the surfaces of the wafer so that carrier densities diminish and therefore the splitting of quasi-Fermi levels in the volume divided by the electron charge does not equal the external measured voltage. This case is illustrated in Figure 9.23. I have simulated a solar cell under 1.5 AM equivalent photon-flux with a higher defect density in the bulk and without the (p)a-Si:H layer at the back of the wafer, so that more recombination takes place in the volume and at the back contact. The effect is a remarkable decrease of the minorities in the volume and thus, reduction of PL. The open circuit voltage calculated from luminescence (using Formula (9.6)) is reduced from 0.605 V for the heterostructure with (p)a-Si:H to 0.587 V for the lower quality solar cell without back surface field.

Figure 9.22 shows the same magnitudes as in Figure 9.21 using the I-V-curve with-

out series resistance from the solar cell. Both intervals can also be identified in the graph. The error between the voltage derived from PL and the voltage from the IV-characteristics without R_s is reduced from $0.37 \times kT$ to $0.15 \times kT$ at OC.

9.4 Conclusions

Simulation of photoluminescence of an a-Si:H/c-Si solar cell at open circuit and short circuit conditions has been performed. The photoluminescence yield and the splitting of quasi-Fermi levels are very sensitive against interface defect densities at open circuit conditions for the typical N_{if} range. On the contrary, at short circuit, the variation of the density of interface defects is not reflected in the integral of the product of carrier densities in the bulk. Thus, the photoluminescence yield at SC is not strongly affected by recombination at the interface.

The ratio of $Y_{pl,oc}/Y_{pl,sc}$ can be used to estimate the interface defect density from relative measurements of PL, when the diffusion length of the heterostructure is known. In the analyzed solar cells, the defect density is in the range $2 \times 10^{11} cm^{-2} < N_{if} < 2 \times 10^{12} cm^{-2}$.

From the comparison between the measured PL-I-V-curve with the curve without series resistance, it can be seen that the voltage derived from luminescence differs from the voltage from the IV-characteristics without R_s for $0.4 < V < V_{OC}$. At J_{sc} and for large currents close to J_{sc} (from 0 V to ca. 0.4 V), there is a large difference between the voltages measured electrically and the ones obtained from PL. The reason for this difference is inhomogeneity of the carrier densities when current is extracted from the device. At short circuit conditions a high luminescence yield can still be detected from the volume as it is not possible to extract immediately all carriers before they recombine. Similar results are obtained from the simulated solar cell. In the simulation, for voltages between V_{oc} and maximum power point, the difference is due to voltage drops at contacts and at regions close to the contact which do not contribute appreciably to the integral of the product np and, thus, are not detected by PL.

In general, the inhomogeneity in the distribution of carriers over the wafer, which produces the departure in the calculation of $E_{F_n} - E_{F_p}$, can be caused by: 1. high recombination in the front and back of the wafer; 2. extraction of carriers through the contacts. In the first case, even the calculation of the open circuit voltage from PL includes an error. The second reason predominates for good quality solar cells. In the simulation, the luminescence yield in the range $0 \leq V \leq 0.4$ V is constant because the extracted current is also almost constant and the profile of the carriers $n(x)$ and $p(x)$ does not vary significantly with the applied voltage. In that range the error diminishes because the applied voltage gets closer to the voltage derived

from the PL. For higher voltages, these differences diminish from ca. $0.5 \times kT$ at MPP to 0 at OC, as the current extracted decreases and the profiles of the carriers in the bulk are more homogeneous. Similar tendencies can be observed for the experimental results. Therefore, PL measurements could be used to separate internal losses due to recombination in the bulk, as the bulk resistance, from voltage drops at the contact or at small close regions next to the contact, in the range $V_{MPP} \leq V \leq V_{OC}$ for high efficiency solar cells.

Chapter 10

Summary / Zusammenfassung

This thesis focusses on the analysis and characterization of hydrogenated amorphous silicon/crystalline silicon (a-Si:H/c-Si) solar cells and wafers by simulated and quantitatively measured photoluminescence (PL).

Different passivation layers (a-Si:H and SiN_x) on nominally identical (p)c-Si substrates were compared in terms of splitting of quasi-Fermi levels ($E_{F_n} - E_{F_p}$) derived from PL, which gives the maximum achievable open circuit voltage. The results show that the wafer pretreatment and doping of the amorphous silicon film influence the $E_{F_n} - E_{F_p}$, likely due to variation in the interface defect density (N_{if}) and consequently modifications in the recombination at the interface. Different deposition parameters and wafer pretreatment executed by various institutes complicate the identification of the critical variables which influence N_{if} . However, a tendency could be observed: wafers with HF-dip pretreatment and an (i)a-Si:H passivation show, in general, a higher splitting of quasi-Fermi levels and therefore a higher open circuit voltage should be expected from solar cells with these passivation layers.

Effective lifetime $\tau_{eff,pl}$ was also calculated from luminescence. Furthermore, the excitation intensity dependence of the photoluminescence yield has been examined. Non-linearities have been detected and two possible explanations have been studied: bulk lifetime intensity dependence and surface recombination intensity dependence. Simulation of the bulk lifetime intensity dependence show non-linearities for recombination and capture coefficients which could be non-realistic. Variations of the slope in the curves of PL yield versus excitation intensity for different passivation layers on the same substrate suggest that surface recombination could also play an important role in the explanation of the non-linearities. Surface recombination also varies when the excitation intensity is increased, but it shows a higher variation than previous studies resulted from PCD measurements. A combination of both illumination dependencies, from the bulk and from the surface, is a possible explanation for the non-linearities.

Experimentally derived absorption coefficients (α) for c-Si at different tempera-

tures have been calculated from the quantitative measurements of PL. The curves of $\alpha(\hbar\omega)$ have been compared with previous experimental measurements of α , finding a very good agreement. The dependence of the lifetime on temperature has also been studied. It is found that it increases with T . This result is in contradiction with the observed reduction of the PL yield. This effect is explained by the temperature dependence of the band-band recombination coefficient, which decreases for higher T .

Using the advantage of PL as a contactless measurements, consecutively processed layers during device deposition and evaluation of each of the process steps has been analyzed. Simulation of PL has shown, as expected, that the interface defect density in a-Si:H/c-Si heterojunctions influences the splitting of quasi-Fermi levels in the whole structure very strongly. The comparison of the splitting of quasi-Fermi levels from quantitative photoluminescence experiments with simulation allowed the extraction of parameters for the interface defects and their recombination dynamics in the a-Si:H/c-Si heterojunction. Interface defects are estimated to be energetically situated at around 0.72 eV above the valence band for a Gauss distribution. Furthermore, detailed studies about recombination have shown that defects situated at midgap are most effective.

Simulation of the carrier densities and splitting of quasi-Fermi levels at open circuit voltage has shown the high sensitivity of these variables for different interface defect densities. Contrarily, PL at short circuit conditions are not affected by variations at the interface. Finally, a PL-I-V-curve from a high efficiency a-Si:H/c-Si solar cell has been derived from quantitative photoluminescence measurements and it has been compared with the electrically measured I-V-characteristics. The differences between both curves are due to the assumption of a constant distribution of carriers in the bulk for currents close to the short circuit current and to the voltage drop at contact and at areas close to the contact for voltages different than the V_{oc} . Simulation shows that, the splitting of quasi-Fermi levels is not constant when carriers are extracted and it decreases at sites near contacts. It has also been observed that also at short circuit, still it is possible to measure luminescence because not all carriers can be extracted and they recombine in the volume. For non-high efficiency solar cells, surface recombination increases the inhomogeneity of the carriers densities and the error in the estimation of the voltage between contacts increases, even for open circuit conditions.

Zusammenfassung

Diese Doktorarbeit fokussiert sich auf die Analyse und Characterisierung von a-Si:H/c-Si Solarzellen und Wafern durch Messungen und Simulation von quantitativer Photolumineszenz (PL).

Verschiedene Passivierungsschichten (a-Si:H und SiN_x) auf gleichem (p)c-Si Substrat wurden bezüglich der Aufspaltung von quasi-Fermi Niveaus ($E_{F_n} - E_{F_p}$) verglichen. Diese wurde aus PL-Messungen ermittelt und geben die maximale Leerlaufspannung der Heterostruktur für Solarzellen mit hoher Effizienz an. Die Ergebnisse zeigen, dass die Vorbehandlung des Wafers und Dotierung des amorphen Siliziumfilms $E_{F_n} - E_{F_p}$ beeinflussen, höchstwahrscheinlich wegen der Variation der Interfacedefektdichte (N_{if}) und folglich Rekombination am Interface. Verschiedene Depositionsparameter und die Vorbehandlung des Wafers von unterschiedlichen Instituten erschweren die Identifikation der kritischen Variablen, die N_{if} beeinflussen. Allerdings, konnte man eine Tendenz beobachten: Wafer mit HF-Dip Vorbehandlung und (i)a-Si:H Passivierung zeigen allgemein eine höhere Aufspaltung der Quasi-Fermi Niveaus und deswegen sollte man aus Solarzellen mit dieser Art Passivierungsschicht eine höhere Leerlaufspannung erwarten.

Dazu wurde aus dem erhaltenen $E_{F_n} - E_{F_p}$ auch die effektive Lebensdauer $\tau_{eff,pl}$ ausgerechnet. Außerdem ist die Abhängigkeit der Photolumineszenzausbeute von der Anregungsintensität geprüft worden. Nicht-Linearitäten sind detektiert und 2 mögliche Erklärungen sind analysiert worden: die Abhängigkeit der Volumenlebensdauer von der Intensität und Intensitätsabhängigkeit der Rekombination an der Oberfläche. Die Simulation der die Intensitätsabhängigkeit der Volumenlebensdauer zeigt Nicht-Linearitäten für Rekombinations- und Einfangkoeffizienten, die nicht realistisch sein können. Variation der Steigung bei verschiedenen Passivierungsschichten auf gleichem Substrat deuten an, dass die Oberflächerekombination eine große Rolle in der Erklärung der Nicht-Linearitäten spielen könnten. Die Oberflächenrekombination ändert sich auch mit der Anregungsintensität, aber zeigt eine größere Variation als vorherige Studien, die auf PCD (photoconductive decay) Messungen basieren. Eine Kombination von Volumen- und Oberflächeintensitätsabhängigkeit wird als mögliche Erklärung der Nicht-Linearitäten vorgeschlagen.

Experimentelle Absorptionskoeffizienten (α) für c-Si wurden aus quantitativen Photolumineszenzmessungen bei verschiedenen Temperaturen abgeleitet. Die resultierenden Werte werden mit vorherigen experimentellen Ergebnissen von α verglichen und man hat eine sehr gute Übereinstimmung gefunden. Die Temperaturabhängigkeit der Lebensdauer ist auch berechnet worden. Man hat gefunden, dass sie mit T zunimmt. Dieses Ergebnis scheint der Abnahme der beobachteten

Photolumineszenzausbeute zu widersprechen. Die Temperaturabhängigkeit des Band-Band Rekombinationskoeffizienten, die mit der Temperatur abnimmt, kann diesen Effekt erklären.

Durch den Vorteil der kontaktlosen PL Messungen wurde eine Analysemethode der fortlaufend prozessierten Schichten während der Herstellung der Solarzelle entwickelt und jeder Prozessschritt evaluiert. PL-Simulationen haben für verschiedene c-Si Waferstrukturen eine direkte Anti-Korrelation zwischen der Rekombinationsrate am Interface und der Aufspaltung der Quasi-Fermi Niveaus im Volumen gezeigt. Demnach beeinflusst die Interfacedefektdichte in a-Si:H/c-Si Heteroübergängen die Aufspaltung der Quasi-Fermi Niveaus in der ganzen Struktur sehr stark. Ergebnisse für die Strukturen mit unterschiedlichen a-Si:H Schichten weisen darauf hin, dass eine Optimierung des vorderen und hinteren Interfaces für das Erreichen von hohen V_{oc} in diesen Heterodioden entscheidend ist. Der Vergleich der Aufspaltung des Quasi-Fermi Niveaus aus quantitativen Photolumineszenzmessungen mit Simulationsergebnissen erlaubt die Parameterextraktion für Interfacedefekte und die Rekombinationsdynamik am a-Si:H/c-Si Heteroübergang. Die Interfacedefekte in den analysierten Strukturen befinden sich schätzungsweise energetisch etwa 0.72 eV oberhalb des Valenzbands und haben eine Gaussverteilung. Weitere detaillierte Studien über Rekombination haben gezeigt, dass Defekte die in der Mitte der Bandlücke liegen am effektivsten sind.

Die Simulation von Ladungsträgerdichten und der Aufspaltung der Quasi-Fermi Niveaus bei Leerlaufspannung hat gezeigt, dass diese Variablen eine sehr hohe Sensibilität gegenüber der Interfacedefektdichte haben. Entgegengesetzt, bei Kurzschluss sind die vorherigen Variablen durch Variationen am Interface nicht beeinflusst. Als letzter Teil wurde eine PL-I-V-Kurve einer hocheffizienten a-Si:H/c-Si Solarzelle aus quantitativen Photolumineszenzmessungen bei verschiedenen Betriebspunkten gemessen und mit elektrisch gemessenen I-V-Kurven verglichen worden. Die Unterschiede zwischen beider Kurven sind begründet durch die Annahme einer konstanter Ladungsträgerverteilung im Volumen bei Strömen dicht beim Kurzschlussstrom und vom Spannungsabfall am Serienwiderstand vom Kontakt und am Flächen nah zum Kontakt für Spannungen unterschiedlich als V_{oc} . Mit Hilfe der Simulation hat man gesehen, dass die Aufspaltung der Quasi-Fermi Niveaus aufgrund von Ladungsträgerextraktion nicht mehr konstant ist und in der Nähe von Kontakten abnimmt. Man hat auch beobachtet, dass es möglich ist Lumineszenz bei Kurzschluss zu messen, da die Ladungsträger eine endliche Mobilität haben, so dass nicht alle extrahiert werden und somit einige im Volumen rekombinieren. Die Oberflächenrekombination nimmt für Solarzellen mit wenig Effizienz zu und daher wird die Ladungsträgerverteilung inhomogener, so dass der Fehler in der Abschätzung der Spannung sogar bei Leerlaufspannung größer wird.

Acknowledgments

At this point I would like to thank all those who supported me while I was working on my PhD thesis.

Gottfried H. Bauer gave me the opportunity to develop my thesis in his group and take part in a German network project. I learnt a lot about solar cells and photoluminescence under his supervision.

Rudi Brüggemann was very helpful as second supervisor. I had very useful discussions with him and he gave me a lot of advice during the development of scientific articles.

All other members of the GRECO group were also always very friendly and cooperative colleagues. All of them were always open to listen to me and help with suggestions.

And last but not least, I would like to thank my very close friends and family, without their moral support I would never have finished this work.

Appendix A

Error calculation in the splitting of quasi-Fermi levels

The error in the splitting of quasi-Fermi levels has been calculated as an error propagation derived from the calibration of the setup. Therefore, first of all I will start evaluating the error obtained from the photoluminescence signal. Once the transfer function is known, the measured PL can be easily quantified by:

$$Q_{PL}(\lambda) = T(\lambda)M_{PL}(\lambda) \quad (\text{A.1})$$

being $Q_{PL}(\lambda)$ the quantified PL measured signal, $T(\lambda)$ the transfer function and $M_{PL}(\lambda)$ the directly measured signal in volts.

The transfer function has been obtained in equation (D.5) (chapter 5). The relative error of $T(\lambda)$ is given as

$$\frac{\Delta T(\lambda)}{T(\lambda)} = \sqrt{\left(\frac{\Delta B(\lambda)}{B(\lambda)}\right)^2 + \left(\frac{\Delta \varepsilon(\lambda)}{\varepsilon(\lambda)}\right)^2 + \left(\frac{\Delta T_{NG}(\lambda)}{T_{NG}(\lambda)}\right)^2 + \left(\frac{\Delta M_t(\lambda)}{M_t(\lambda)}\right)^2} \quad (\text{A.2})$$

where $B(\lambda) = dn_{bb,2500K}(\lambda)/d\lambda$ and $M_t(\lambda) = dV_t(\lambda)/d\lambda$ have been taken in order to work with simplified expressions.

Using (A.2) it is possible to get the propagated error in the calibrated function $Q_{PL}(\lambda)$:

$$\begin{aligned} \frac{\Delta Q_{PL}(\lambda)}{Q_{PL}(\lambda)} &= \sqrt{\left(\frac{\Delta T(\lambda)}{T(\lambda)}\right)^2 + \left(\frac{\Delta M_{PL}(\lambda)}{M_{PL}(\lambda)}\right)^2} \\ &= \sqrt{\left(\frac{\Delta B(\lambda)}{B(\lambda)}\right)^2 + \left(\frac{\Delta \varepsilon(\lambda)}{\varepsilon(\lambda)}\right)^2 + \left(\frac{\Delta T_{NG}(\lambda)}{T_{NG}(\lambda)}\right)^2 + \left(\frac{\Delta M_t(\lambda)}{M_t(\lambda)}\right)^2 + \left(\frac{\Delta M_{PL}(\lambda)}{M_{PL}(\lambda)}\right)^2} \quad (\text{A.3}) \end{aligned}$$

Now I will calculate each of the relative errors in equation (A.3). The error in the 'black body' function is due to the inaccuracy in the determination of the tungsten lamp temperature ($T_t \approx 2500 \pm 50K$). This temperature of the tungsten lamp was determined using a bolometer from one side and the slope of a spectral measurement from the other side. The error was determined statistically. This error in the temperature, introduced in the expression (D.6) from Appendix D, implies an error of $\Delta B(\lambda)/B(\lambda) = 0.15$. $\Delta \varepsilon(\lambda)/\varepsilon(\lambda) = 0.015$ is obtained from literature data [76]. The error of the neutral glass filter $T_{NG}(\lambda)$ derives from transmission measurements: $\Delta T_{NG}(\lambda)/T_{NG}(\lambda) = 0.01$. Talking about the measured signal, two factors should be taken into account in order to determine the error: 1. the resolution of the monochromator, and 2. error in the wavelength calibration. The inaccuracy in the monochromator wavelength derives from the reciprocal linear dispersion in the grating, which is $3nm\ mm^{-1}$ for a grating of $1200\ g\ mm^{-1}$ (ref. manual) in our case. This can be translated, using the Bragg condition in a maximal error of $\Delta\lambda/\lambda = 0.004$. Wavelength calibration was obtained using different well determined wavelengths and calculating the transfer curve between the real wavelength and the one given by the counter of the monochromator:

$$\lambda_{real} = -53(\pm 5) + 2.10(\pm 0.01)\lambda_{counter} \quad (A.4)$$

$$\begin{aligned} \Delta\lambda_{real} &= \sqrt{5^2 + 0.01^2} \approx 5nm \\ \Rightarrow \frac{\Delta\lambda_{real}}{\lambda_{real}} &= 0.006 \end{aligned} \quad (A.5)$$

in the worst case for $\lambda_{real} = 800nm$. Therefore,

$$\frac{\Delta M_t(\lambda)}{M_t(\lambda)} = \frac{\Delta M_{PL}(\lambda)}{M_{PL}(\lambda)} = \sqrt{\left(\frac{\Delta\lambda}{\lambda}\right)^2 + \left(\frac{\Delta\lambda_{real}}{\lambda_{real}}\right)^2} = 0.007 \quad (A.6)$$

Adding all the errors as in formula (A.3):

$$\frac{\Delta Q_{PL}(\lambda)}{Q_{PL}(\lambda)} = 0.15 \quad (A.7)$$

As we can see, the main error comes from the inaccuracy in the determination of the tungsten lamp temperature.

As the photon flux per wavelength interval is related to the photon flux per energy interval by (D.8), the error expressed as a function of energy has the same value as in (A.7):

$$\frac{\Delta Q_{PL}(\hbar\omega)}{Q_{PL}(\hbar\omega)} = 0.15 \quad (A.8)$$

In our case the calibrated function is given by equation (6.1), where considering the Boltzmann approximation we get:

$$Q_{PL}(\hbar\omega) = \frac{dn_\gamma(\hbar\omega)}{d(\hbar\omega)} = C(\hbar\omega) \exp\left(\frac{E_{F_n} - E_{F_p}}{kT}\right) \quad (\text{A.9})$$

being $C(\hbar\omega) = \frac{(\hbar\omega)^2 \exp(-\hbar\omega/kT)}{4\pi^2 c_o^2 \hbar^3} \frac{(1-R)(1-\exp(-\alpha d))}{1-R\exp(-\alpha d)}$.

The splitting of quasi-Fermi energies and its error is obtained as following:

$$E_{F_n} - E_{F_p} = kT \ln \left(\frac{Q_{PL}(\hbar\omega)}{C(\hbar\omega)} \right) \quad (\text{A.10})$$

$$\Delta E_{F_n} - E_{F_p} = \sqrt{\left(\frac{\partial E_{F_n} - E_{F_p}}{\partial Q_{PL}(\hbar\omega)} \right)^2 (\Delta Q_{PL}(\hbar\omega))^2} = kT \frac{\Delta Q_{PL}(\hbar\omega)}{Q_{PL}(\hbar\omega)} \approx 4meV \quad (\text{A.11})$$

Considering the values of $E_{F_n} - E_{F_p}$ measured in this work, we find that the relative error is less than 1%.

Appendix B

Defects in a-Si:H

Defects in amorphous silicon have amphoteric character, i.e., they could be positively, or negatively charged. A defect is positive when the defect state is unoccupied and neutral when it is occupied by one electron. The third possible state is that an extra electron can be attached in a neutral defect state, forming a negative charged defect. This state is energetically unfavorable increasing its energy in comparison to the neutral or positive charge defects. The additional energy related to negative charged defects E_d^- is known as correlation energy U_{corr} and denotes the energy difference to neutral or positive charged defects $E_d^{0,+}$:

$$E_d^- = E_d^{0,+} + U_{corr} \quad (\text{B.1})$$

Due to this correlation energy, the probability functions of these defects are obtained solving the Hamiltonian $H = E_0 \sum_{i,S} n_{iS} - U \sum_i n_{i\uparrow} n_{i\downarrow}$, being n_{iS} the number operator for electrons with spin S localized on the defect at site i . E_0 and U are the energy of the positive or neutral defects and the correlation energy for the negative defects at site i respectively. The eigenvalues of this Hamiltonian are: $E_j = NE_0 - jU$, where N is the total number of electrons associated with the defect states and j is the number of doubly occupied states. For one defect which can be completely unoccupied, singly occupied or doubly occupied, applying statistics of the partition function [77] and the occupation probabilities for positive, neutral and negative charged defects are respectively given by:

$$Z = 1 + 2 \exp\left(\frac{E_F - E_d}{kT}\right) + \exp\left(\frac{2E_F - 2E_d - U_{corr}}{kT}\right) \quad (\text{B.2})$$

$$P_+ = \frac{1}{Z} \quad (\text{B.3})$$

$$P_0 = \frac{2}{Z} \exp\left(\frac{E_F - E_d}{kT}\right) \quad (\text{B.4})$$

$$P_- = \frac{1}{Z} \exp\left(\frac{2E_F - 2E_d - U_{corr}}{kT}\right) \quad (\text{B.5})$$

with E_F defined as Fermi energy. This model of defects was already integrated in

the simulation program SC-Simul [18] and it has been used to built a 2 nm defect layer with parameters from crystalline silicon (bandgap, mobility, doping...) with the additional described gaussian distribution of defects. The interface defect density has been considered to be fixed after the deposition of the (i)a-Si:H passivation layer at both sides of the (p)c-Si wafer, and consecutive changes in the splitting of quasi-Fermi levels should be caused of variations in the band bending produced by the addition of different layers in the a-Si:H/c-Si solar cell processing.

Appendix C

Recombination through interface defects

In this section I will describe the recombination in interface defects following the Shockley-Read-Hall formalism and apply an appropriate statistic for correlated defects. As interface defects are given in the form of dangling bonds, they can be neutral, negatively or positively charged.

In this model only recombination between the defects and the conduction or valence band has been considered. Recombination between defect levels in the band gap is neglected.

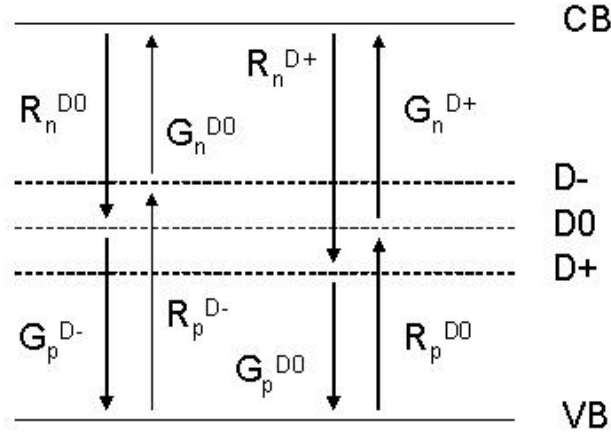


Figure C.1: Sketch of the recombination model considered for interface defects. Dangling bonds can be neutral or negatively or positively charged. In the figure all possible recombination rates between the defects and the conduction and valence band are shown. Transitions between defects are neglected.

Figure C.1 shows the different carrier transitions and the corresponding emission and generation rates. The different flows are linked to the concentration of carriers

and recombination centers by the Shockley-Read expressions

$$\begin{aligned}
R_n^{D0} &= c_n^{D0} n N_{if} f^{D0} \\
G_n^{D0} &= c_n^{D0} n_1^{D0} N_{if} f^{D-} \\
R_n^{D+} &= c_n^{D+} n N_{if} f^{D+} \\
G_n^{D+} &= c_n^{D+} n_1^{D+} N_{if} f^{D0} \\
R_p^{D-} &= c_p^{D-} p N_{if} f^{D-} \\
G_p^{D-} &= c_p^{D-} p_1^{D-} N_{if} f^{D0} \\
R_p^{D0} &= c_p^{D0} p N_{if} f^{D0} \\
G_p^{D0} &= c_p^{D0} p_1^{D0} N_{if} f^{D+}
\end{aligned} \tag{C.1}$$

The energy dependent terms n_1^{D0} , n_1^{D+} , p_1^{D0} and p_1^{D-} are given using the principle of the detailed balance [30], which implies that the rate of capture and the rate of emission of electrons (and holes) must be equal:

$$\begin{aligned}
n_1^{D+}(E_{D_{if}}) &= \frac{1}{2} N_C \exp\left(-\frac{E_C - E_{D_{if}}}{kT}\right) \\
n_1^{D0}(E_{D_{if}}) &= 2N_C \exp\left(-\frac{E_C - E_{D_{if}} - U_{corr}}{kT}\right) \\
p_1^{D0}(E_{D_{if}}) &= 2N_V \exp\left(-\frac{E_{D_{if}} - E_V}{kT}\right) \\
p_1^{D-}(E_{D_{if}}) &= \frac{1}{2} N_V \exp\left(-\frac{E_{D_{if}} + U_{corr} - E_V}{kT}\right)
\end{aligned} \tag{C.2}$$

Considering the system under illumination (G_L) and steady state, three independent equations characterize the system shown in Figure C.1 [78]:

$$\begin{aligned}
\frac{dn}{dt} &= G_n^{D0} - R_n^{D0} + G_n^{D+} - R_n^{D+} + G_L = 0 \\
\frac{dp}{dt} &= G_p^{D-} - R_p^{D-} + G_p^{D0} - R_p^{D0} + G_L = 0 \\
\frac{dn_{D+}}{dt} &= -G_p^{D0} - R_n^{D+} + G_n^{D+} + R_p^{D0} = 0
\end{aligned} \tag{C.3}$$

In addition,

$$f^{D+} + f^{D-} + f^{D0} = 1 \tag{C.4}$$

as the sum of all occupation probabilities should equal the unity.

Solving the system we find the occupation probabilities for neutral f^{D0} , positive f^{D+} and negative charged f^{D-} defects:

$$\begin{aligned}
f^{D-} &= \frac{2c_n^{D+}c_p^{D0}np - 2c_n^{D+}c_p^{D0}n_1^{D+}p_1^{D0} + c_n^{D0}n(c_n^{D+}n + c_p^{D0}p_1^{D0})}{g_{0-}} \\
&\quad + \frac{-c_n^{D+}c_p^{D-}np_1^{D-} - c_p^{D0}c_p^{D-}p_1^{D0}p_1^{D-}}{g_{0-}} \\
f^{D+} &= \frac{(c_n^{D+}n_1^{D+} + c_p^{D0}p)(c_n^{D0}n_1^{D0} - c_p^{D-}p)}{g_+} \\
f^{D0} &= \frac{(c_n^{D0}n_1^{D0} - c_p^{D-}p)(c_n^{D+}n + c_p^{D0}p_1^{D0})}{g_{0-}}
\end{aligned} \tag{C.5}$$

where the denominators g_{0-} and g_+ are given by:

$$\begin{aligned}
g_{0-} &= c_n^{D0}(c_n^{D+}(n^2 + nn_1^{D0} + n_1^{D0}n_1^{D+}) + c_p^{D0}(np_1^{D0} + n_1^{D0}(p + p_1^{D0})) \\
&\quad - c_p^{D0}c_p^{D-}(p^2 + pp_1^{D0} + p_1^{D0}p_1^{D-}) + c_n^{D+}(2c_p^{D0}(np - n_1^{D+}p_1^{D0})) \\
&\quad - c_p^{D-}(n_1^{D+}p + n(p + p_1^{D-}))) \\
g_+ &= (c_n^{D+}n_1^{D+} + c_p^{D0}p)(c_n^{D+}n + c_n^{D0}n_1^{D0} - c_p^{D-}p - c_p^{D0}p_1^{D0}) \\
&\quad - (c_n^{D+}n + c_p^{D0}p_1^{D0})(-c_n^{D0}(n + n_1^{D0}) + c_n^{D+}n_1^{D+} - c_p^{D0}p + c_p^{D-}p + c_p^{D-}p_1^{D-})
\end{aligned} \tag{C.6}$$

Appendix D

Calibration of photoluminescence setup

In order to quantify photoluminescence it is necessary to calculate a calibration curve which translates the voltage per wavelength given as an output signal from the detector to the photon flux per stereo radian in the energy interval $d(\hbar\omega)$ emitted by the sample. Therefore, it is required to have a calibrated source as a reference. In our case, a tungsten lamp was used. Radiation from this lamp is treated as black body radiation following Planck's law for a temperature of $T = 2500K$ multiplied by the emissivity of tungsten at same temperature. This can be written as

$$dn_\gamma(\lambda)/d\lambda \int_0^\Omega \cos \theta d\Omega = T(\lambda, \Omega) dV(\lambda)/d\lambda \quad (D.1)$$

where $n_\gamma(\lambda)$ is the photon flux emitted by the sample, θ is the angle of the emitted photons with normal to the surface, $d\Omega$ is the differential solid angle of the radiation, $T(\lambda, \Omega)$ is the transfer function (from the measured to the calibrated curve) and $V(\lambda)$ is the measured curve. The term $\cos \theta$ is due to the Lambert's cosine law [33]

We are looking for the transfer function $T(\lambda)$. It will be obtained by comparison of a theoretical curve obtained from Planck's Law and a measured curve of a 'black body' radiation (in this case, the tungsten lamp)

$$AT_{opt}(\lambda) \frac{dn_\gamma(\lambda)}{d\lambda} \int_0^\Omega \cos \theta d\Omega = B(\lambda) \frac{dV(\lambda)}{d\lambda} \quad (D.2)$$

$$A_t T_{NG}(\lambda) T_{opt}(\lambda) \varepsilon(\lambda) \frac{dn_{bb,2500K}(\lambda)}{d\lambda} \int_0^{\Omega_t} \cos \theta_t d\Omega_t = B(\lambda) \frac{dV_t(\lambda)}{d\lambda} \quad (D.3)$$

where A and $d\Omega$ are respectively the emitting area and solid angle interval in photoluminescence measurements, $T_{opt}(\lambda)$ is the transmission of the whole optical system, $V_t(\lambda)$ is the measured signal from the tungsten lamp, $\varepsilon(\lambda)$ is the emissivity of the tungsten lamp at 2500 K, A_t and $d\Omega_t$ are respectively the emitting area and

solid angle interval for the calibration measurements, $T_{NG}(\lambda)$ is the transmission of the neutral glass filters used for the calibration measurements to avoid damaging of the detector due to high intensity radiation coming from the tungsten lamp and $B(\lambda)$ is the calibration curve of the photoluminescence setup.

Rearranging Eqs. (D.2) and (D.3) to get the same expression as Eq. (D.1), it is possible to get the desired transfer function $T(\lambda, \Omega)$

$$T(\lambda, \Omega) = \frac{\frac{dn_{bb,2500K}(\lambda)}{d\lambda} \varepsilon(\lambda) T_{NG}(\lambda) A_t \int_0^\Omega \cos \theta d\Omega_t}{\frac{dV_t(\lambda)}{d\lambda} A \int_0^{\Omega_t} \cos \theta_t d\Omega} \quad (D.4)$$

In order to account for the same emitting areas and solid angles for photoluminescence and tungsten lamp measurements and thus simplify the transfer function, a pinhole has been introduced in the entrance to the monochromator. Another requirement is to set both the sample and the calibration lamp at the same position in order to get the same emitting area and solid angle. This procedure simplifies notably the calculation to get quantitative photoluminescence, because it is not necessary anymore to measure the areas or solid angles implied and angular dependencies are neglected.

Thus, using the pinhole: $A = A_t$, $\theta = \theta_t$ and $d\Omega = d\Omega_t$ and the transfer function is given by

$$T(\lambda) = \frac{\frac{dn_{bb,2500K}(\lambda)}{d\lambda} \varepsilon(\lambda) T_{NG}(\lambda)}{\frac{dV_t(\lambda)}{d\lambda}} \quad (D.5)$$

From Planck's law [32, 29] the function $dn_{bb,2500K}(\lambda)/d\lambda$ is derived:

$$\frac{dn_{bb,2500K}(\lambda)}{d\lambda} = \frac{2c_o}{\lambda^4} \frac{1}{\exp \frac{hc}{\lambda k 2500K} - 1} \quad (D.6)$$

as the photon flux emitted by a 'black body area' per wavelength for $T = 2500K$. $\varepsilon(\lambda)$ is obtained from the literature [76] and $T_{NG}(\lambda)$ and $dV_t(\lambda)/d\lambda$ are measured.

Once we have multiplied the output data by the transfer function, the photon flux per wavelength interval is obtained. We are interested in calculating the photon flux per energy interval, thus it is necessary to do the following transformation

$$d(\hbar\omega) = \frac{hc}{\lambda^2} d\lambda \quad (D.7)$$

$$\frac{dn_\gamma(\hbar\omega)}{d(\hbar\omega)} = \left(\frac{dn_\gamma(\lambda)}{d\lambda} \frac{\lambda^2}{2\pi\hbar c} \right)_{\lambda=\hbar\omega} \quad (D.8)$$

Bibliography

- [1] G. Sasaki, S. Fujita, and A. Sasaki. Gap-states measurement of chemically vapor-deposited amorphous silicon: High-frequency capacitance-voltage method. *Journal of Applied Physics*, 53(2):1014–1017, February 1982.
- [2] A. Goetzberger, B. Voß, and J. Knobloch. *Sonnenenergie: Photovoltaik*. Teubner, Stuttgart, 1997.
- [3] Sakata, T. Nakai, T. Baba, M. Taguchi, S. Tsuge, K. Uchihashi, and S. Kiyama. 20.7 % highest efficiency large area (100.5 cm²) HIT cell. In *Proceedings 28th IEEE PVSEC*, pages 7–12, New York, 2000. IEEE.
- [4] M. Taguchi, H. Sakata, Y. Yoshimine, E. Maruyama, A. Terakawa, M. Tanaka, and S. Kiyama. An approach for the higher efficiency in the HIT cells. In *Proceedings 31st IEEE PVSC*, pages 866 – 871, New York, 2005. IEEE.
- [5] P. Würfel. The chemical potential of radiation. *J. Phys. C: Solid State Phys.*, 15:3967–3985, 1982.
- [6] R. Brüggemann, M. Rösch, S. Tardon, and G. H. Bauer. Application of SC-simul for numerical modeling of the opto-electronic properties of heterojunction diodes. In *Material Research Society Symposium*, volume 862, pages A9.3.1–A9.3.6, 2005.
- [7] G. H. Bauer, R. Brüggemann, M. Rösch, S. Tardon, and T. Unold. Numerical modelling as a tool for understanding room temperature photoluminescence in a-Si:H/c-Si heterojunction solar cells. *Physica Status Solidi C*, 1(5):1308–1315, 2004.
- [8] E. Daub and P. Würfel. Ultralow values of the absorption coefficient of Si obtained from luminescence. *Physical Review Letters*, 74(6):1020–1023, February 1995.
- [9] E. Daub and P. Würfel. Ultra-low values of the absorption coefficient for band-band transitions in moderately doped Si obtained from luminescence. *Journal of Applied Physics*, 80(9):5325–5331, November 1996.

- [10] T. Unold, D. Berkhahn, B. Dimmler, and G. H. Bauer. Open circuit voltage and loss mechanism in polycrystalline Cu(InGa)Se₂-heterodiodes from photoluminescence. In H. Scheer et al., editor, *Proceedings of 16th PVSEC Conference*, pages 736–739. James&James Scient. Publ. London, May 2000.
- [11] S. Tardon, R. Brüggemann, M. Rösch, and G. H. Bauer. Quantitative photoluminescence as a tool to estimate density and energy distribution of interface defects in a-Si:H/c-Si heterostructures. In W. Palz et al., editor, *Proceedings of 20th European Photovoltaic Solar Energy Conference*, pages 1259–1262, Ispra, Juni 2005. Joint Research Center European Commission.
- [12] F. Roca, D. Della Sala, G. Di Francia, P. Grillo, G. Fameli, F. Pascarella, and A. Citarelle. Relevant process steps for the fabrication of amorphous silicon / crystalline silicon heterojunction solar cells. In W. Freiersleben et al., editor, *13th European Photovoltaic Solar Energy Conference*, pages 1558–1561, Bedford, 1995. H. S. Stephens.
- [13] H. Matsuura. Hydrogenated amorphous silicon/ crystalline silicon heterojunctions: Properties and applications. In *IEEE Transactions on Electron Devices*, volume vol. 36, pages 2908–2913, vol. 36, 1989.
- [14] R. A. Street. *Hydrogenated Amorphous Silicon*. Cambridge University Press, Cambridge, 1991.
- [15] J. Kanicki. *Amorphous and Microcrystalline Semiconductor Devices*. Artech House, Boston, 1991.
- [16] M. Vanecek, A. Abraham, O. Stoika, J. Struchlik, and J. Kocka. Gap states density in a-Si:H deduced from subgap optical absorption measurement on Schottky solar cells. *Physica Status Solidi*, A(83):617, 1983.
- [17] D. V. Lang, J. D. Cohen, and J. P. Harbison. Measurement of the density of gap states in hydrogenated amorphous silicon by space charge spectroscopy. *Physical Review B*, 25(8):5285–5320, April 1982.
- [18] Maximilian Rösch. *Experimente und Numerische Modellierung zum Ladungsträgertransport in a-Si:H/c-Si Heterodioden*. PhD thesis, Carl von Ossietzky Universität Oldenburg, 2003.
- [19] S.M. Sze. *Physics of Semiconductor Devices*. John Wiley & Sons, New York, 2nd edition, 1981.
- [20] H. Eschrich, L. Elstner, and J. Bruns. Numerical simulation of ACJ-HIT solar cells. In R. Hill et al., editor, *12th European Photovoltaic Solar Energy Conference*, pages 172–175, Bedford, 1994. H. S. Stephens.

- [21] K. V. Maydell, M. Schmidt, L. Korte, A. Laades, E. Conrad, R. Stangl, M. Scherff, and W. Fuhs. Basic electronic properties and optimization of TCO/a-si:h(n)/c-si(p) hetero solar cells. In *31st IEEE Photovoltaic Specialists Conference*, pages 1225–1228, New York, 2005. IEEE.
- [22] A. S. Gudovskikh, J. P. Kleider, A. Froitzheim, W. Fuhs, and E. I. Terukov. Investigation of a-si:h/c-si heterojunction solar cells interface properties. *Thin Solid Films*, 451-452:345–349, 2004.
- [23] M. L. D. Scherff, A. Froitzheim, A. Ulyashin, M. Schmidt, W. R. Fahrner, and W. Fuhs. 16.2 % efficiency for Amorphous/Crystalline silicon heterojunction solar cells on flat p-type silicon wafer. In *PV in Europe - From PV Technology to Energy Solutions*, 2002, Rome.
- [24] A. Froitzheim, K. Brendel, L. Elstner, W. Fuhs, K. Kliefoth, and M. Schmidt. Interface recombination in heterojunctions of amorphous and crystalline silicon. *Journal of Non-Crystalline Solids*, 299-302:663–667, 2002.
- [25] A. Froitzheim, H. Angermann, K. Brendel, L. Elstner, W. Füssel, J. Knechtel K. Kliefoth, M. Schmidt, N. Sinh, H. Weiser, and W. Fuhs. Interface and transport properties of a-Si:H(n)/c-Si(p) solar cells. In H. Scheer et al., editor, *16th European Photovoltaic Solar Energy Conference*, pages 1580–1583. James&James Scient. Publ. London, 2000.
- [26] S. Dauwe, J. Schmidt, A. Metz, and R. Hezel. Fixed charge density in silicon nitride films on crystalline silicon surfaces under illumination. In *29th IEEE Photovoltaics Specialists Conference*, pages 162–165, New York, 2002. IEEE.
- [27] S. Dauwe, J. Schmidt, and R. Hezel. Very low surface recombination velocities on p- and n-type silicon wafers passivated with hydrogenated amorphous silicon films. In *29th IEEE Photovoltaic Specialists Conference*, pages 1246–1249, New York, 2002. IEEE.
- [28] E. Hecht and A. Zajac. *Optics*. Addison-Wesley Publishing Company, 1974.
- [29] P. Würfel. *Physics of Solar Cells*. Wiley-VCH, Weinheim, 2005.
- [30] W. Van Roosbroeck and W. Shockley. Photon-radiative recombination of electrons and holes in germanium. *Physical Review*, 94(6):1558–1560, June 1954.
- [31] E. Daub. *Photolumineszenz von Silizium*. PhD thesis, Universität Karlsruhe, 1995.
- [32] M. Planck. *Vorlesungen über Die Theorie der Wärmestrahlung*. Johann Ambrosius Barth, Leipzig, 1906.
- [33] K. Schick, E. Daub, S. Finkbeiner, and P. Würfel. Verification of a generalized planck law for luminescence radiation from silicon solar cells. *Applied Physics A*, 54:109–114, 1992.

- [34] D. Berkhahn. Stationäre photolumineszenz in $Cu(In_{1-x}Ga_x)Se_2$. Master's thesis, Carl von Ossietzky Universität Oldenburg, 1998.
- [35] R. Häcker and A. Hangleiter. Intrinsic upper limits of the carrier lifetime in silicon. *Journal of Applied Physics*, 75(11):7570–7572, June 1994.
- [36] A.G. Aberle. *Crystalline Silicon Solar Cells: Advanced Surface Passivation and Analysis*. Centre for Photovoltaics Engineering, University of New South Wales Publishing and Printing Services, 1999.
- [37] W. Shockley and W. T. Read. Statistics of the recombinations of holes and electrons. *Physical Review*, 87(5):835–843, September 1952.
- [38] A. W. Stephens, A. G. Aberle, and M. A. Green. Surface recombination velocity measurements at the silicon-silicon dioxide interface by microwave-detected photoconductive decay. *Journal of Applied Physics*, 76(1):363–370, July 1994.
- [39] H. Mäkel and R. Lüdemann. Detailed study of hydrogenated SiN_x layers for high-quality silicon surface passivation. *Journal of Applied Physics*, 92(5):2602–2609, September 2002.
- [40] E. Yablonovitch, D. L. Allara, C. C. Chang, T. Gmitter, and T. B. Bright. Unusually low surface-recombination velocity on silicon and germanium surfaces. *Physical Review Letters*, 57(2):249–252, July 1986.
- [41] A. Froitzheim. *Hetero-Solarzellen aus Amorphem und Kristallinem Silizium*. PhD thesis, Philipps-Universität Marburg, 2003.
- [42] N. Jensen, R. M. Hausner, R. B. Bergmann, J. H. Werner, and U. Rau. Optimization and characterization of Amorphous/Crystalline silicon heterojunction solar cells. *Progress in Photovoltaics: Research and Applications*, 10:1–13, 2002.
- [43] M. A. Green. Intrinsic concentration, effective densities of states, and effective mass in silicon. *Journal of Applied Physics*, 67(6):2944–2954, 1990.
- [44] F. Voigt and T. Jiasundera. Recombination of a four level system program. Technical report, Carl von Ossietzky Universität Oldenburg, 2005. Program developed with MATLAB at GRECO by Felix Voigt und Tharanga Jiasundera, with some contributions from the author.
- [45] R. H. Bube. *Photoelectric Properties of Semiconductors*. Cambridge University Press, 1992.
- [46] Sebastian Meier. *Temperaturabhängige Photolumineszenz zur Bestimmung des Bimolekularen Rekombinationskoeffizienten in Kristallinem Silizium*. work-study, Carl von Ossietzky Universität Oldenburg, 2005.

- [47] J. Schmidt and A. G. Aberle. Accurate method for the determination of bulk minority-carrier lifetimes of mono- and multicrystalline silicon wafers. *Journal of Applied Physics*, 81(9):6186–6199, May 1997.
- [48] P. P. Altermatt, J. Schmidt, G. Heiser, and A. G. Aberle. Assessment and parameterisation of coulomb-enhanced Auger recombination coefficients in lowly injected crystalline silicon. *Journal of Applied Physics*, 82(10):4938–4944, November 1997.
- [49] A. Cuevas, M. J. Kerr, and J. Schmidt. Passivation of crystalline silicon using silicon nitride. In Kurokawa et al., editor, *Third World Conference on Photovoltaic Solar Energy Conversion*, number 1, pages 913–918, Tokyo, May 2003. Wcpec-3 Organizing Committee.
- [50] T. Lauinger, J. Schmidt, A. G. Aberle, and R. Hezel. Record low surface recombination velocities on 1 Ωcm p-silicon using remote plasma silicon nitride. *Applied Physical Letters*, 68(9):1232–1234, February 1996.
- [51] J. Schmidt, J. D. Moschner, J. Henze, S. Dauwe, and R. Hezel. Recent progress in the surface passivation of silicon solar cells using silicon nitride. In H. Ossenbrink et al., editor, *19th European Photovoltaic Solar Energy Conference, Paris, France*, pages 391 – 394. WIP Munich and ETA-Florence, 2004.
- [52] M. J. Kerr, J. Schmidt, and A. Cuevas. Surface recombination velocity of phosphorus-diffused silicon solar cell emitters passivated with plasma enhanced chemical vapor deposited silicon nitride and thermal silicon oxide. *Journal of Applied Physics*, 89(7):3821–3826, April 2001.
- [53] C. Boehme and G. Lucovsky. Origins of silicon solar cell passivation by $\text{SiN}_x\text{:H}$ anneal. *Journal of Non-Crystalline Solids*, 299-302:1157–1161, 2002.
- [54] J. Henze, C. Schmiga, J. Schmidt, and R. Hezel. Passivation of defects in mc-si and EFG-si by hydrogen release from low frequency and remote PECVD silicon nitride. In H. Ossenbrink et al., editor, *19th European Photovoltaic Solar Energy Conference*, pages 907–910. WIP Munich and ETA-Florence, 2004.
- [55] S. Dauwe, L. Mittelstädt, A. Metz, J. Schmidt, and R. Hezel. Low-temperature rear surface passivation schemes for $\lambda > 20$ silicon solar cells. In Kurokawa et al., editor, *3rd World Conference on Photovoltaic Energy Conversion*, pages 1395 – 1398, Tokyo, 2003. Wcpec-3 Organizing Committee.
- [56] J. H. Stathis D. Jousse, J. Kanicki. Observation of multiple silicon dangling bond configurations in silicon nitride. *Applied Physics Letters*, 54(11):1043–1045, March 1989.

- [57] M. W. M. Van Cleef, F. M. Schuurmans, A. S. H. Van der Heide, A. Schönecker, and R. E. I. Schropp. Passivation of c-si solar cells by low temperature h-treatments and deposited a-si:h layers. In J. Schmid et al., editor, *2nd World Conference and Exhibition on Photovoltaic Solar Energy Conversion*, pages 1661–1664, Ispra, 1998. Joint Research Center European Commission.
- [58] L. J. Geerligs and D. Macdonald. Base doping and recombination activity of impurities in crystalline silicon solar cells. *Progress in Photovoltaics: Research and Applications*, 12:309–316, 2004.
- [59] S. Diez, S. Rein, and W. Glunz. Analyzing defects in silicon by temperature- and injection dependent lifetime spectroscopy (t-IDLS). In W. Palz et al., editor, *20th European Photovoltaic Solar Energy Conference, Barcelona, Spain*, pages 1216 – 1219, Ispra, 2005. Joint Research Center European Commission.
- [60] K. Bothe. Photoconductive decay measurement realized at the ISFH (Germany).
- [61] R. J. Elliot. Intensity of optical absorption by excitons. *Physical Review*, 108(6):1384–1389, December 1957.
- [62] G. G. MacFarlane, T. P. McLean, J. E. Quarrington, and V. Roberts. Fine structure in the absorption-edge spectrum of silicon. *Physical Review*, 111(5):1245–1254, September 1958.
- [63] R. Corkish and M. A. Green. Band edge optical absorption in intrinsic silicon: Assessment of the indirect transition and disorder models. *Journal of Applied Physics*, 73(8):3988–3996, April 1993.
- [64] P. J. Dean, J. R. Haynes, and W. F. Flood. New radiative recombination processes involving neutral donors and acceptors in silicon and germanium. *Physical Review*, 161(3):711–729, September 1967.
- [65] V. Alex, S. Finkbeiner, and J. Weber. Temperature dependance of the indirect energy gap in crystalline silicon. *Journal of Applied Physics*, 79(9):6943–6946, May 1996.
- [66] K. P. O'Donnell and X. Chen. Temperature dependance of semiconductor band gaps. *Applied Physics Letters*, 58(25):2924–2926, June 1991.
- [67] M. A. Green and M. J. Keevers. Short communication: Optical properties of intrinsic silicon at 300. *Progress in Photovoltaics: Research and Applications*, 3:189–192, 1995.
- [68] H. Mäkel and A. Cuevas. Open-circuit voltage quantum efficiency technique for defect spectroscopy in semiconductors. *Applied Physics Letters*, 87(104102):1–3, August 2005.

- [69] S. Rein, T. Rehrl, W. Warta, and S. W. Glunz. Lifetime spectroscopy for defect characterization: Systematic analysis of the possibilities and restrictions. *Journal of Applied Physics*, 91(4):2059–2070, February 2002.
- [70] T. Trupke, M. A. Green, P. Würfel, P. P. Altermatt, A. Wang, J. Zhao, and R. Corkish. Temperature dependance of the radiative recombination coefficient of intrinsic crystalline silicon. *Journal of Applied Physics*, 94(8):4930–4935, October 2003.
- [71] D.K. Schroeder. *Semiconductor Material and Device Characterisation*. John Wiley & Sons, New York, 1990.
- [72] A. Laades, K. Kliefoth, L. Korte, K. Brendel, R. Stangl, M. Schmidt, and W. Fuhs. Surface passivation of crystalline silicon wafers by hydrogenated amorphous silicon probed by time resolved surface photovoltage and photoluminescence spectroscopy. In H. Ossenbrink et al., editor, *19th European Photovoltaic Solar Energy Conference*, pages 1170 – 1173. WIP Munich and ETA-Florence, 2004.
- [73] Measurement done at FUH (Germany) by Maximilian Scherff.
- [74] A. G. Aberle, S. R. Wenham, and M. A. Green. A new method for accurate measurements of the lumped series resistance of solar cells. In *23th IEEE Photovoltaic Specialist Conference*, pages 133–139, New York, 1993. IEEE.
- [75] L. Ferraioli, P. Maddalena, A. Parretta, A. Wang, and J. Zhao. Current-voltage characteristics of high-efficiency silicon solar cells from photoluminescence. *Applied Physics Letters*, 85(18):4222–4224, November 2004.
- [76] D. R. Lide. *Handbook of Chemistry and Physics*. CRC Press, 75th edition, 1994-1995.
- [77] D. Adler and E. J. Yoffa. Electronic structure of amorphous silicon. *Physical Review Letters*, 36(20):1197–1200, May 1976.
- [78] F. Vaillant and D. Jousse. Recombination at dangling bonds and steady-state photoconductivity in a-Si:H. *Physical Review B*, 34(6):4088–4098, September 1986.

Curriculum Vitae

Education

- 10. 2001 / present: “Quantitative Photoluminescence Analysis of a-Si:H/c-Si Solar Cells“, PhD studies, Faculty of Sciences, Carl von Ossietzky University Oldenburg (Germany).
- 06. 2001 / 09. 2001: Master Thesis “Luminescence and Electronic Studies of a-Si:H/c-Si Hetero Solar Cells”, Semiconductor Physics Department, Carl von Ossietzky University Oldenburg (Germany)
- 09. 2000 / 09. 2001: Postgraduate Program in Renewable Energies, Carl von Ossietzky University Oldenburg (Germany).
- 10. 1993 / 06. 2000: Physics Degree, Faculty of Sciences, University of the Basque Country (Spain).

Work Experience

- 07. 2005 / 10. 2005: Scientific assistant at GRECO, Semiconductor Physics Department, Carl von Ossietzky University Oldenburg (Germany) financed by donation of the energy corporation EWE
- 10. 2001 / 04. 2005: Scientific assistant at GRECO, Semiconductor Physics Department, Carl von Ossietzky University Oldenburg (Germany)
- 10. 2001 / 02. 2004: Teaching assistant, Postgraduate Program of Renewable Energies, Carl von Ossietzky University Oldenburg (Germany)
- 02. 2001 / 03. 2001: External practical training, Fraunhofer Institute, Institute of Solar Energy Systems, Gelsenkirchen (Germany)

Hiermit erkläre ich, dass

a) ... ich die vorliegende Arbeit selbständig verfasst habe und nur die angegebenen Hilfsmittel verwendet habe.

b)... Teile des Kapitels „Quantitative measurements of photoluminescence“ der Dissertation zur Publikation in der Zeitschrift „Journal of Non-crystalline Solids“ veröffentlicht wurden.

c)... Teile des Kapitels „a-Si:H/c-Si Solar Cell Processing: Step by Step via PL“ der Dissertation zur Publikation im Konferenzband „20th European Photovoltaic Solar Energy Conference and Exhibition“ veröffentlicht wurden.

Saioa Tardon